Chapter 8 Computational Fluid Dynamic Modelling

It is clear from the preceding presentation of results that the degree of success with which Dijstelbergen's "frictionless" equation can be used to correct meter data varies. Results are particularly unsatisfactory for meter B. It has been suggested that this occurs because of a lack of flow guidance due to the low blade count for the meter. However, it is difficult to confirm this explanation without directly examining the pattern of flow through the meter. The resolution of this issue has provided the stimulus for undertaking a CFD (computational fluid dynamics) simulation based investigation of flowmeter response. The present chapter gives an account of the work carried out.

In this chapter, a review of published works dealing with the application of CFD to turbine flowmeters will be given. An account is then given of the work undertaken towards the development of a CFD model of unsteady turbine flowmeter response. This includes a description of the techniques used to generate the computer model for flow in a helically bladed rotor and of the simplifying assumptions which were made. Next, the simulation results from the model applied to the geometry of meter B, for which least satisfactory corrections were obtained, are presented. CFD data are used to predict meter errors under pulsating flow condition (both over-registration of the mean flow and the pulsation amplitude attenuation) and the results are compared with experimental measurements and with the predicted errors derived using the Dijstelbergen equation. Finally, the numerical data are used to examine the underlying assumptions of the Dijstelbergen equation.

8.1 Literature Review

There appears to be only three published works on the application of CFD to turbine flowmeters: Ferreira (1988), Xu (1992b) and Caffrey et al. (1997). All of the published models were developed to predict the performance of a turbine flowmeter under steady flow conditions.

A detailed mathematical model was built by Ferreira (1988) using a software developed for the analysis of flow in turbomachinery compressors. This model used the "Through-flow

Analysis" approach developed by Wu (1952) and Marsh (1966) to solve a three-dimensional geometrical problem by modelling a series of two-dimensional problems. Ferreira divided the rotor into ten cylindrical blade-to-blade surfaces, and a single hub-to-shroud surface, about the axis of the meter. The blade-to-blade and hub-to-shroud solutions were obtained by an iterative procedure, each solution defining the stream surfaces on which the other was solved. The relative flow through the rotor was assumed to be steady; the outer shroud was assumed to be rotating together with the rotor; and there was no leakage through the blade tips. Hub, blade and shroud boundary layers were calculated but no separation was allowed.

Ferreira used Laser Doppler velocimetry to measure the velocity components in the rotor blade passages of four different 50 mm 10-bladed turbine meters (two with helical blades and two with flat blades). The measured velocity components were compared with the predicted values. In the central region of the blade passage (away from the blade surfaces, the hub, the shroud, and from the leading and trailing edges) the axial velocity was predicted to within 5% and the swirl velocity within 10%. Predictions of K-factor curves were not made.

Xu (1992a) used a two-dimensional inviscid flow model (based on the vortex panel method) to predict the flow behaviour around turbine flowmeter blades. In his model, the separated leading edge flow and the trailing edge wake were simulated by shed vortices. The spanwise distribution of flow over a three-dimensional blade was approximated by interpolating two-dimensional solutions on cylindrical flow surfaces. In this way, the aerodynamic characteristic of a flowmeter blade could be evaluated for use in meter performance predictions.

Xu (1992b) further developed his model to obtain the net driving torque on a flowmeter rotor. He calculated all resisting torques, except for pick-up torque, using published equations (some of which are shown in Chapter 3) with slight modifications to accommodate for his model. Xu found that the bearing friction dominated other retarding torques at small flow rates but that it dropped very quickly as the flow rate was increased. At the higher flow rates, the blade boundary layer friction was the most dominant retarding torque, and the friction torques on the hub surface and the end disk were of secondary importance.

The model was validated against experimental data for a 100mm turbine flowmeter operating in the linear flow range with three different levels of inlet swirls. The predicted flowmeter K factor accuracy was within 1 % without inlet swirl; and within 3 % for cases with inlet swirl.

Caffrey et al. (1997) carried out a three-dimensional computational investigation into the effects of viscosity and installation on a turbine meter. They used commercially available CFD software to simulate different upstream flow conditions. The flow model did not include any formulation for bearing friction, blade thickness, tip clearance and end wall boundary layer influence. An iterative method was used to predict the zero net torque operating condition of the rotor and hence to predict its operating speeds. Results were presented for fully developed axial inlet flow at two Reynolds numbers and for swirling inlet flow. The model over-estimated the performance of 4 different rotors (nominal size: 100 mm) to within 5 to 10 % of their measured K-factors for the linear range.

In summary, it is evident from these three studies that, for steady flow, some qualitative measure of agreement can be obtained between numerical prediction and experiment. Quantitative agreement, reported to be between 1 % (Xu's model) and 10 % (Caffrey et al.'s model) for blade speed, is still well above the level required for calibration purposes. However, the particular relevance of these results to unsteady flows is questionable as it is expected that the flow pattern through the meter blading may be substantially altered by flow pulsation. Clearly, there is potential for far more extensive regions of separated/stalled flow to exist in pulsating flow as a consequence of increased flow incidence on the meter blades.

No papers reporting CFD modelling of turbine flowmeter under pulsating flow conditions were found.

8.2 CFD Model Development

The meter to be simulated is meter B (nominal size 12mm), which has a three-bladed rotor. The blades are helical, of uniform thickness with angle varying from 20° at the hub to 40° at the tip. The meter has a hub-to-tip ratio of 0.4 and clearance at the tip is 4% of the blade span. (See Appendix A and Figure 6.1 for a photographic view of the actual rotor).

This section describes the development of the CFD model and is divided into sub-sections dealing with the model geometry, the governing equations, the computational mesh and the solution procedure.

8.2.1 Model geometry

A simplified model of the physical flow installation is used: Figures 8.1 and 8.2 show for comparison the actual meter installation and the modelled installation. A cascade view of the actual installation is shown in Figure 8.3.

Note that the modelled installation is simplified in the following respects:

1. Uniform inlet velocity profile
2. No flow straighteners
3. No end-wall boundary layers resolved for calculations (shear free slip condition)
4. Zero tip clearance
5. Extended hub section, therefore no hub disc friction torque
6. No retarding torque related to the magnetic pick-up
7. No retarding torque related to the bearing assembly

It was originally intended to include many of these features as progressive refinements to the model, however, due to limitations on computing resource no feature was eventually included in the final model.

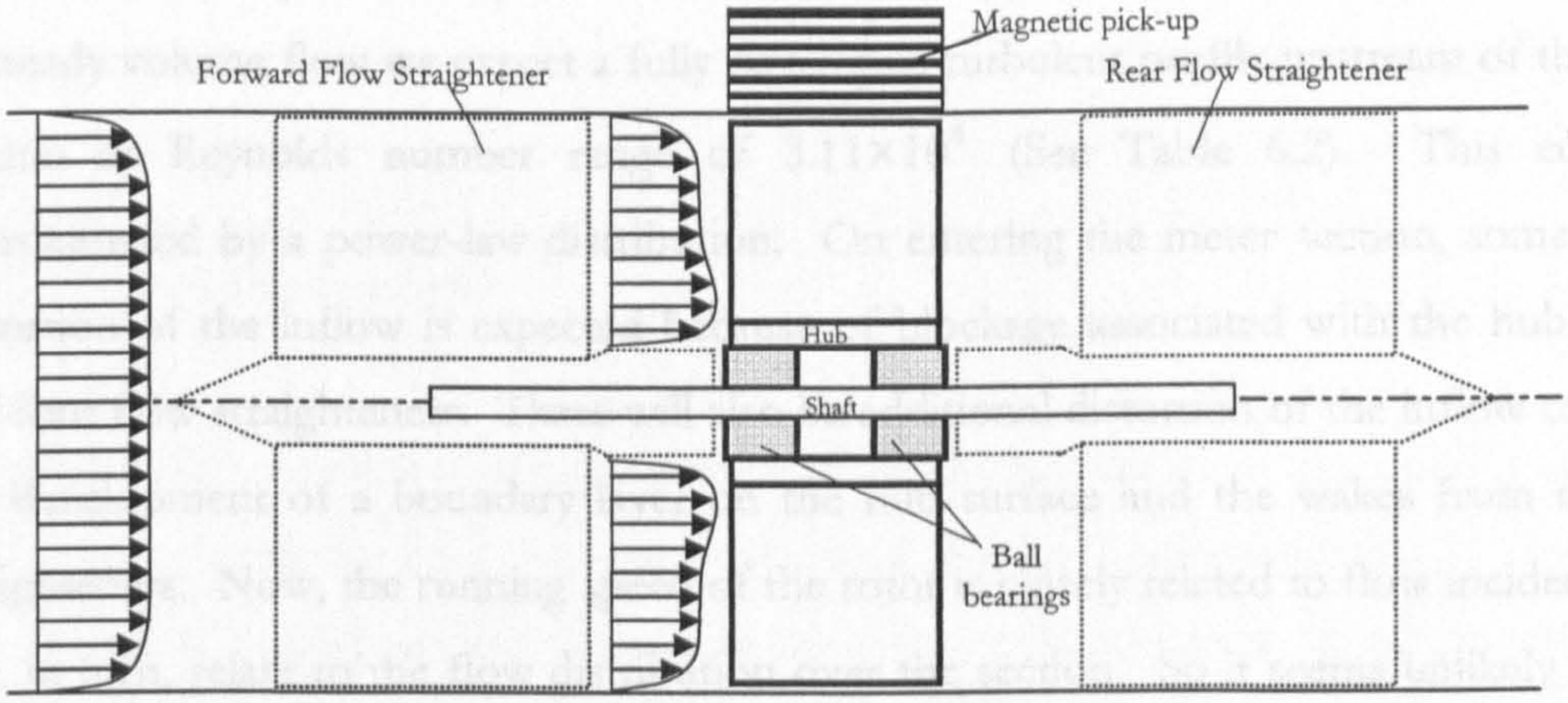

Figure 8.1 **Schematic drawing of the actual installation of meter B**

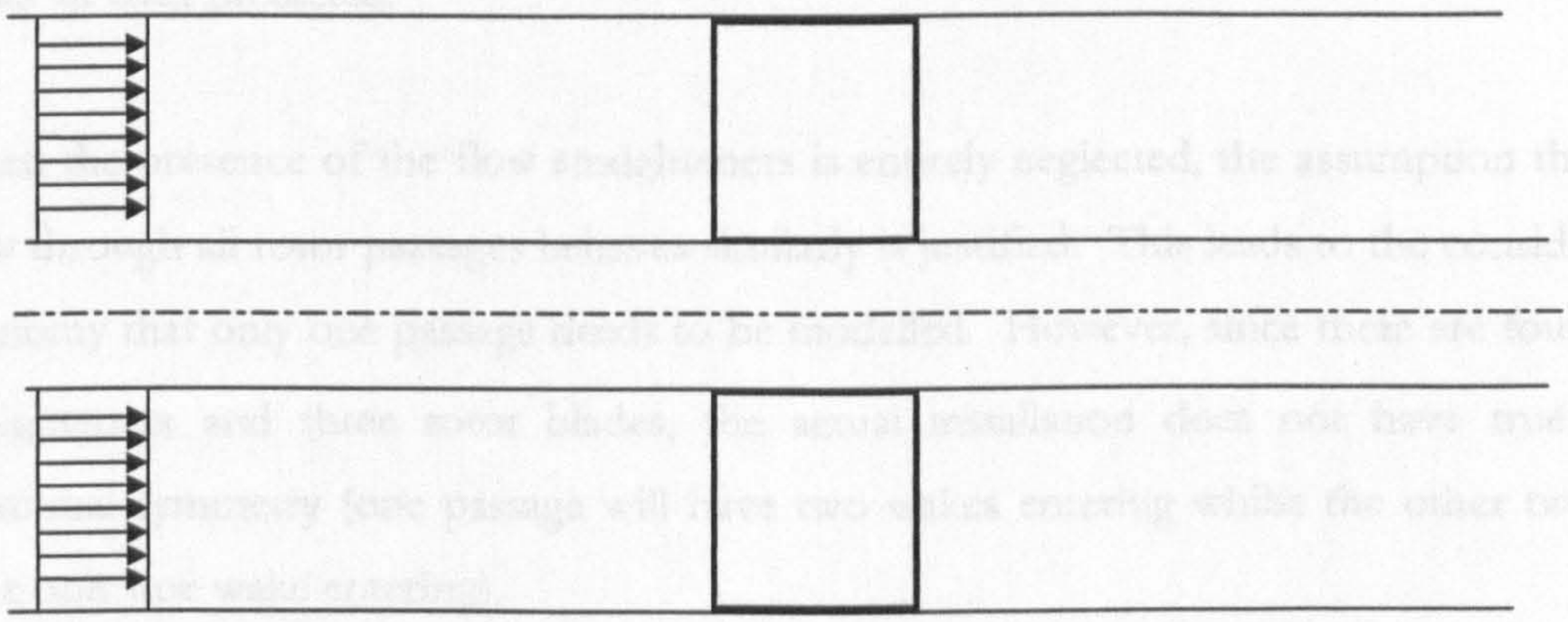

Figure 8.2 **Schematic drawing of the modelled installation of meter B**

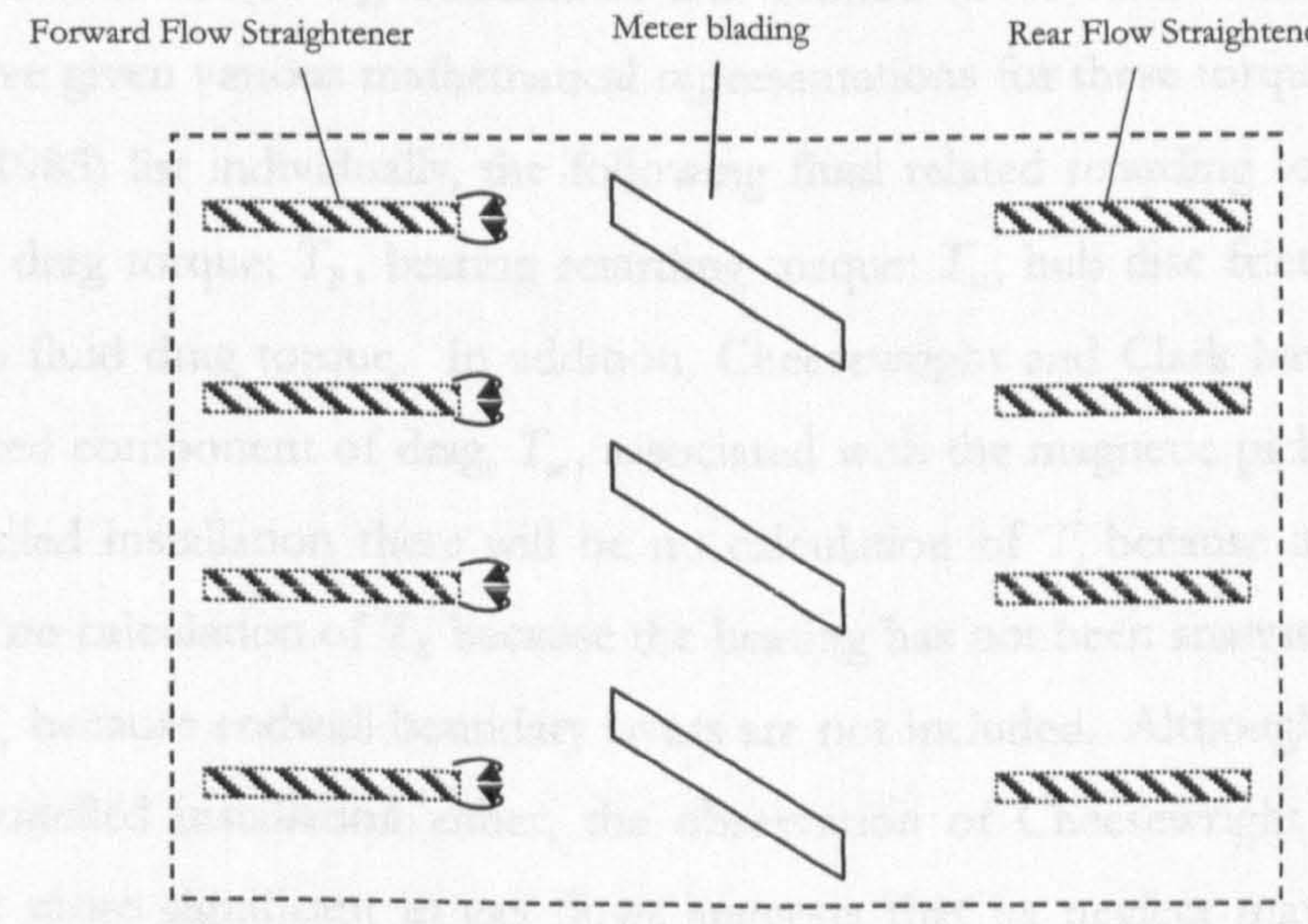

Figure 8.3 **Schematic drawing showing the wake patterns generated from the forward flow straightener on the cylindrical surface at a general radius, *r***

Clearly, the velocity profile entering the rotor section is considerably more complex than the uniform inlet profile adopted in the model. Firstly, even under the simplest conditions of steady volume flow we expect a fully developed turbulent profile upstream of the meter section at Reynolds number range of 3.11×10^4 (See Table 6.2). This could be approximated by a power-law distribution. On entering the meter section, some further distortion of the inflow is expected because of blockage associated with the hub section and four flow straighteners. There will also be additional distortion of the inflow related to the development of a boundary layer on the hub surface and the wakes from the flow straighteners. Now, the running speed of the rotor is closely related to flow incidence; this will, in turn, relate to the flow distribution over the section. So it seems unlikely that the blade speed can be computed with a high level of accuracy if an assumption of uniform inlet velocity is maintained. However, it is not possible to say whether the speed will be under or over predicted.

When the presence of the flow straighteners is entirely neglected, the assumption that the flow through all rotor passages behaves similarly is justified. This leads to the considerable economy that only one passage needs to be modelled. However, since there are four flow straighteners and three rotor blades, the actual installation does not have true 120° rotational symmetry (one passage will have two wakes entering whilst the other two will have only one wake entering).

The simplified installation neglects a range of retarding torques to which the actual rotor is subject. Lee et al. (1975), Tsukamoto and Hutton (1985) and Cheesewright and Clark (1996) have given various mathematical representations for these torques. Tsukamoto and Hutton (1985) list individually, the following fluid related retarding torques: T_t, blade tip clearance drag torque; T_B, bearing retarding torque; T_w, hub disc friction torque; and T_b, rotor hub fluid drag torque. In addition, Cheesewright and Clark have discussed a non-fluid related component of drag, T_m, associated with the magnetic pick-up. Note that for the modelled installation there will be no calculation of T_t because zero tip clearance is assumed, no calculation of T_B because the bearing has not been analysed, no calculation of T_w and T_b because endwall boundary layers are not included. Although T_m is not included in the modelled installation either, the observation of Cheesewright and Clark that T_m would be more significant in gas flows suggests that its neglect may be justified. The overall effect of omitting the above mentioned torques would, however, be to over-predict

blade speed. It is nonetheless notable that the recent study of Caffrey et al. (1997), as mentioned above, does suggest for a larger 100mm rotor that fair predictions of steady rotor speed are possible, even where various sources of retarding torque are neglected.

8.2.2 Governing equations

Unsteady fluid motion is governed by basic physical laws relating to mass and momentum conservation embedded in the continuity and Navier-Stokes equations. Under the assumption of isothermal incompressible flow, the required forms of the continuity and Navier-Stokes equations are given below:

$$\nabla \cdot \boldsymbol{U} = 0 \qquad \textbf{Eq. 8. 1}$$

$$\underbrace{\rho\left[\frac{D\boldsymbol{U}}{Dt}\right]}_{\textit{inertia term}} = \underbrace{\boldsymbol{B}}_{\textit{body force term}} - \underbrace{\nabla p}_{\textit{pressure term}} + \underbrace{\mu\left[\nabla^2 \boldsymbol{U}\right] - \rho\nabla\left(\overline{u'u'}\right)}_{\textit{viscous term}} \qquad \textbf{Eq. 8. 2}$$

Where: $\boldsymbol{U}$ is vector velocity;

ρ is density;

t is time;

$\boldsymbol{B}$ is vector body force;

p is pressure;

μ is dynamic viscosity;

$\rho\nabla\left(\overline{u'u'}\right)$ is the phase average Reynolds stress (sometimes written as $-\rho\nabla\left(\overline{u'u'}\right)$, see Appendix C)

A Reynolds averaged formulation for the mean flow equations is used as the piped water flow is fully turbulent (Re $\approx 3.11\times10^4$) for the test cases considered. The stresses are determined by the often used low-Reynolds number k-ε turbulence model of Launder and Sharma (1974). (Further details of this model are given in Appendix C. 2.)

Now, the governing equations are most easily solved in a reference frame rotating with the meter blading. Since this frame is a non-inertial reference frame, additional body forces

arise in the momentum equation. These are included in the Navier Stokes equations via the body force $\boldsymbol{B}$.

For a frame rotating with angular velocity ω and acceleration $\dot{\omega}$, fluid acceleration in the absolute and relative frames are related by the expression (White 1998):

$$\left(\frac{d\boldsymbol{U}}{dt}\right)_{abs} = \underbrace{\left(\frac{d\boldsymbol{U}}{dt}\right)_{rel}}_{\text{rectilinear accel.}} + [\ \underbrace{\dot{\omega}\times\boldsymbol{r}}_{\text{tangential accel.}} + \underbrace{2\omega\times\boldsymbol{U}}_{\text{Coriolis accel.}} + \underbrace{\omega\times(\omega\times\boldsymbol{r})}_{\text{centripetal accel}}\ ] \qquad \textbf{Eq. 8. 3}$$

where $\boldsymbol{r}$ represents the position vector of the point in question.

Clearly, in transferring the Navier-Stokes equations from an absolute to a relative frame there are three additional terms corresponding to angular, Coriolis and centripetal accelerations. Thus, to account for frame rotation, the body force (per unit volume) $\boldsymbol{B}$ is set to:

$$\boldsymbol{B} = -\rho[\dot{\omega}\times\boldsymbol{r} + 2\omega\times\boldsymbol{U} + \omega\times(\omega\times\boldsymbol{r})] \qquad \textbf{Eq. 8. 4}$$

In a cylindrical coordinate system (r,θ,x) rotating about the axial direction, x axis, we obtain:

$$\boldsymbol{B}_r = \rho(2u_\theta\omega + r\omega^2) \qquad \textbf{Eq. 8. 5}$$

$$\boldsymbol{B}_\theta = -\rho(2u_r\omega + r\dot{\omega}) \qquad \textbf{Eq. 8. 6}$$

$$\boldsymbol{B}_x = 0 \qquad \textbf{Eq. 8. 7}$$

Where u_r, u_θ, u_x are the components of velocity; and,

$\boldsymbol{B}_r$, $\boldsymbol{B}_\theta$, $\boldsymbol{B}_x$ are the three components of the body force in the r, θ, x directions.

To evaluate the components of $\boldsymbol{B}$ (Eqs. 8. 5, 8. 6 and 8. 7), the angular velocity, ω, and acceleration, $\dot{\omega}$, of the frame are required. As the motion of the frame follows the motion of the meter blades, the required quantities can be obtained from an equation for the rotational motion of the meter blades. Thus, the angular acceleration of the frame, $\dot{\omega}$, is obtained from the net torque turning the rotor, T_N, as:

$$\dot{\omega} = \frac{T_N}{I_R} \qquad \textbf{Eq. 8. 8}$$

where I_R is the inertia of the rotor.

The angular velocity of the frame, ω, is then determined by integration:

$$\omega = \int \dot{\omega} dt \qquad \textbf{Eq. 8. 9}$$

In the present method, the net torque, T_N, can be obtained by an integral of forces over the blade surface;

$$T_N = \int_{\substack{blade \\ surface}} p \cdot r dA_\theta + \int_{\substack{blade \\ surface}} r(\tau_{\theta\theta} dA_\theta + \tau_{r\theta} dA_r + \tau_{x\theta} dA_x) \qquad \textbf{Eq. 8. 10}$$

Where r is radius;

p is the pressure acting on the elemental blade surface;

dA_x, dA_r, dA_θ are the elemental areas in the x, r, θ directions; and,

$\tau_{\theta\theta}, \tau_{r\theta}, \tau_{x\theta}$ are the components of the shear stress tensor.

Boundary conditions on U and p (Eqs. 8.1 and 8.2) are required on the cyclic, inlet, outlet and wall boundaries (on the blade, hub and case surfaces).

The simplest treatment is for the cyclic boundaries at which periodic conditions are applied. For the inlet, velocity is made uniform over the pipe annulus. In steady flow, it is fixed in time so as to match the measured volume flow. For unsteady flow, a sinusoidally pulsating variation is assumed:

$$U_x(t) = \overline{U_x}(1 + \alpha_p \sin 2\pi f_p t) \qquad \textbf{Eq. 8. 11}$$

with α_p being the relative pulsation amplitude and f_p being the pulsation frequency.

Uniform inlet values for k and ε were also used. They are set at the values which are based upon the characteristic of a fully developed pipe flow. (Details are given in Appendix C.3.1.)

At the blade surface boundaries, standard no-slip conditions (zero flow velocity) with zero values for k and ε are used. However, the endwall boundary layers at the hub and casing are not resolved and a shear free slip condition is used.

A more complex treatment is required at the flow exit than for the other flow boundaries. Pressure is set at the exit boundary; however it is not initially clear how it should vary over the exit plane. We desired that the exit boundary condition should be equivalent to an infinite (or at least very long) exit duct without having to actually extend the grid to infinity.

A conceptual problem arises with an assumption of uniform pressure if the exit flow emerges from the rotor with swirl. This is because uniform pressure is not compatible with a swirling flow which must have a lower pressure at its core to maintain the swirling motion. Thus, this type of boundary condition yields results far removed from the solution that would have been obtained for an infinite exit duct for which swirling motion would not be restricted.

A better solution is to set the pressure distribution assuming radial equilibrium. With a reference pressure value specified in the hub, the distribution of pressure is evaluated using the following equation, for the absolute reference frame, which balances centripetal acceleration and radial pressure gradient:

$$\frac{1}{\rho}\frac{\partial p}{\partial r} = \frac{u_\theta^{\,2}}{r} \qquad \textbf{Eq. 8. 12}$$

In the presence of swirl the radial equilibrium boundary condition is commonly used in turbo-machinery calculations. This type of boundary condition is compatible with the existence of exit swirl and should yield results closer to the desired infinite duct solution.

8.2.3 Computational mesh

Figures 8.4 and 8.5 shows the computational grid for the simulation of the flow through meter B. Note that the calculations are carried out for a 120° segment, although the full 360° is shown for clarity. In Figure 8.5, we see that the mesh is formed as an "O-mesh" surrounding the blades embedded within an "H-mesh". There are 15 spanwise nodes from hub to tip, and the distance of the first node centre from both surfaces is situated at a y^+ value of 30. There are 30 nodes from blade to blade across the boundary layer in the O-mesh and the first cell centre from the blade surface is situated at a distance where the y^+ value is at 0.3. The total number of nodes is 36580. The inlet is situated approximately 2 times the blade chord length upstream. The outlet is situated approximately 3 times the blade chord length downstream.

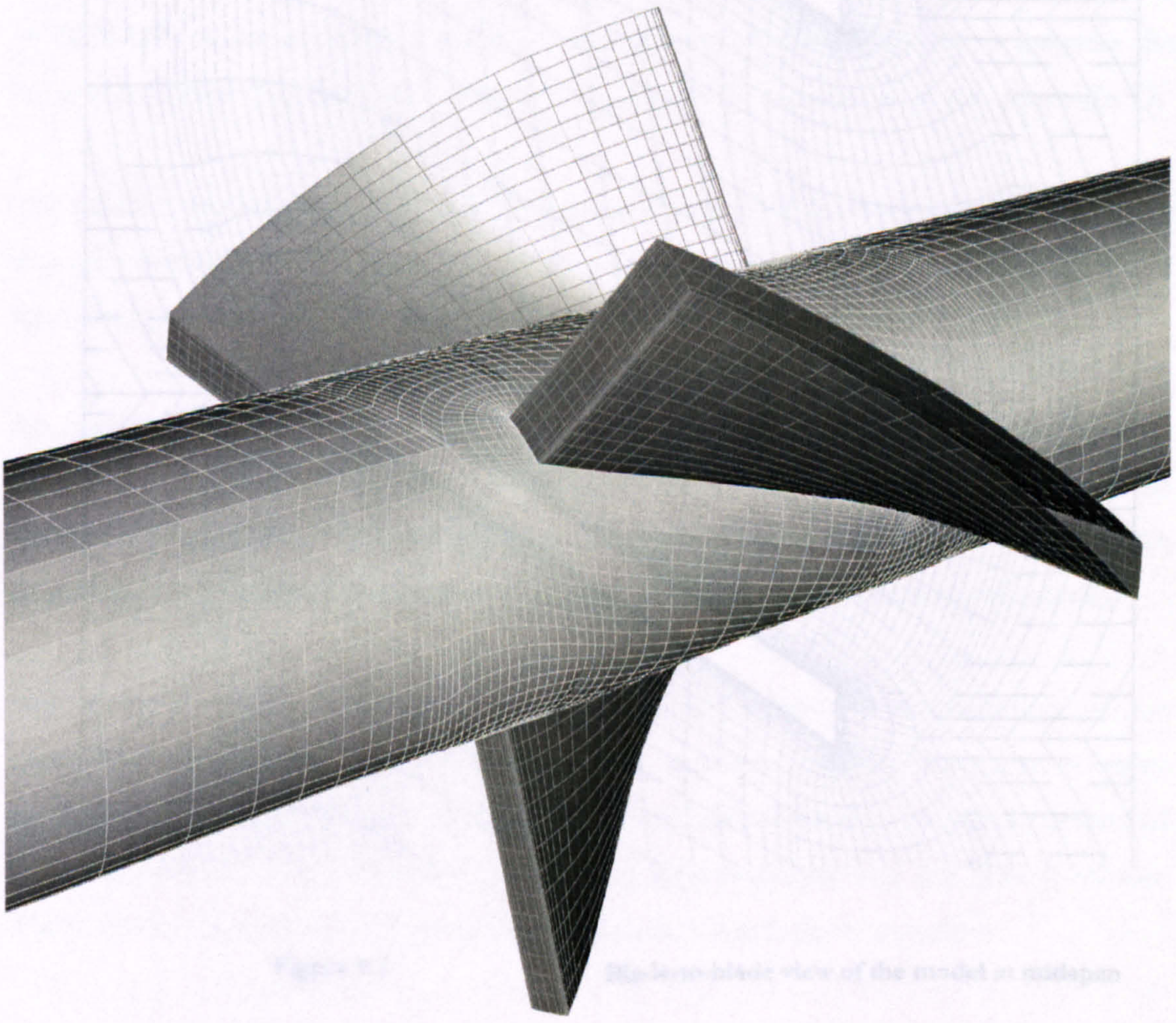

Figure 8.4 **Grid showing hub and blades of the rotor of meter B**

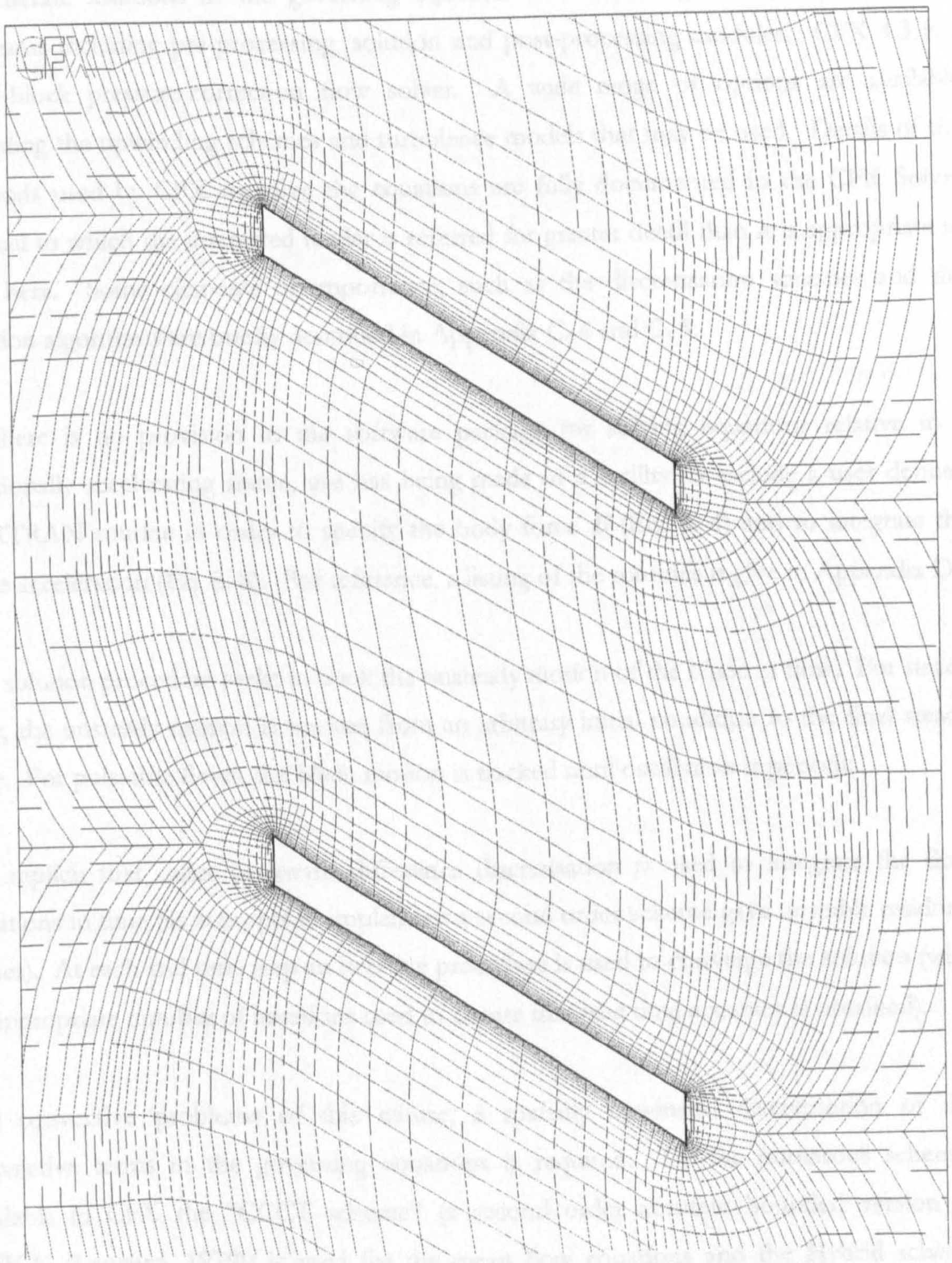

Figure 8.5 **Blade-to-blade view of the model at midspan**

8.2.4 Solution procedure

A commercial CFD software package, CFX Version 4.3 (AEA Technology Ltd.), was used to generate solutions to the governing equations. The package comprises a suite of programs including pre-processing, solution and post-processing modules. CFX 4.3 is a multi-block pressure-correction flow solver. A wide range of options are available regarding the upwinding schemes and turbulence models that may be used. Details of the methods used by CFX to solve the equations are fully documented in the CFX Solver Manual to which the interested reader is referred for greater detail than it is appropriate to give here. Some elements of importance, such as the discretisation schemes and the solution algorithms are briefly described in Appendix C. 4 and C. 5.

As there is no provision in the software package for solving equations relative to a rotationally accelerating frame, use has being made of a facility to include a user defined FORTRAN routine in order to specify the body force $\boldsymbol{B}$ (Eq. 8. 4) and to integrate the blade acceleration (Eq. 8. 8). For reference, a listing of the routines is give in Appendix D.

The solution procedure seeks to track the unsteady motion of the blade in time. For steady flow, the unsteady motion is tracked from an arbitrary initial condition to the final steady state. For pulsating flows, the blade motion is tracked until oscillation is periodic.

An implicit first order backward difference discretisation is used to integrate the flow equations in time (as attempts to implement a second order scheme gave unstable residuals values). At each real time step an iterative procedure is used to converge the solution (with an appropriate number of iterations used to ensure that true time accuracy is obtained).

For convective problems of this nature, a spatially upwinded discretisation of the convective terms in the governing equations is required. Of the numerous schemes available in CFX the "CCCT scheme" (a second order accurate bounded version of QUICK (Leonard, 1979)) is used for the mean flow equations and the Hybrid scheme (Pantankar and Spalding, 1972) is used for the less stable turbulence equations.

8.3 Steady Flow Analyses

8.3.1 Test cases

The ability of the simulation to predict the steady flow performance of the meter was first assessed. Six flow conditions were examined, denoted S1 to S6, and are listed in Table 8.1. Note that these conditions span the linear flow range of the meter (Appendix A). The experimental steady flow condition, about which pulsating flow tests were carried out for this meter, is included as case S6 in the Table.

Case No.	Pipe volume flow rate ($\times 10^{-3}$ $m^3 s^{-1}$)	Domain inlet mass flow rate (kg s^{-1})	Inlet velocity (ms^{-1})	Reynolds number ($\times 10^4$)	Length of time step ($\times 10^{-4}$ s)	No. of steps	No. of iterations per step
S1	0.144	0.048	1.298	1.7	5	200	6
S2	0.303	0.101	2.720	3.5	5	200	6
S3	0.756	0.252	6.788	8.8	5	200	6
S4	1.211	0.404	10.880	14.1	5	200	6
S5	1.667	0.556	14.973	19.3	5	200	6
S6	0.292	0.097	2.615	3.5	5	200	6

Table 8. 1 Meter B — Steady flow conditions and the corresponding simulation settings

Each steady flow run is marched in time from an approximate initial condition to steady state when the net torque acting on the rotor becomes zero and its speed remains constant. Only the final condition is of significance.

Representative histories for predicted blade acceleration and speed are shown in Figures 8.6 and 8.7 respectively. We see that a steady state blade speed is achieved after about 100 time steps.

Convergence is examined more closely in Figure 8.8 which shows representative plots of the residuals for the mean flow and turbulence equations and for the mass fluxes. A reduction of between five and six orders of magnitude is achieved over 200 steps confirming that the final solution is indeed steady. For each case the run time is about two hours on a Sun UltraSparc Ultra™ 10 workstation with 440-MHz UltraSPARC-IIi processor and 256MB physical memory.

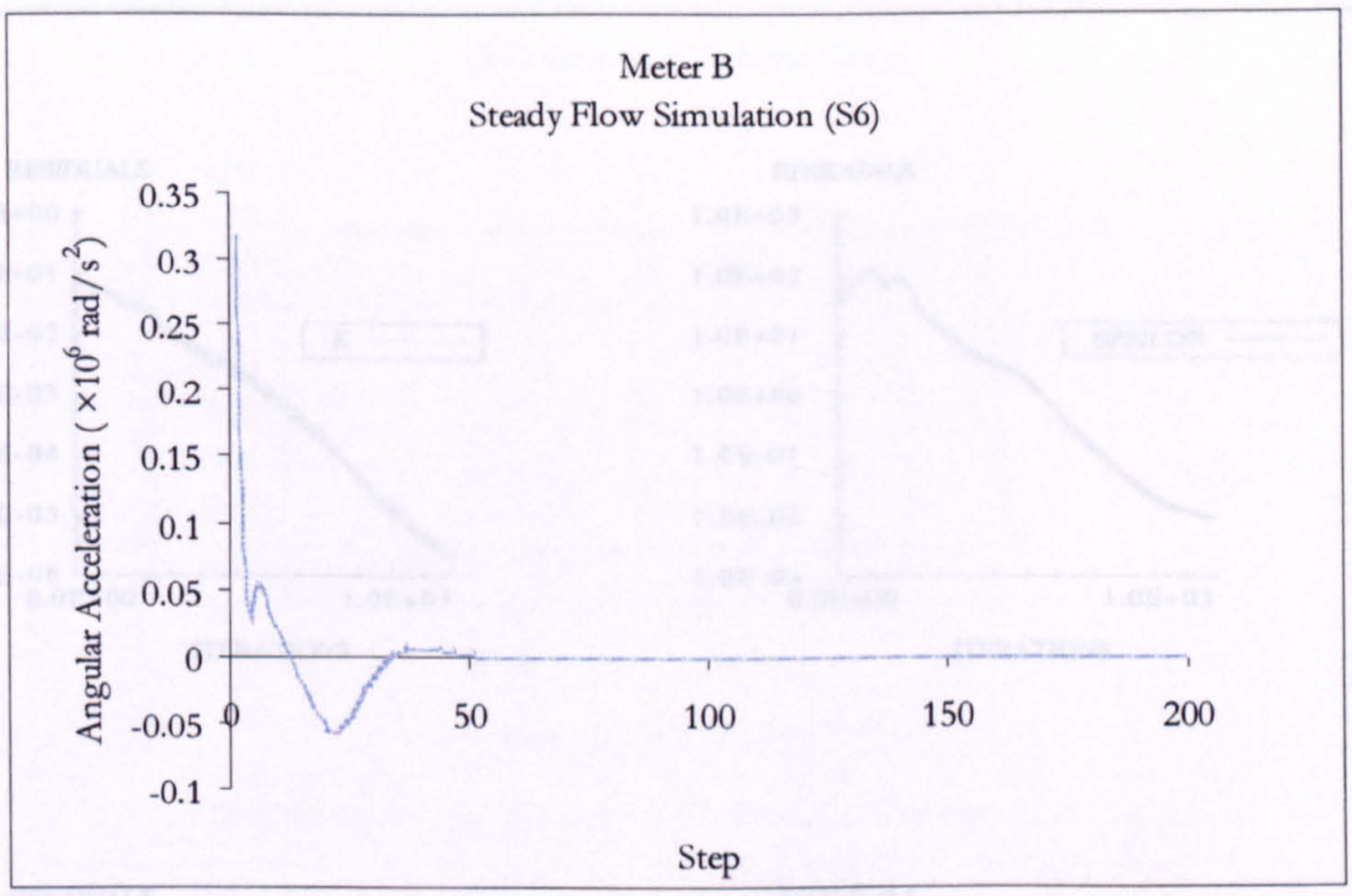

Figure 8. 6 **Meter B, S6 — Simulated angular acceleration versus no. of time step, $\Delta t = 5 \times 10^{-4}$ s, 6 iterations each Δt, input flow rate = 0.292×10^{-3} m^3/s.**

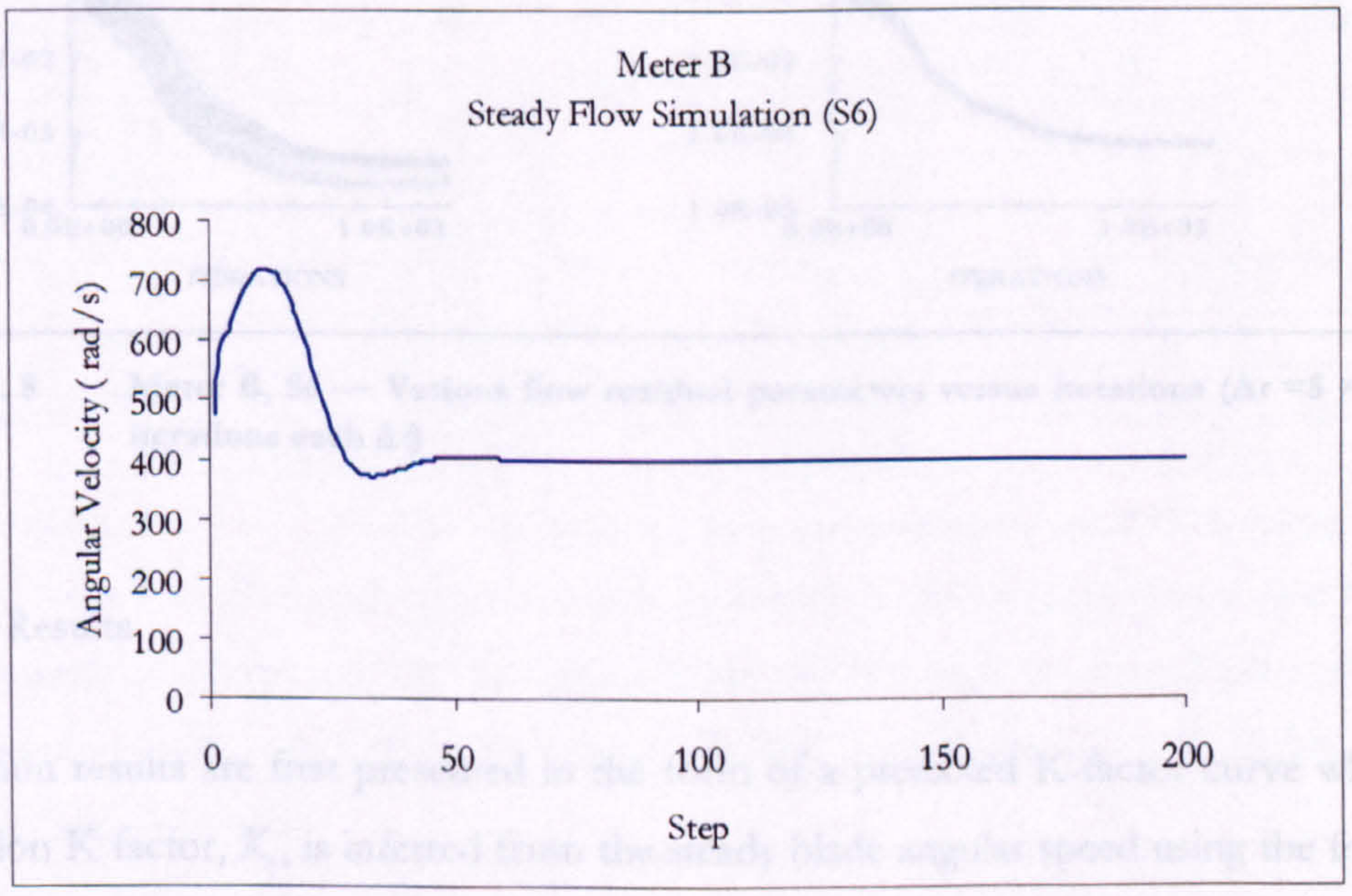

Figure 8. 7 **Meter B, S6 — Simulated angular speed versus no. of time step, $\Delta t = 5 \times 10^{-4}$ s, 6 iterations each Δt, input flow rate = 0.292×10^{-3} m^3/s**

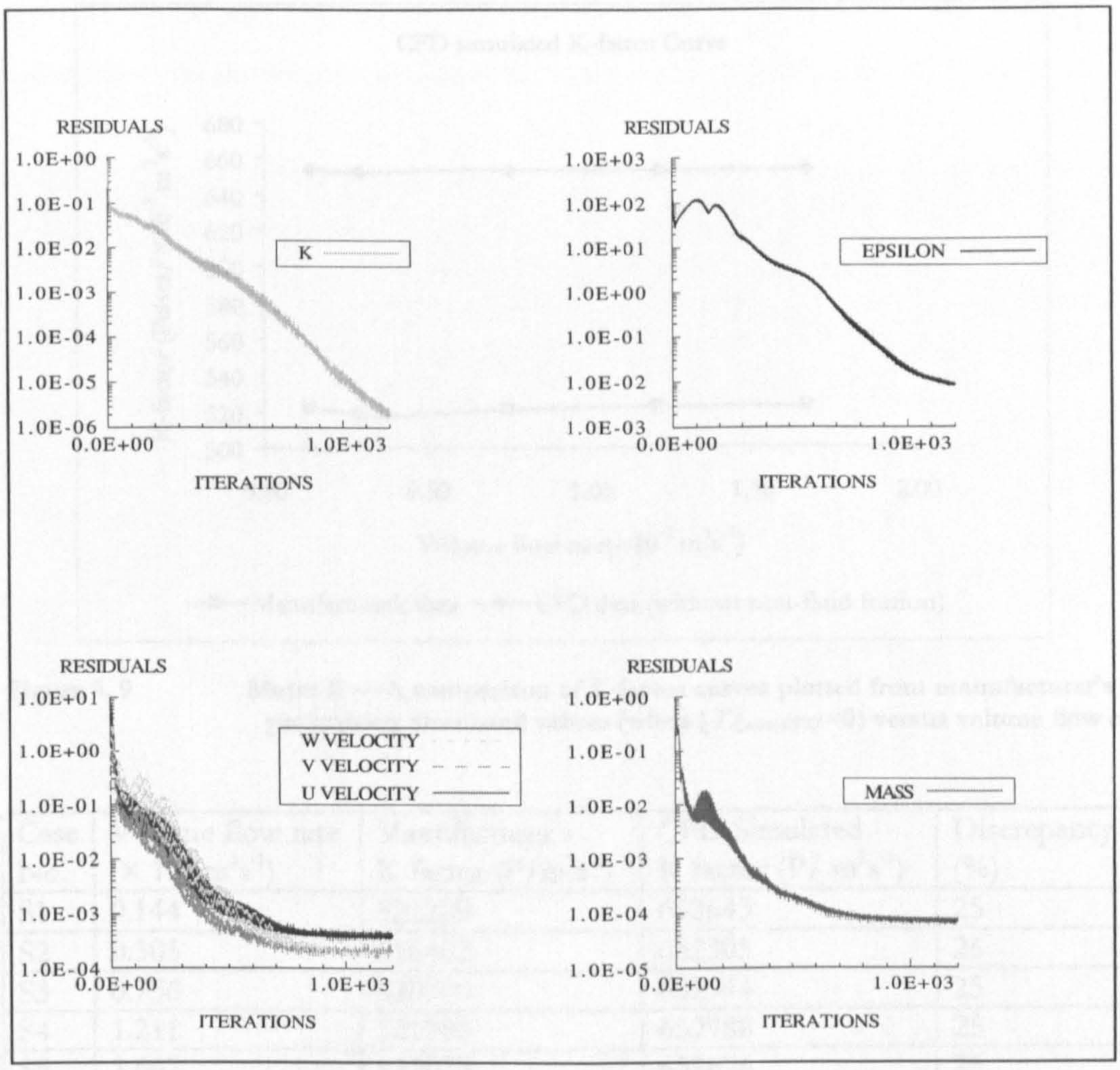

Figure 8. 8 Meter B, S6 — Various flow residual parameters versus iterations (Δt =5 × 10^{-4} s, 6 iterations each Δt)

8.3.2 Results

Simulation results are first presented in the form of a predicted K-factor curve where the simulation K factor, K_s, is inferred from the steady blade angular speed using the following equation:

$$K_s = (3\omega/2\pi) \div \dot{V}_{in} \qquad \textbf{Eq. 8. 13}$$

In this equation the factor 3 arises since there are three blades, whence the blade passing frequency f_b will be $3\omega/2\pi$. The derived curve is compared with manufacturer's data in Figure 8.9 and numerical results are tabulated in Table 8.2. The notation $[T_r]_{non\text{-}CFD}$ represents that there are no retarding torques included in the simulation (as mentioned in Section 8.2.1)

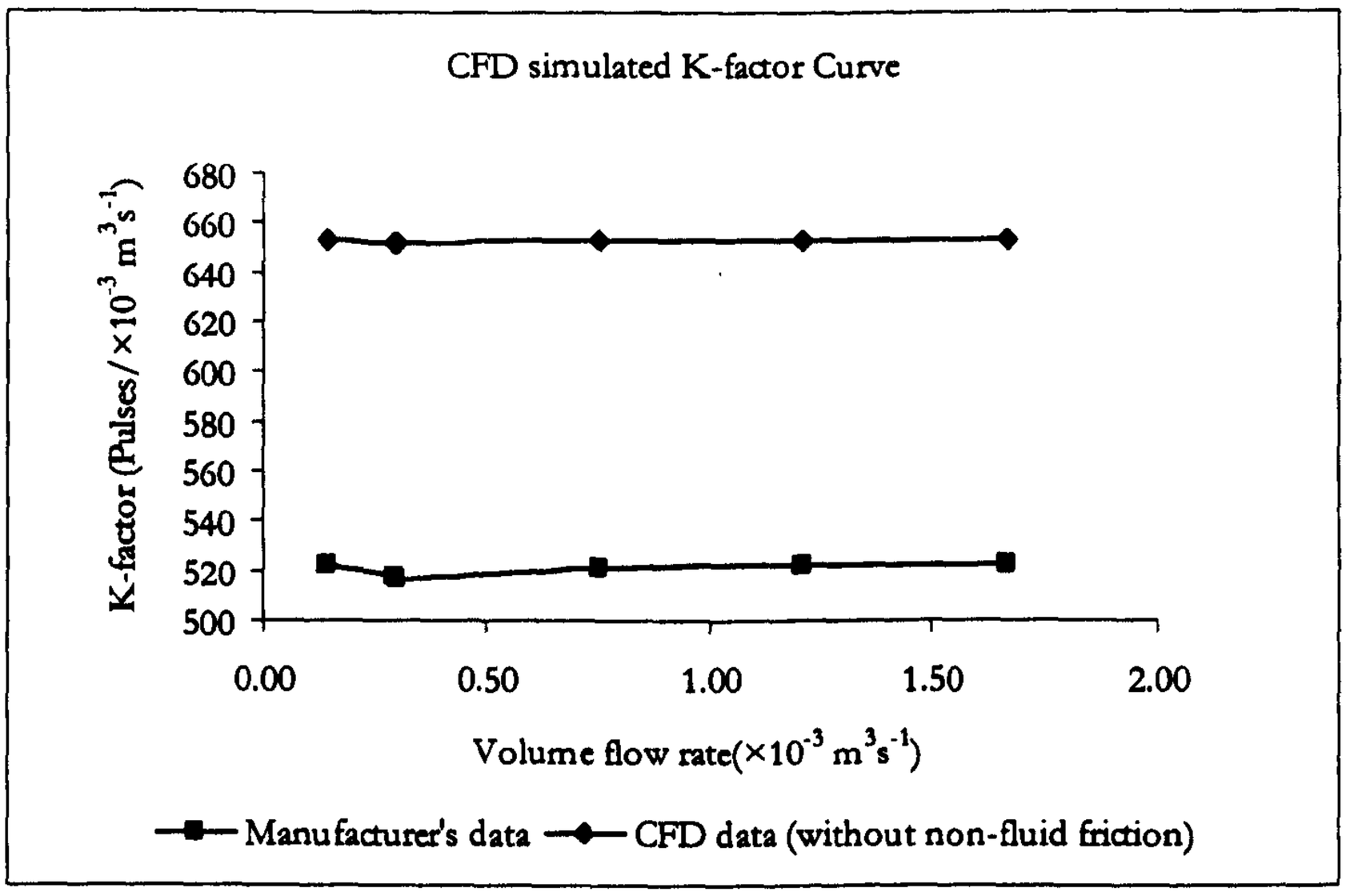

Figure 8. 9 **Meter B — A comparison of K-factor curves plotted from manufacturer's and preliminary simulated values (when $[T_r]_{non\text{-}CFD}$=0) versus volume flow rates**

Case No.	Volume flow rate ($\times 10^{-3}$ m^{3}s^{-1})	Manufacturer's K factor (P/m^{3}s^{-1})	CFD Simulated K factor (P/ m^{3}s^{-1})	Discrepancy (%)
S1	0.144	522209	652643	25
S2	0.303	516402	652305	26
S3	0.756	520700	652944	25
S4	1.211	521980	652988	25
S5	1.667	522070	652876	25
S6	0.292	520331	652329	25
	Average:	520615	652681	25

Table 8. 2 **Meter B — K-factor values of manufacturer's and CFD simulation**

It can be seen that the linear meter response (constant K-factor) is predicted over the flow range examined, however the predicted value of K-factor is 25% higher than the manufacturer's data. In effect, the predicted blade speed will be 25% higher than is measured experimentally.

Flow profiles on blade-to-blade sections at root-mean-square (rms) radius are shown for case S6 in Figures 8.10 to 8.12 to illustrate the predicted flow field in the region of the meter blade. Figures 8.10 and 8.11 show the distribution of pressure and velocity vectors in the region of the blade. Figure 8.12 shows contours of vorticity which more readily reveals the behaviour of the viscosity affected regions of the flow.

It is seen that strong adverse pressure gradient downstream of the leading edge corners forces the flow to separate. The flow reattaches for both upper and lower surfaces at

around 10% chord and remains attached to the trailing edge corners. The trailing edge wake is quite stable showing no tendency to shed vorticity periodically.

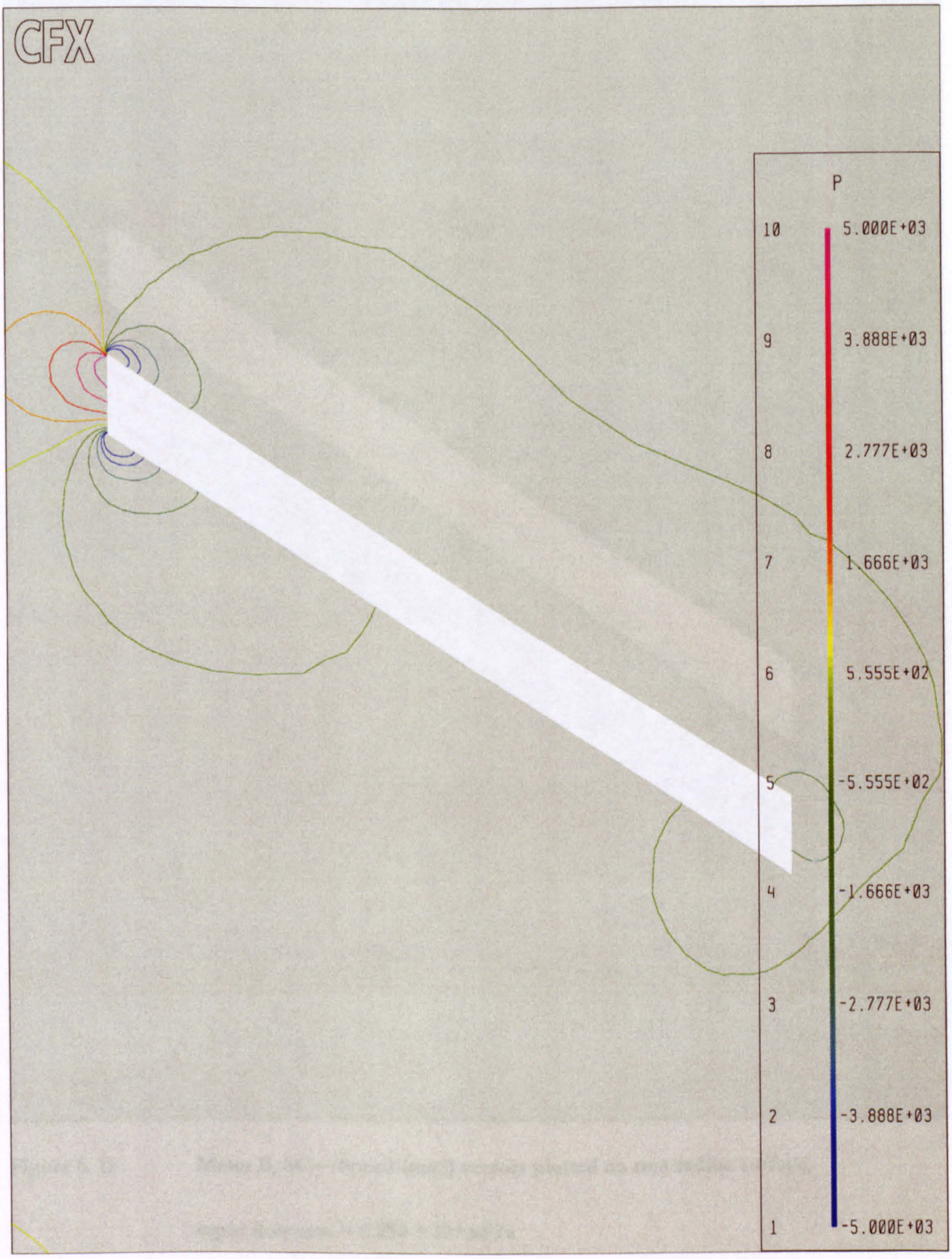

Figure 8. 10 **Meter B, S6 — Pressure (Pa) contour plotted on rms radius surface, input flow rate = 0.292×10^{-3} m^3/s**

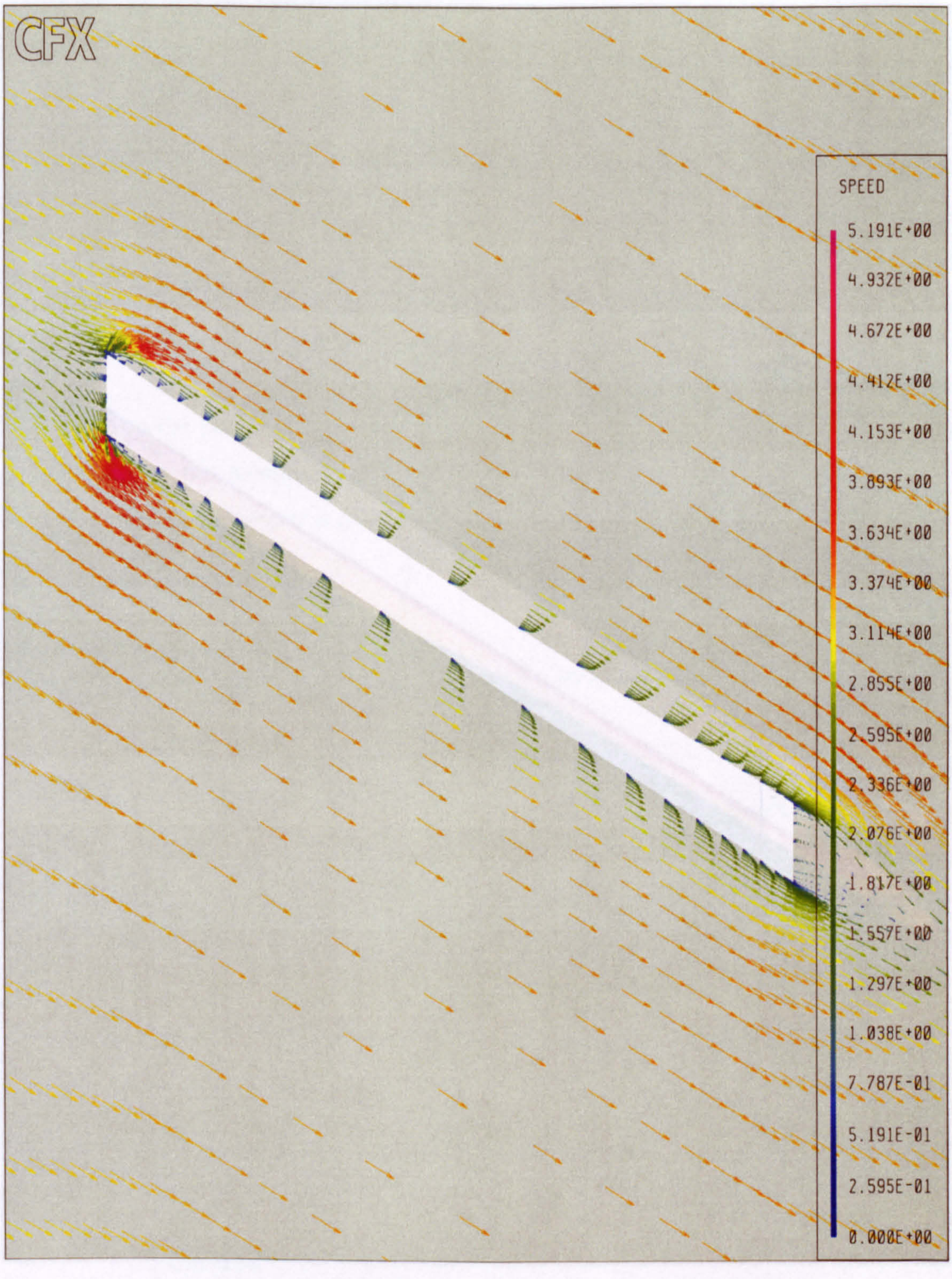

Figure 8. 11 **Meter B, S6 — Speed (ms^{-1}) vectors plotted on rms radius surface, input flow rate = 0.292×10^{-3} m^3/s**

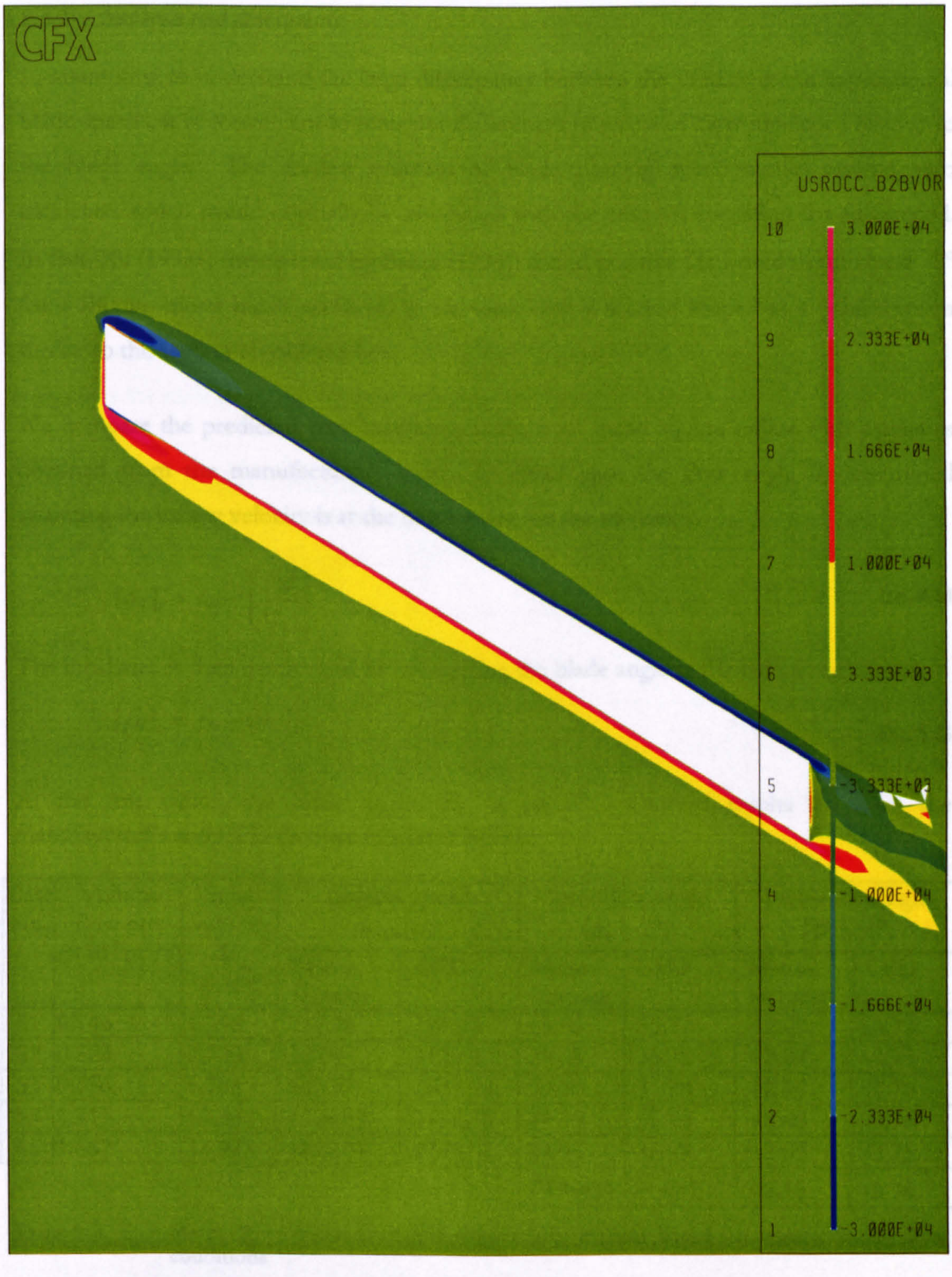

Figure 8. 12 **Meter B, S6 — Vorticity plotted on rms radius surface,**

input flow rate = 0.292×10^{-3} m^3/s

8.3.3 Analysis and discussion

In attempting to understand the large discrepancy between the predicted and experimental blade speeds, it is convenient to interpret differences in terms of flow incidence relative to the blade angle. The crudest estimate of blade running speed would assume zero incidence, which would normally be associated with the zero lift condition for an aerofoil. In fact, Xu (1992a) (interpreted by Baker (1993)) found positive lift would occur above -2° for a 100mm meter blade examined in his work with a section shaped as a parallelogram similar to the section considered here.

We compare the predicted flow incidence at the root mean square radius with estimates obtained from the manufacturer's data. In either case the flow angle is determined assuming the inflow velocity is at the mean value for the section:

$$[\phi_{in}]_{\bar{r}} = \tan^{-1}\left[\frac{\bar{r}\omega}{U_x}\right] \qquad \textbf{Eq. 8.14}$$

The incidence is then determined by subtracting the blade angle at the radius considered:

$$[\beta_i]_{\bar{r}} = \beta_{\bar{r}} - [\phi_{in}]_{\bar{r}} \qquad \textbf{Eq. 8.15}$$

At the rms radius, the blade angle, $\beta_{\bar{r}}$, is 32.02°. Derived results for both the manufacturer's and CFD data are tabulated below:

Case No.	Volume flow rate ($\times 10^{-3}$ m^3/s)	Inlet velocity U_x (m/s)	Angular speed ω (rad/s)		Inlet flow angle $[\phi_{in}]_{\bar{r}}$ (°)		Incidence Angle $[\beta_i]_{\bar{r}}$ (°)	
			Manu-facturer	CFD	Manu-facturer	CFD	Manu-facturer	CFD
S1	0.144	1.298	157.98	197.44	29.96	35.77	+2.07	-3.74
S2	0.303	2.720	327.47	413.65	29.68	35.75	+2.34	-3.73
S3	0.756	6.788	823.97	1033.24	29.89	35.78	+2.14	-3.76
S4	1.211	10.880	1324.03	1656.33	29.95	35.78	+2.08	-3.76
S5	1.667	14.973	1822.37	2278.97	29.95	35.78	+2.07	-3.75
					Average $[\beta_i]_{\bar{r}}$ =		**+2.15**	**-3.74**

Table 8. 3 Meter B — Flow incidence angles (rms radius) based on various steady flow conditions

It can be seen that the predicted flow incidence is near -3.74° whilst the manufacturer's data are close to +2°. The difference of 6° coincides with the large speed error of 25%. It is notable that the CFD data is comparable to the result given by Xu (positive lift starts from -2°). The discrepancies might then reasonably be attributed to various retarding torques not accounted for in the modelled geometry.

8.4 Pulsating Flow Analyses

8.4.1 Test cases

As previously stated, runs for the pulsating flow cases have been carried out for the mean condition of case S6. Three pulsation frequencies, f_p, and three pulsation amplitudes, α_p ,are considered giving a total of nine cases. These are denoted P1 to P9 and the conditions for each test are shown below in Table 8.4.

Case No.	Pulsation frequency f_p (Hz)	Pulsation amplitude α_p (%)	No. of pulsation cycle	No. of iterations per step	Time step length (°)
P1	20	16.95	2	9	1
P2		28.02	2	9	1
P3		41.98	2	9	1
P4	40	16.57	2	9	1
P5		26.16	2	9	1
P6		40.63	2	9	1
P7	60	16.65	2	9	1
P8		28.13	2	9	1
P9		36.69	2	9	1

Table 8. 4 Meter B — Pulsating flow conditions and the corresponding simulation settings

For each case the run begins from the steady flow result obtained for case S6. The solution is then marched in time subject to sinusoidal pulsation of the volume flow until periodic oscillation of the blade is established. (It should be borne in mind that a pure sinusoidal pulsation is assumed, which is not exactly the case for some experimental tests due to some distortions at lower frequency pulsations.)

Finally, the simulated meter volume flow, $\dot{V}_s$, can then be inferred from the K-factor computed in the steady flow analysis using the following equation:

$$\dot{V}_s = (3\omega/2\pi) \div K_s \qquad \textbf{Eq. 8. 16}$$

In these cases the development of the solution as marching proceeds is crucially important. For solutions to be considered acceptably, we require the following three conditions:

i. a sufficient number of cycles are computed for periodic pulsation

ii. at each time step, a sufficiently large number of iterations must be used to ensure the flow equations are solved

iii. a sufficiently small time step is adopted for time accuracy to be obtained

A number of tests have been carried out to assess these three conditions.

Results of a representative test run to assess periodicity of the solution is shown in Figure 8.13. The figure compares the input volume flow with the simulated meter flow derived from the computed blade speed using Eq. 8.16. Four cycles are computed, and the derived mean flow and peak-to-peak amplitude are compared for second, third and fourth cycles in Table 8.5. In this case, it is concluded that two cycles are sufficient to establish periodic blade oscillation. In fact, this was found to be true for all nine cases examined.

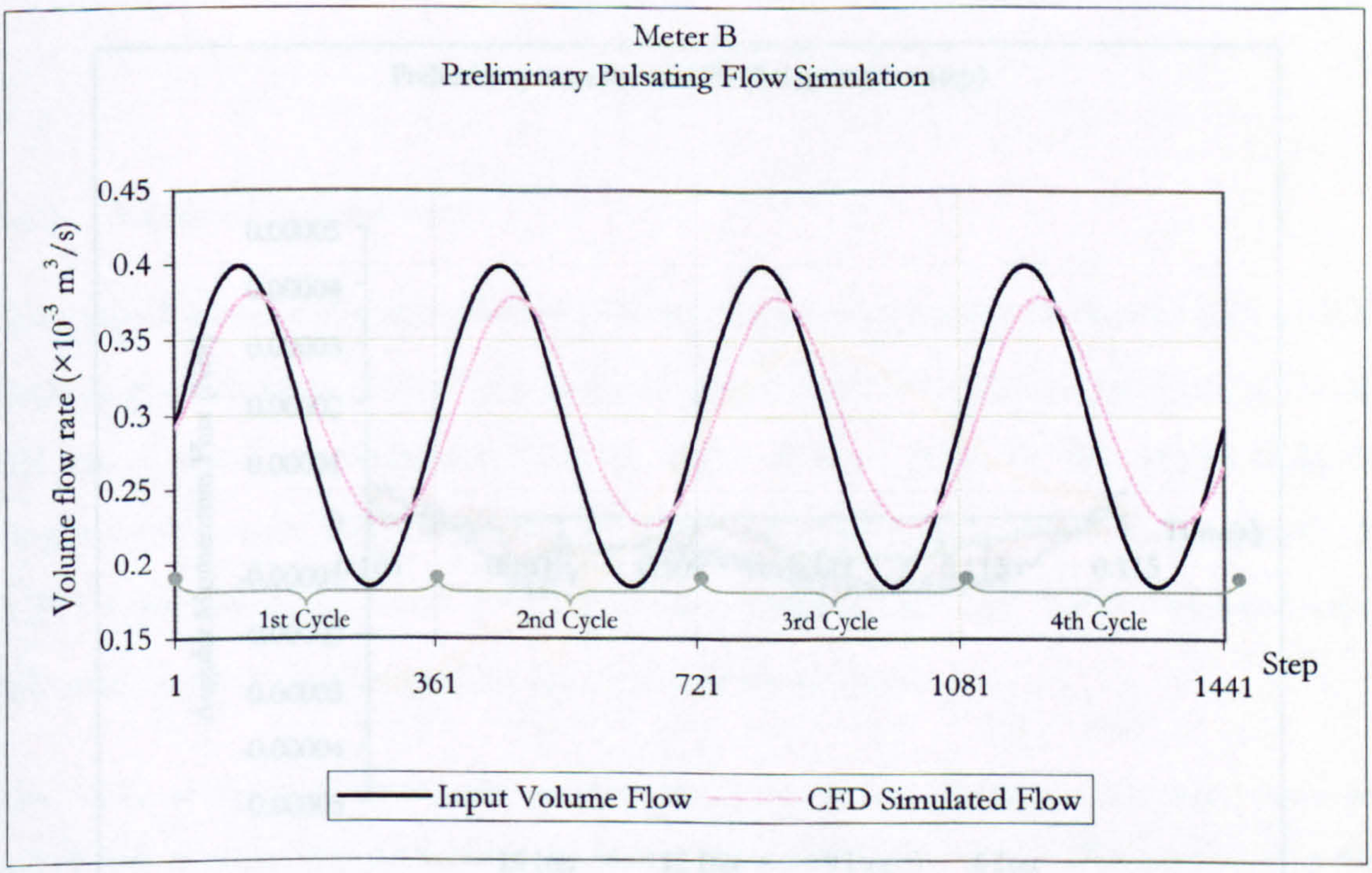

Figure 8. 13 **Preliminary pulsating flow simulation, P9 — flow inferred from simulated angular speed versus no. of time step**

Cycle	Simulated mean flow rate $\overline{\dot{V}_s}$ ($\times 10^{-3}$ m^3/s) (to 6 s.f.)	Simulated pk-pk flow amplitude $[\dot{V}_s]_{pk-pk}$ ($\times 10^{-3}$ m^3/s) (to 6 s.f.)
Second	0.298917	0.152301
Third	0.298897	0.152291
Forth	0.298897	0.152292

Table 8. 5 **Meter B — Comparison of simulation results between the second and third pulsating cycle**

In order to assess the effect of varying the number of iterations used at each time step, we have examined the balance of terms in an equation for angular momentum. This is considered in more mathematical detail in Section 8.5, however, for the purposes of the present discussion we note that the net flux of angular momentum into the rotor domain should be balanced by the rate of increase of angular momentum for the fluid and for the rotor. This balance was found to be particularly sensitive to the number of iterations employed. The imbalance in the various terms is shown in Figure 8. 14 as the number of iterations varies from 6 to 15. We see that the magnitude of the imbalance reduces as the number of iterations increases. At nine iterations the level of the imbalance is, in fact, less than 1% of the maximum term in the angular momentum equation for the rotor (see Figure 8.34 in Section 8.5). We thus conclude that the equations are satisfactorily solved using nine iterations per time step.

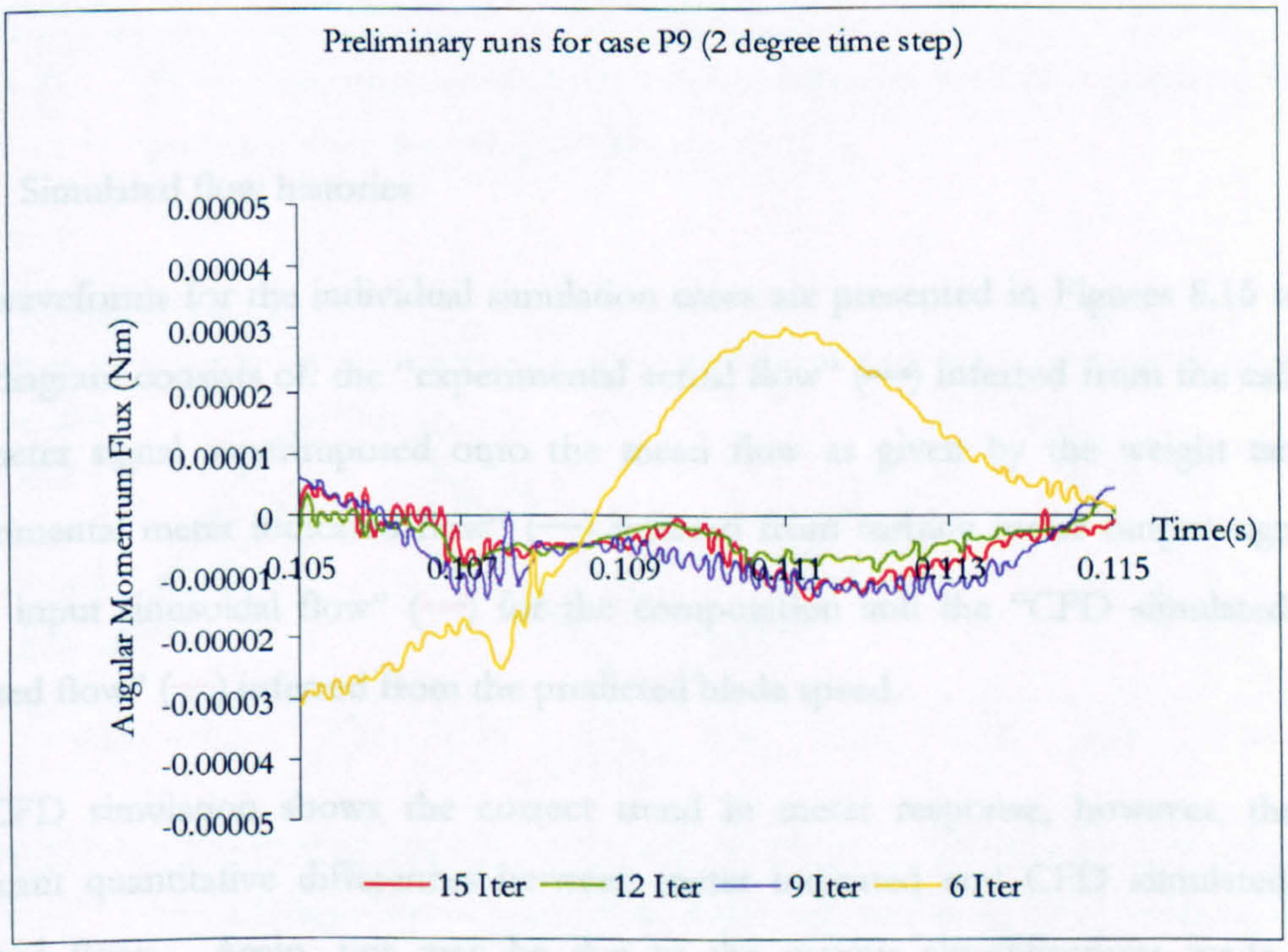

Figure 8. 14 **Preliminary runs, P9 — Sum of Angular Momentum Flux within the domain versus time, 2 degree time step per cycle with various number of iterations per time step.**

In Figure 8.15 the effect of varying time step on the computed variation of the blade speed is examined at 0.5°, 1° and 2° steps. Clearly, there is little difference in results and the solution can be considered to be time accurate at 1° steps.

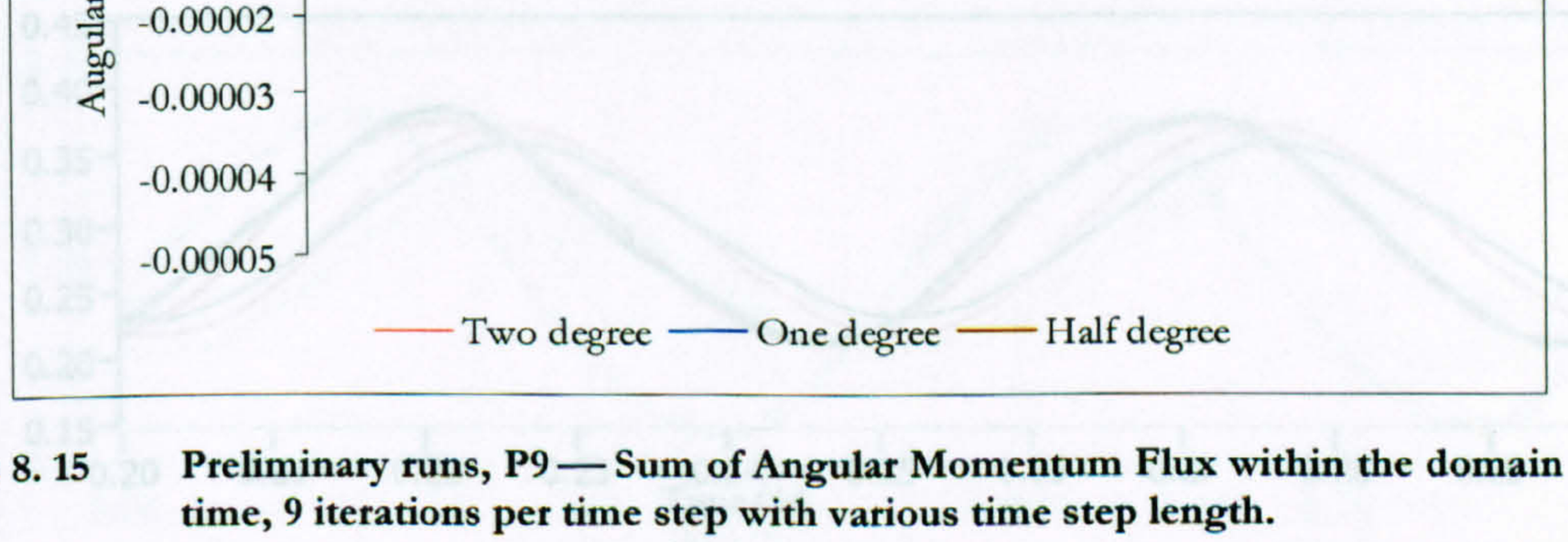

Figure 8. 15 Preliminary runs, P9 — Sum of Angular Momentum Flux within the domain versus time, 9 iterations per time step with various time step length.

8.4.2 Simulated flow histories

Flow waveforms for the individual simulation cases are presented in Figures 8.16 to 8.24. Each diagram consists of: the "experimental actual flow" (—) inferred from the calibrated EM meter signal superimposed onto the mean flow as given by the weight tank; the "experimental meter indicated flow" (—) inferred from turbine meter output signal; the "CFD input sinusoidal flow" (—) for the computation and the "CFD simulated meter indicated flow" (—) inferred from the predicted blade speed.

The CFD simulation shows the correct trend in meter response, however, there are significant quantitative differences between meter indicated and CFD simulated meter indicated flows. Again, this may be due to the various simplifications made in the modelled geometry.

P1: f_p= 20 Hz, α_p= 16.95 %

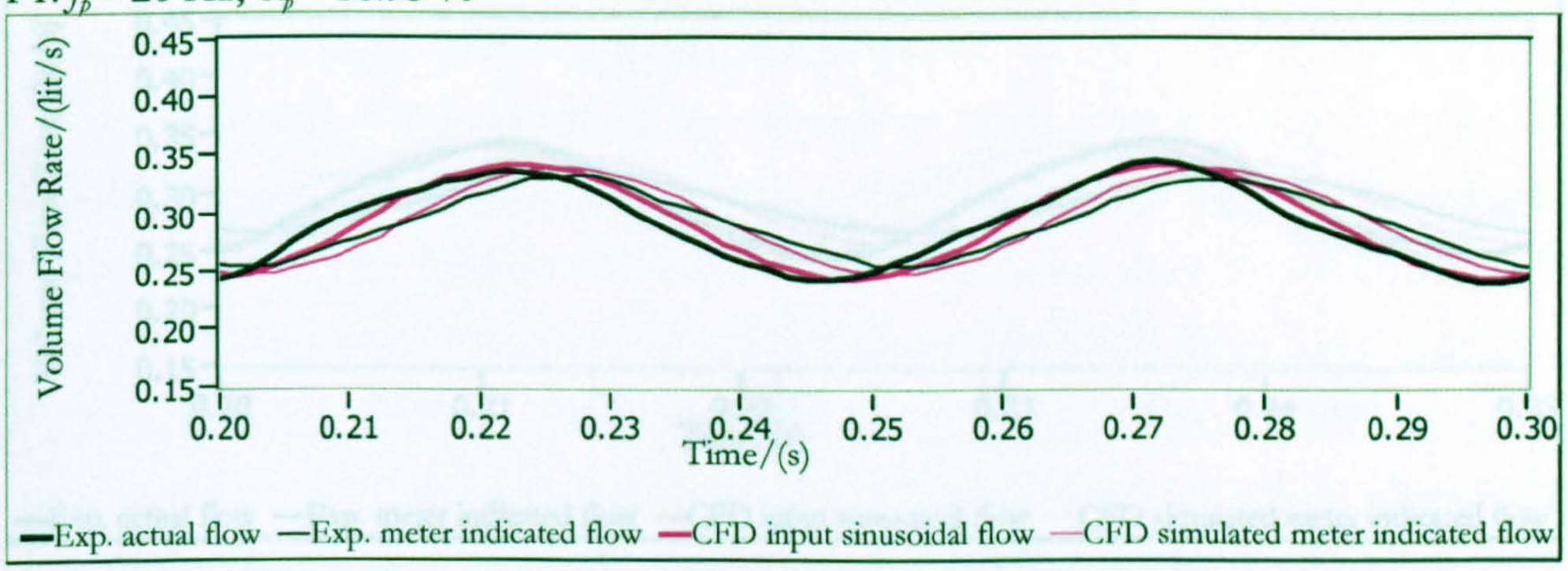

Figure 8. 16 **P1 — Comparison of actual flow, meter indicated flow, CFD simulated flow and predicted meter flow; at f_p= 20 Hz, α_p= 16.95%.**

P2: f_p= 20 Hz, α_p= 26.16 %

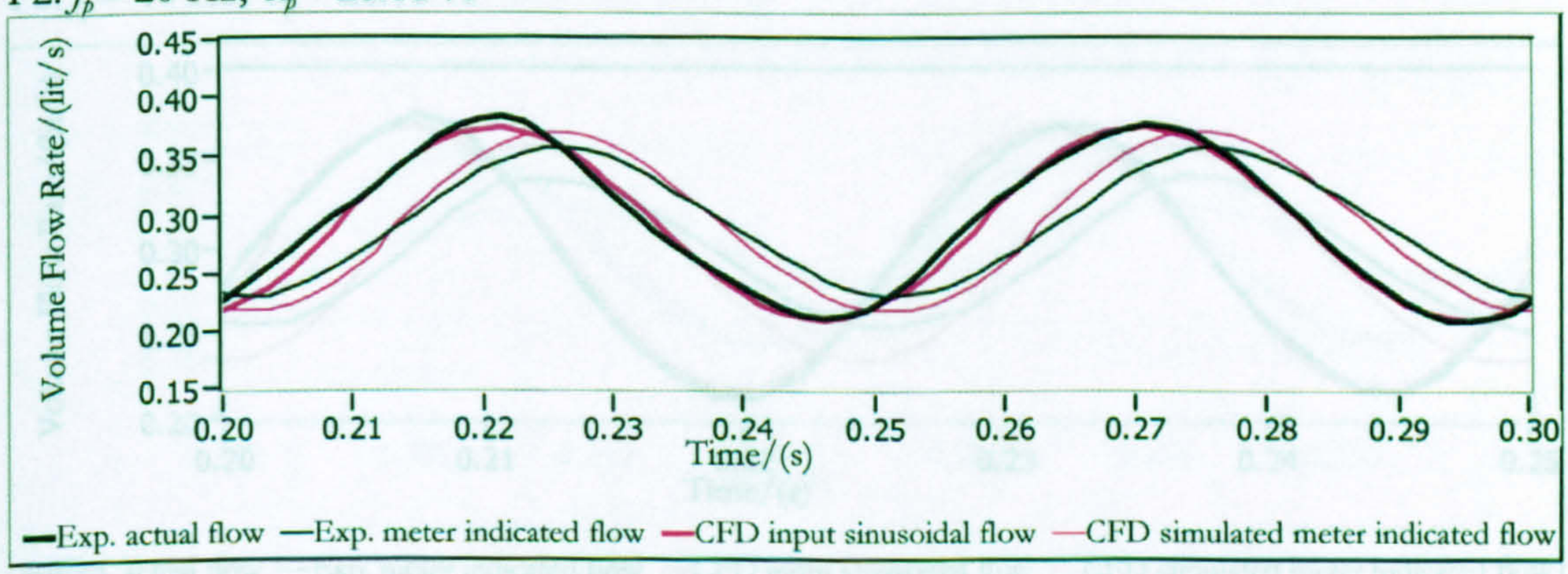

Figure 8. 17 **P2 — Comparison of actual flow, meter indicated flow, CFD simulated flow and predicted meter flow; at f_p= 20 Hz, α_p= 26.16 %.**

P3: f_p= 20 Hz, α_p= 41.98 %

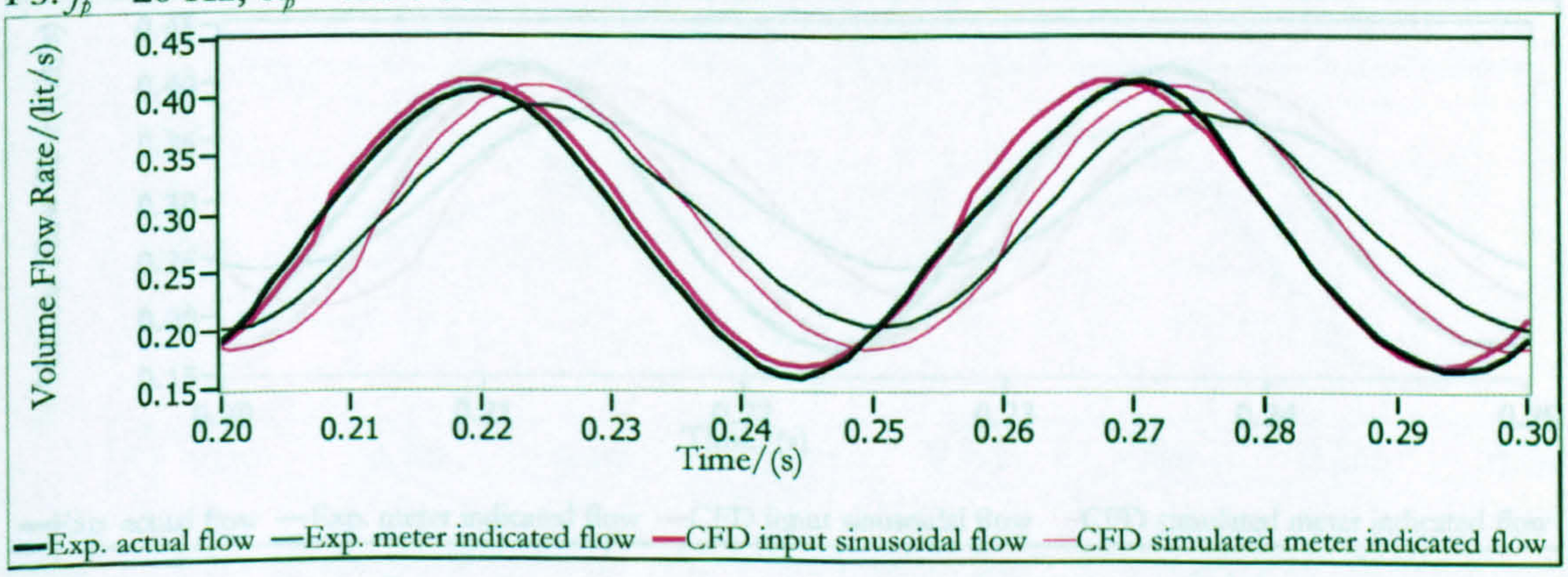

Figure 8. 18 **P3 — Comparison of actual flow, meter indicated flow, CFD simulated flow and predicted meter flow; at f_p= 20 Hz, α_p= 41.98 %.**

P4: f_p= 40 Hz, α_p= 16.57 %

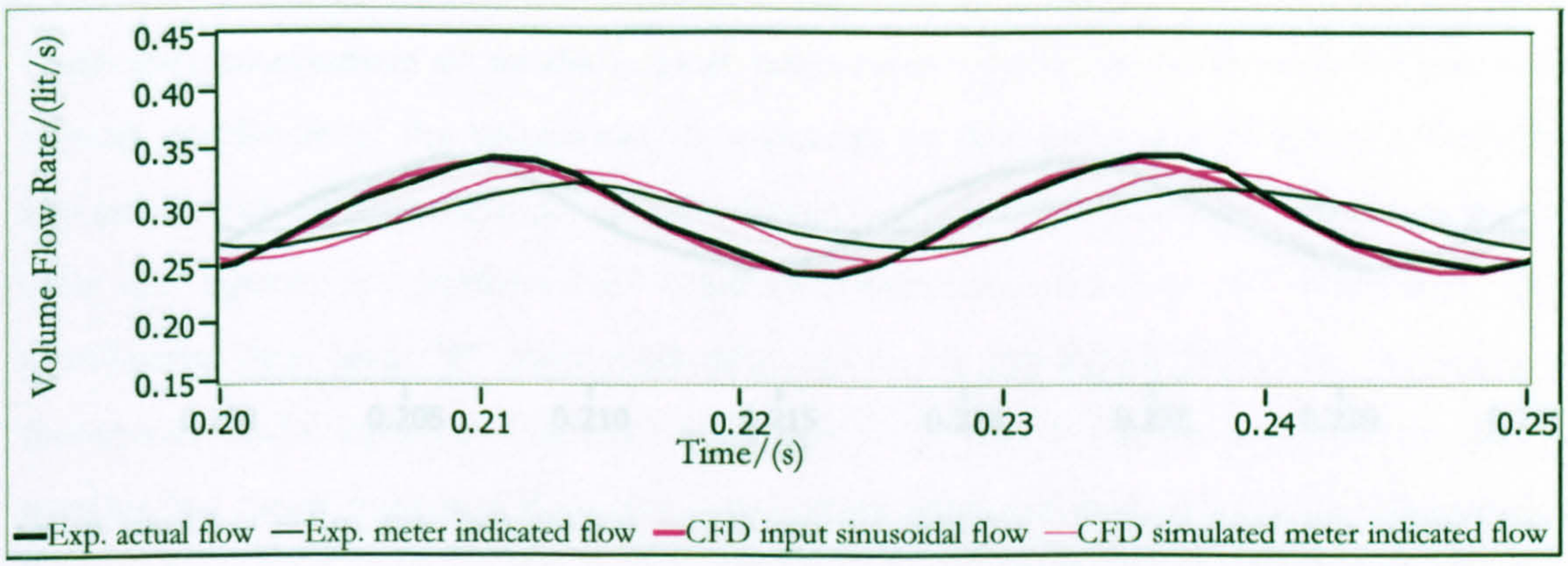

Figure 8. 19 **P4 — Comparison of actual flow, meter indicated flow, CFD simulated flow and predicted meter flow; at f_p= 40 Hz, α_p= 16.57 %.**

P5: f_p= 40 Hz, α_p= 26.16 %

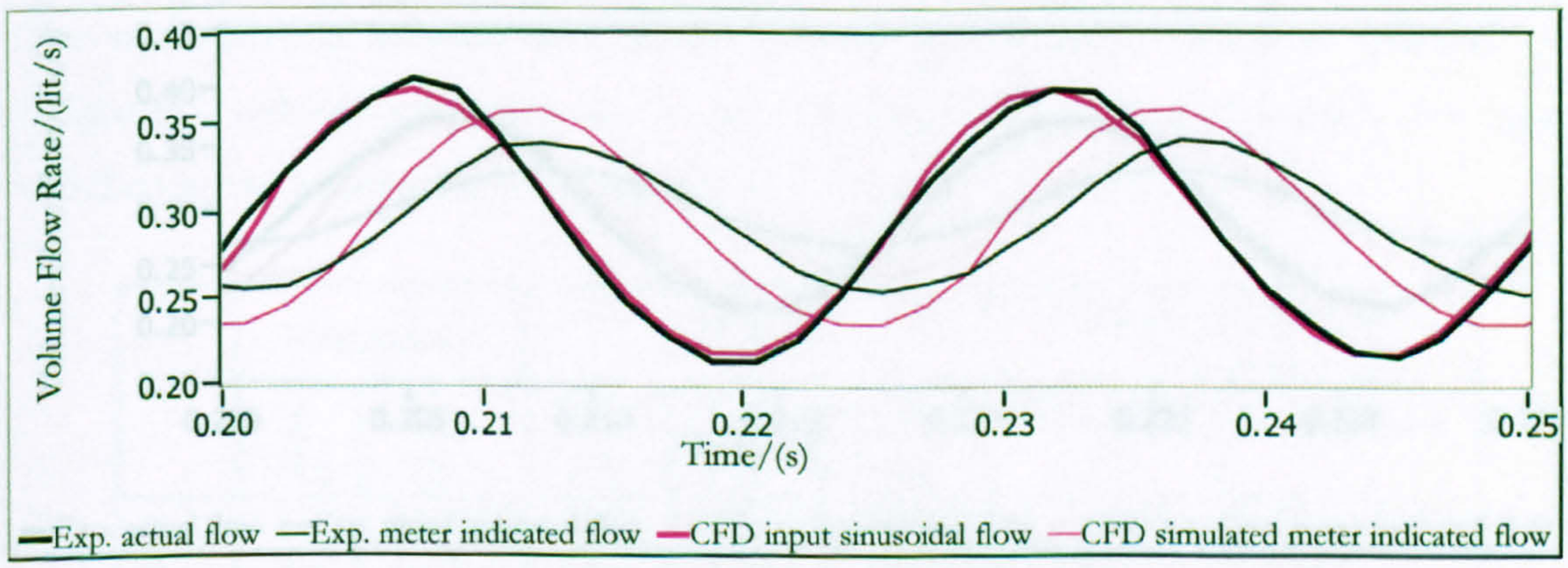

Figure 8. 20 **P5 — Comparison of actual flow, meter indicated flow, CFD simulated flow and predicted meter flow; at f_p= 40 Hz, α_p= 26.16 %.**

P6: f_p= 40 Hz, α_p= 40.63 %

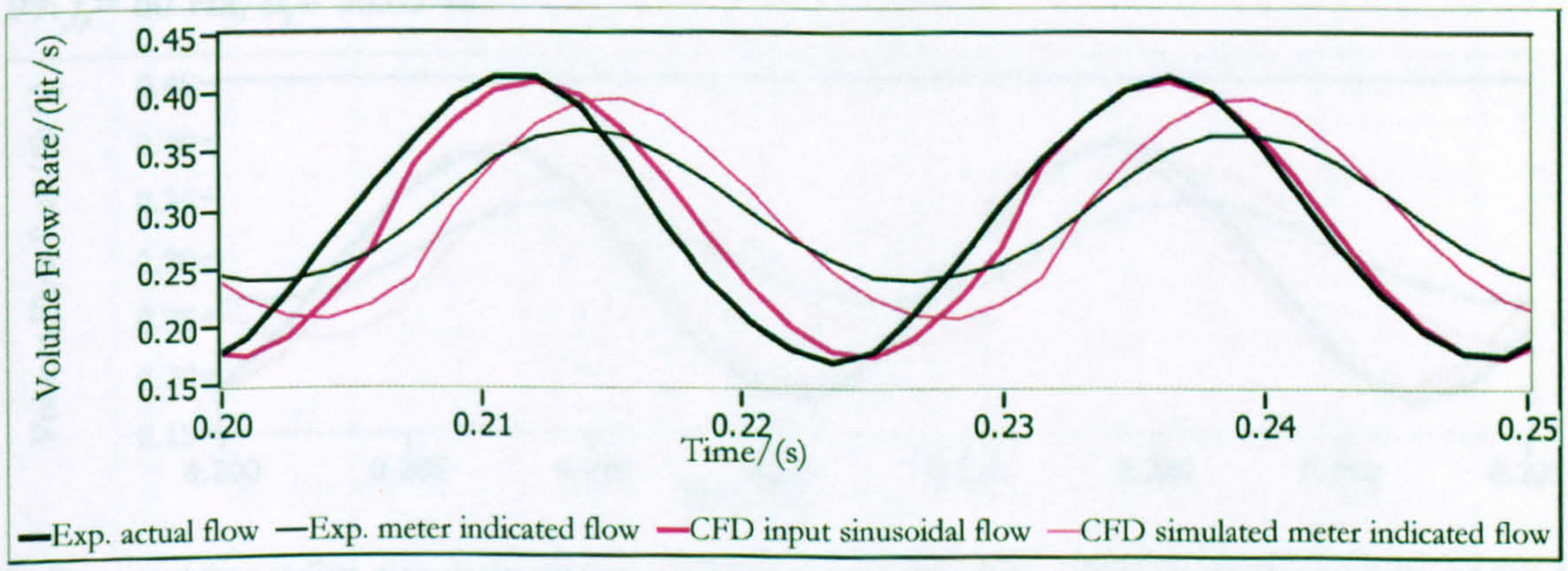

Figure 8. 21 **P6 — Comparison of actual flow, meter indicated flow, CFD simulated flow and predicted meter flow; at f_p= 40 Hz, α_p= 40.63 %.**

P7: f_p= 60 Hz, α_p= 16.65 %

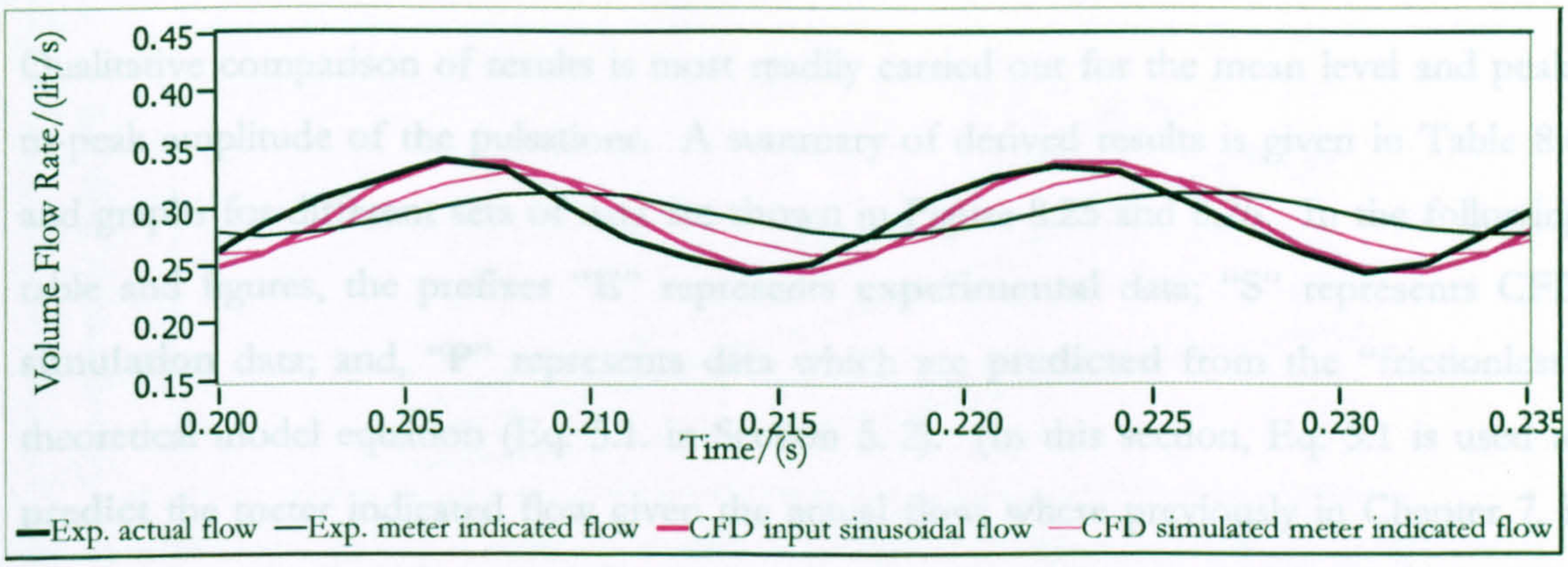

Figure 8. 22 **P7 — Comparison of actual flow, meter indicated flow, CFD simulated flow and predicted meter flow; at f_p= 60 Hz, α_p= 16.65 %.**

P8: f_p= 60 Hz, α_p= 28.13 %

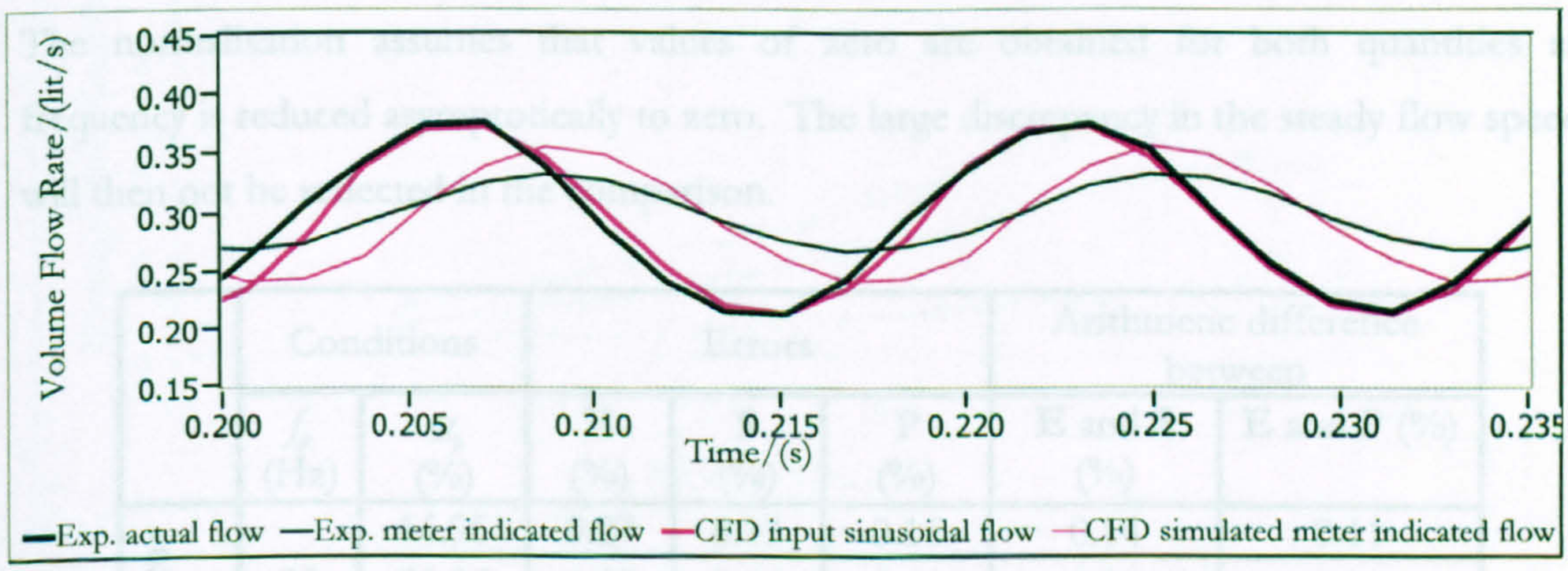

Figure 8. 23 **P8 — Comparison of actual flow, meter indicated flow, CFD simulated flow and predicted meter flow; at f_p= 60 Hz, α_p= 28.13 %.**

P9: f_p= 60 Hz, α_p= 36.69 %

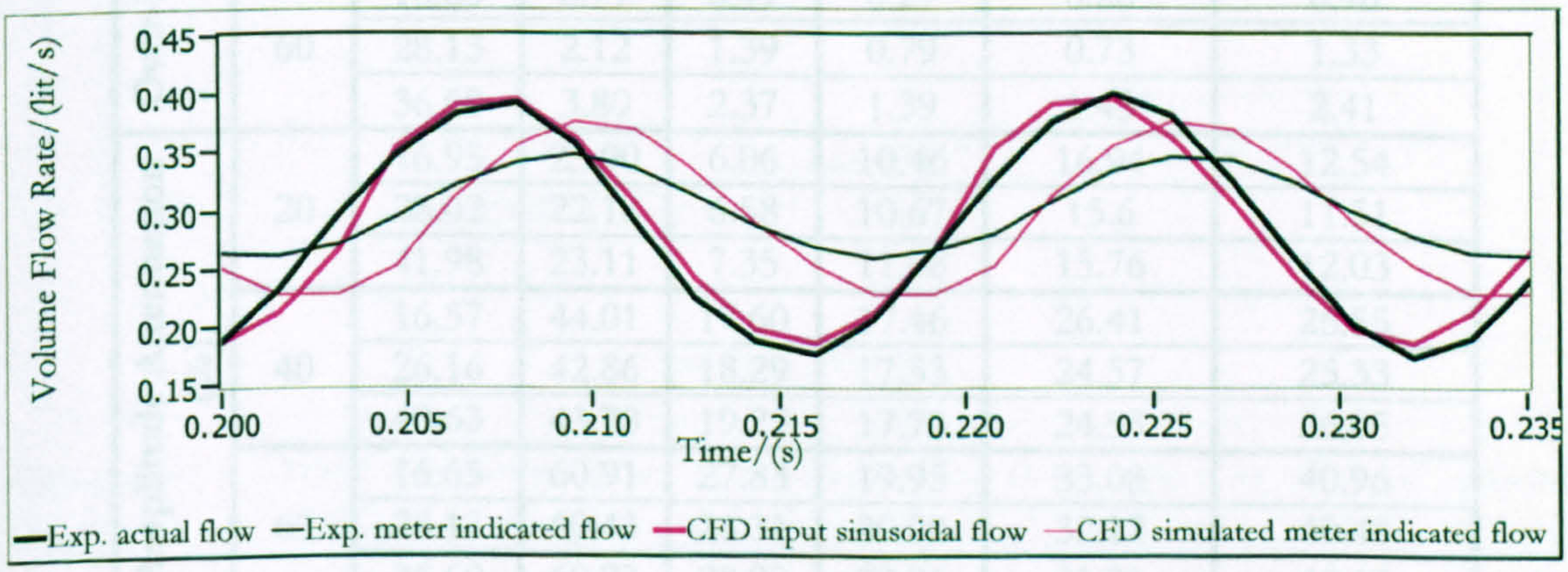

Figure 8. 24 **P9 — Comparison of actual flow, meter indicated flow, CFD simulated flow and predicted meter flow; at f_p= 60 Hz, α_p= 36.69 %.**

8.4.3 'Harmonic' analysis

Qualitative comparison of results is most readily carried out for the mean level and peak-to-peak amplitude of the pulsations. A summary of derived results is given in Table 8.6 and graphs for different sets of data are shown in Figure 8.25 and 8.26. In the following table and figures, the prefixes "**E**" represents **experimental** data; "**S**" represents CFD **simulation** data; and, "**P**" represents data which are **predicted** from the "frictionless" theoretical model equation (Eq. 5.1. in Section 5. 2). (In this section, Eq. 5.1 is used to **predict** the meter indicated flow given the actual flow; where previously in Chapter 7, it was used to simulate the actual flow using the experimental meter indicated flow. The mode of usage is, in effect, the reverse of the procedure previously used).

In this presentation of results the mean and peak-to-peak amplitude are normalised as over-registration error and amplitude attenuation factor respectively (Eqs. 2.3 and 2.4). The normalisation assumes that values of zero are obtained for both quantities as frequency is reduced asymptotically to zero. The large discrepancy in the steady flow speed will then not be reflected in the comparison.

	Conditions		Errors			Arithmetic difference between	
	f_p (Hz)	α_p (%)	**E** (%)	**S** (%)	**P** (%)	**E** and **S** (%)	**E** and **P** (%)
Over-Registration Error (%)	20	16.95	0.27	0.13	0.16	0.14	0.11
		28.02	0.68	0.36	0.44	0.32	0.24
		41.98	1.58	0.85	1.03	0.73	0.55
	40	16.57	0.53	0.32	0.26	0.21	0.27
		26.16	1.41	0.83	0.61	0.58	0.80
		40.63	3.39	2.01	1.53	1.38	1.86
	60	16.65	0.77	0.49	0.29	0.28	0.48
		28.13	2.12	1.39	0.79	0.73	1.33
		36.69	3.80	2.37	1.39	1.43	2.41
Amplitude Attenuation (%)	20	16.95	23.00	6.06	10.46	16.94	12.54
		28.02	22.18	6.58	10.67	15.6	11.51
		41.98	23.11	7.35	11.08	15.76	12.03
	40	16.57	44.01	17.60	17.46	26.41	26.55
		26.16	42.86	18.29	17.53	24.57	25.33
		40.63	43.78	19.25	17.73	24.53	26.05
	60	16.65	60.91	27.83	19.95	33.08	40.96
		28.13	60.43	28.31	20.00	32.12	40.43
		36.69	60.23	28.92	20.06	31.31	40.17

Table 8. 6 **Comparison of experimental, simulation and prediction results for pulsating frequencies of 20, 40 and 60 Hz.**

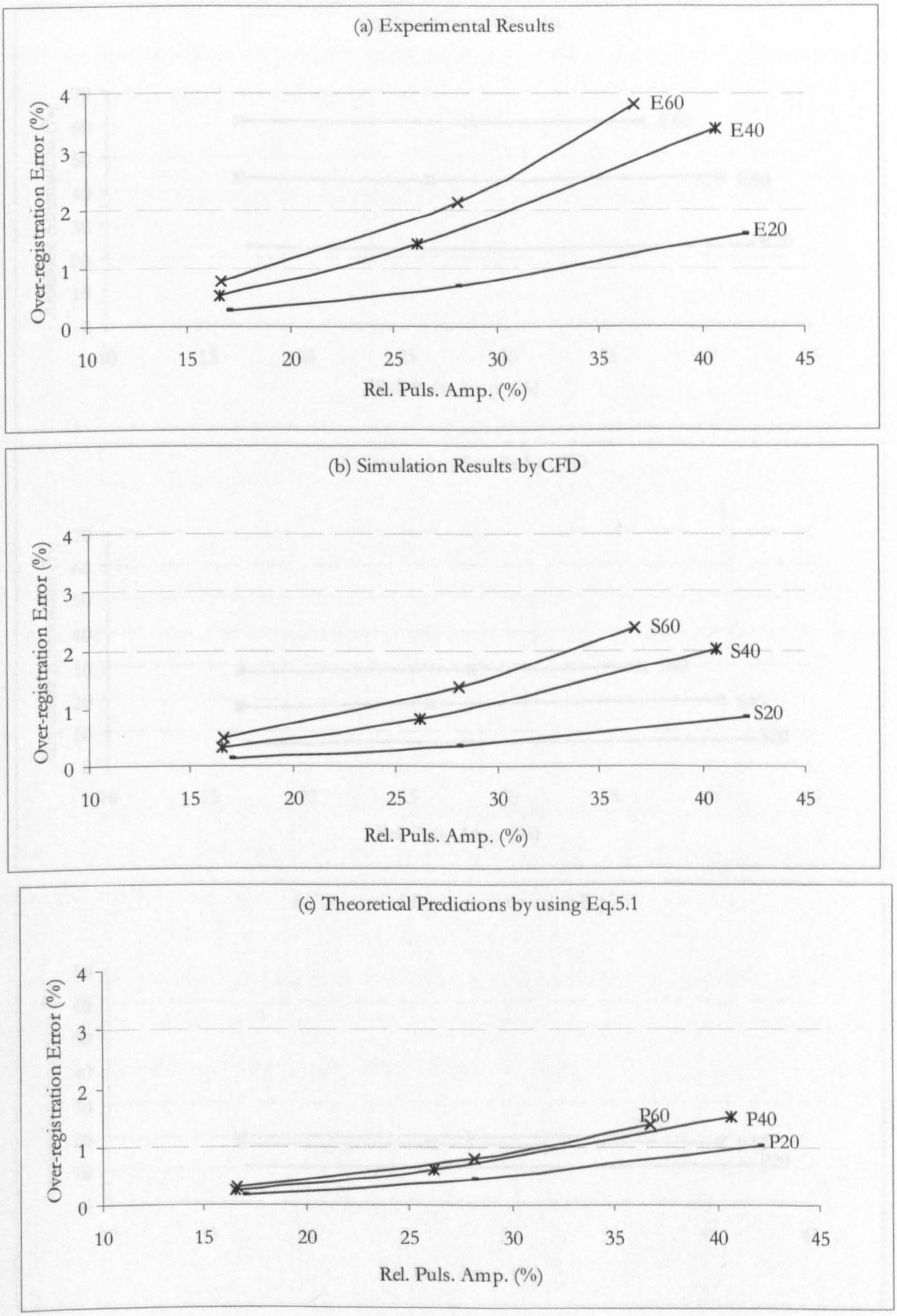

Figure 8. 25 Meter B – Comparisons of over-registration errors with a selection of pulsation amplitudes and pulsation frequencies from: (a) experimental results, (b) simulations by CFD modelling, and (c) normalised "frictionless" theoretical model predictions.

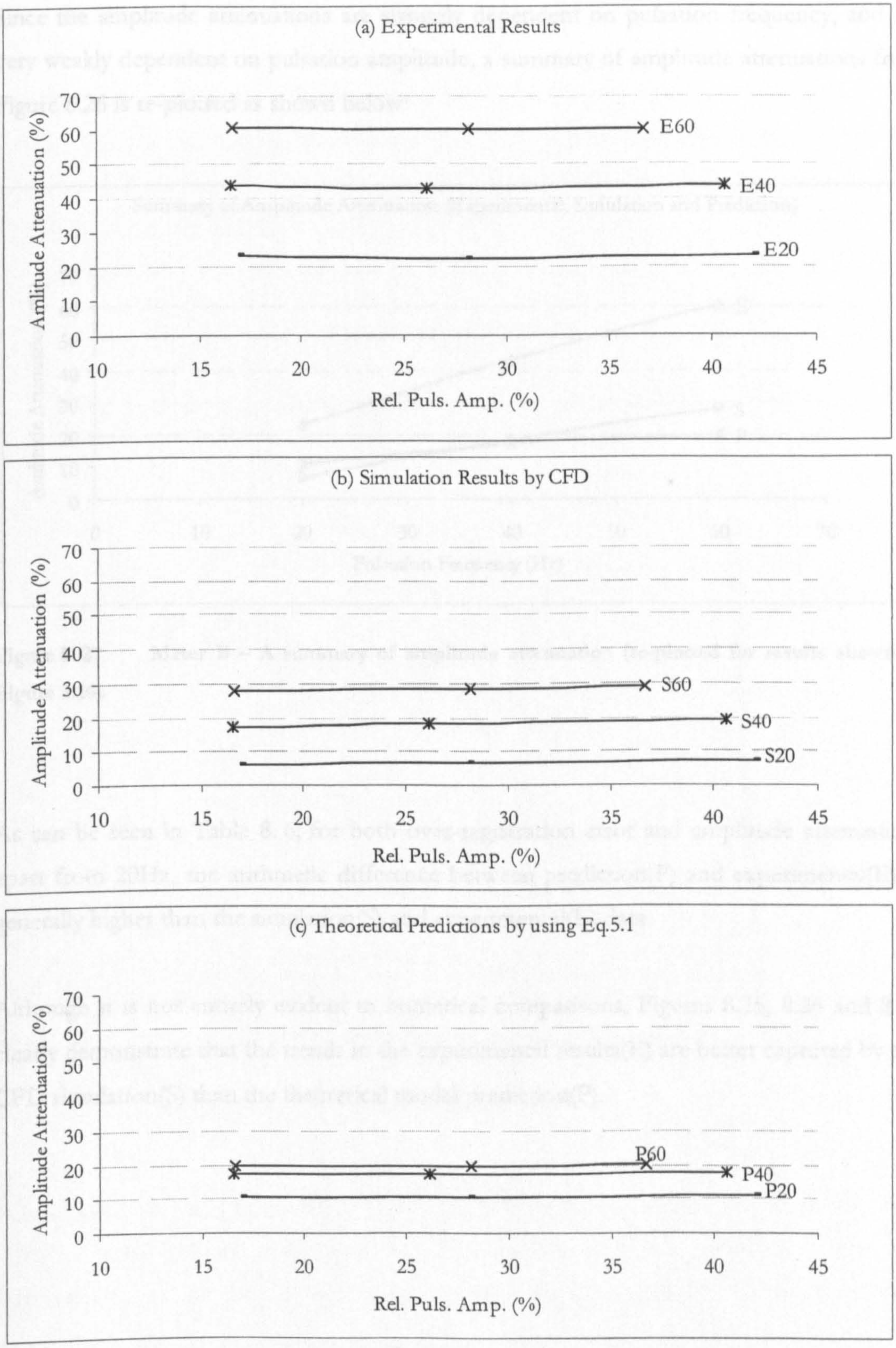

Figure 8. 26 **Meter B – Comparisons of amplitude attenuations with a selection of pulsation amplitudes and pulsation frequencies from: (a) experimental results, (b) simulations by CFD modelling, and (c) normalised "frictionless" theoretical model predictions.**

Since the amplitude attenuations are strongly dependent on pulsation frequency, and are very weakly dependent on pulsation amplitude, a summary of amplitude attenuations from Figure 8.26 is re-plotted as shown below:

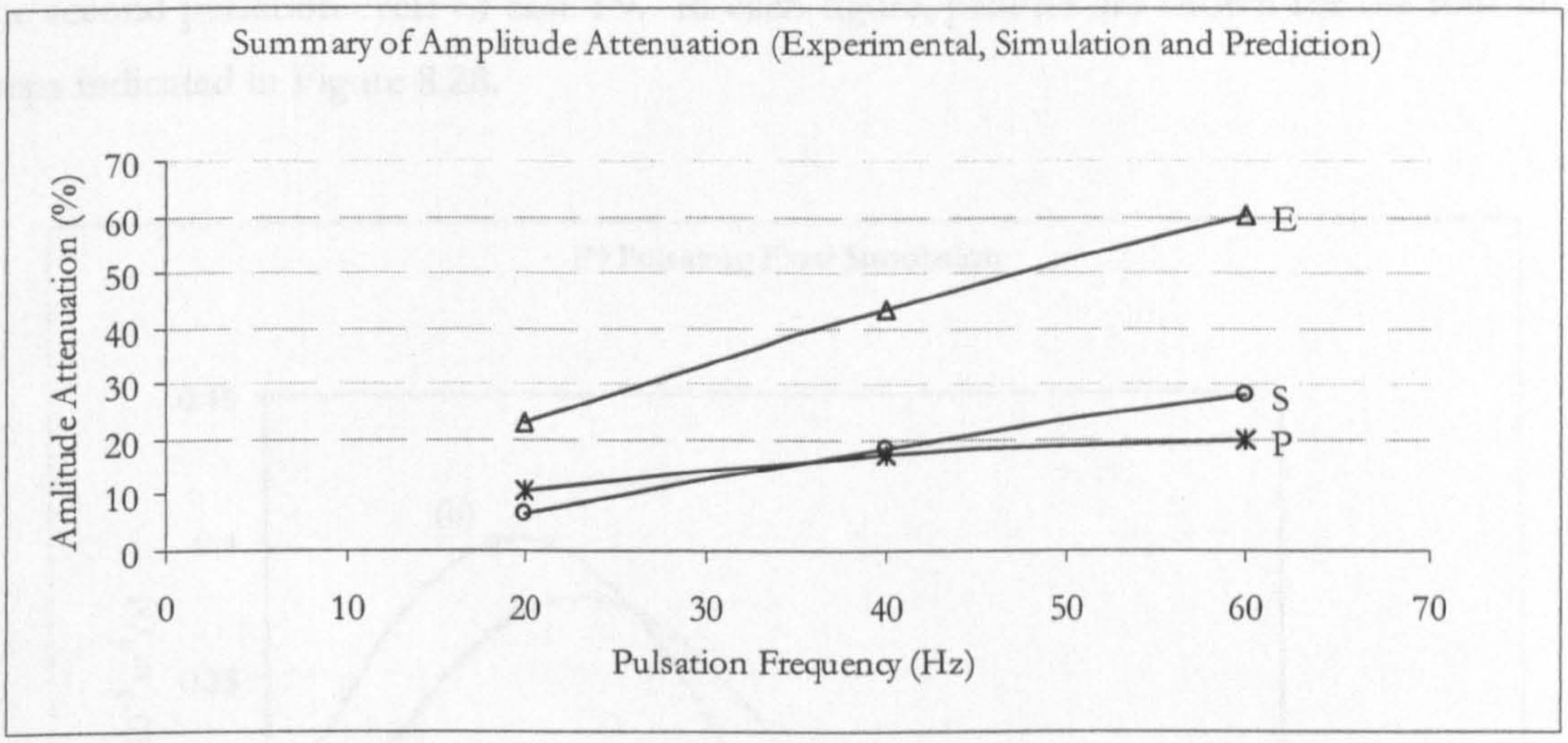

Figure 8. 27 Meter B – A summary of amplitude attenuation (re-plotted for results shown in Figure 8.26)

As can be seen in Table 8. 6; for both over-registration error and amplitude attenuation, apart from 20Hz, the arithmetic difference between prediction(P) and experimental(E) is generally higher than the simulation(S) and experimental(E) data.

Although it is not entirely evident in numerical comparisons, Figures 8.25, 8.26 and 8.27 clearly demonstrate that the trends in the experimental results(E) are better captured by the CFD simulation(S) than the theoretical model prediction(P).

8.4.4 Flow profiles

Predicted flow profiles on a blade-to-blade surface at the rms radius are examined in this section. Velocity and vorticity profiles are shown in Figures 8.29 and 8.30 respectively for the second pulsation cycle of case P9. In each figure, profiles are shown for the four time steps indicated in Figure 8.28.

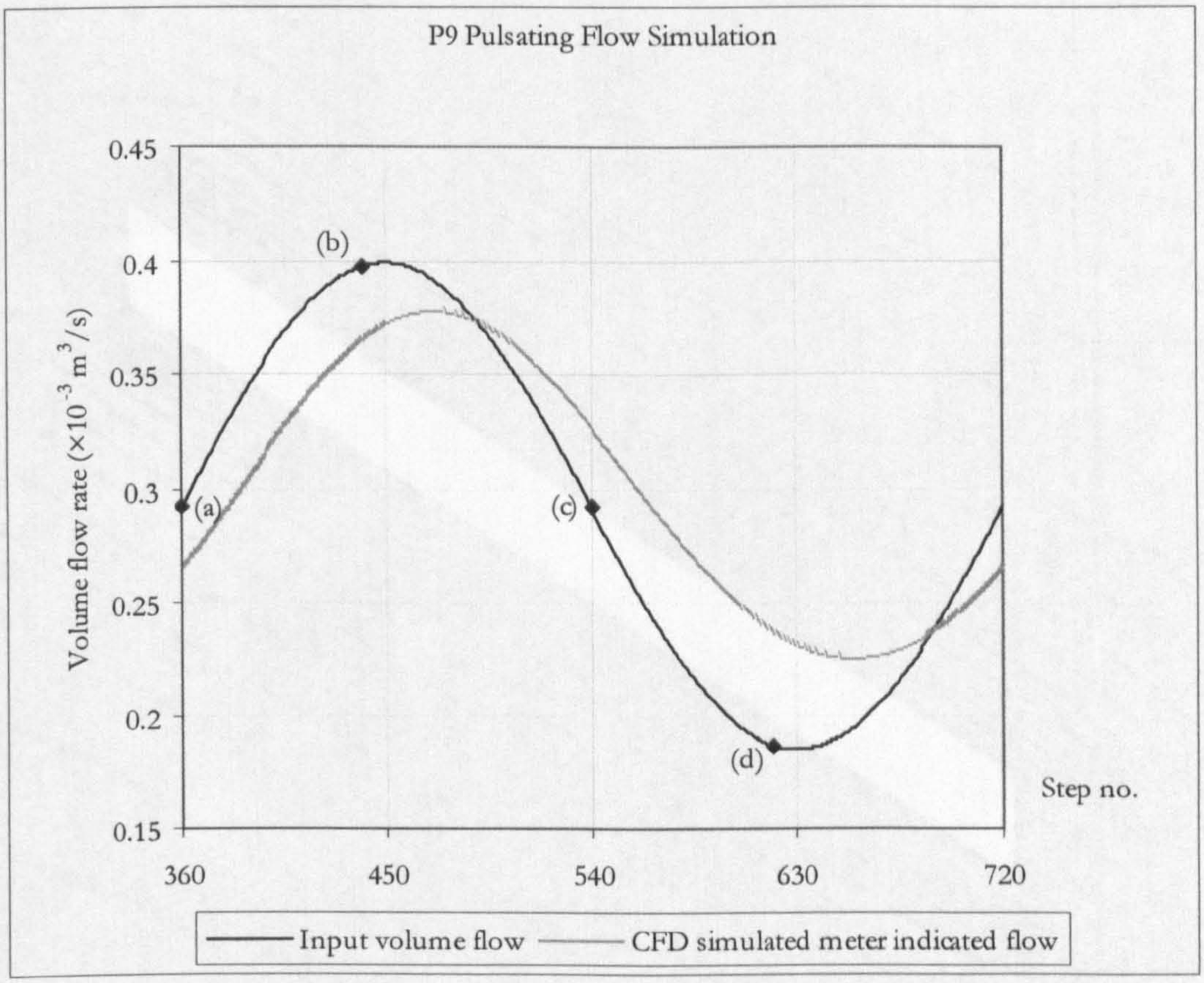

Figure 8. 28 P9 — Comparison of input volume flow and CFD simulated meter flow;

$\overline{\dot{V}_s}$ = 0.292 × 10⁻³ m³/s, f_p= 60 Hz, α_p= 36.69 %.

It would be interesting to see whether the flow behaviour at points (a) and (c) would be any different since they are both on the mean flow line crossing. Similarly it would be interesting to see whether the flow behaviour at points (b) and (d) would be any different, as point (b) represents accelerating high flow and point (d) represents decelerating low flow.

P9 Velocity Plot (Step 360)

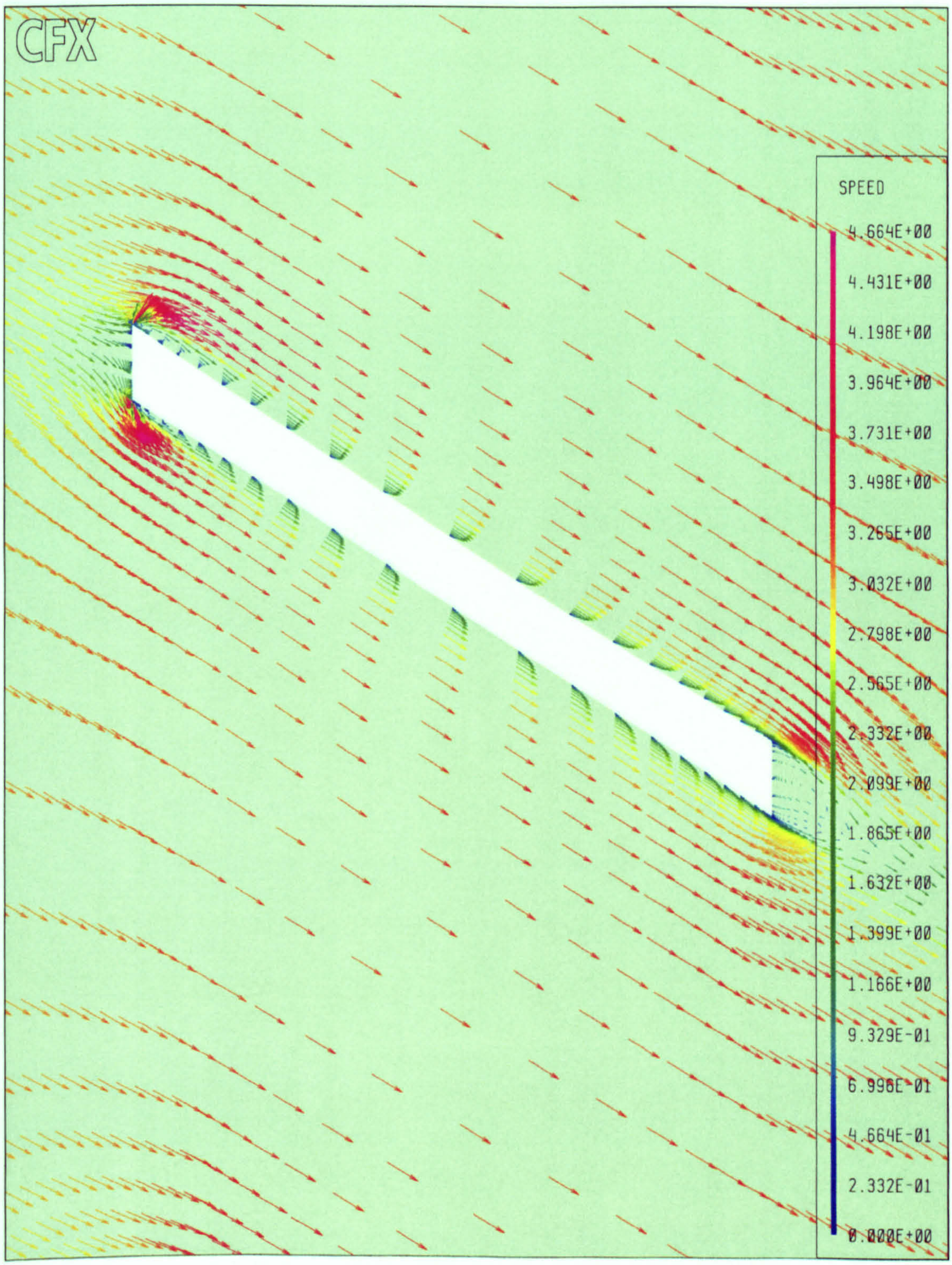

Figure 8. 29(a) **P9 (Step 360) — Velocity plotted on rms radius surface;**

$\overline{\dot{V}_s}$ = 0.292 × 10^{-3} m^3/s, f_p= 60 Hz, α_p= 36.69 %.

P9 Velocity Plot (Step 440)

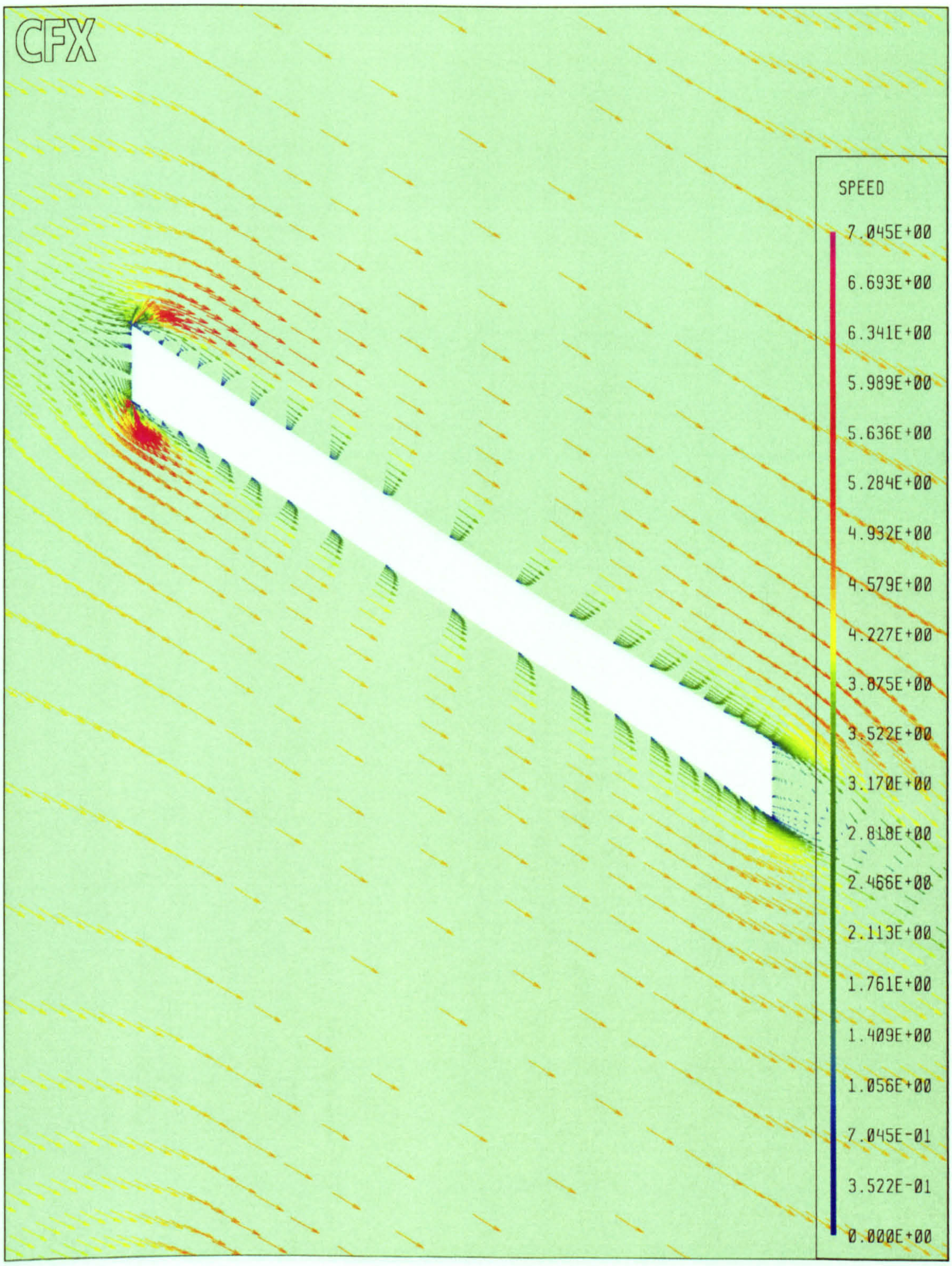

Figure 8. 29(b) P9 (Step 440) — Velocity plotted on rms radius surface;

$\overline{\dot{V}_s}$ = 0.292 × 10^{-3} m^3/s, f_p= 60 Hz, α_p= 36.69 %.

P9 Velocity Plot (Step 540)

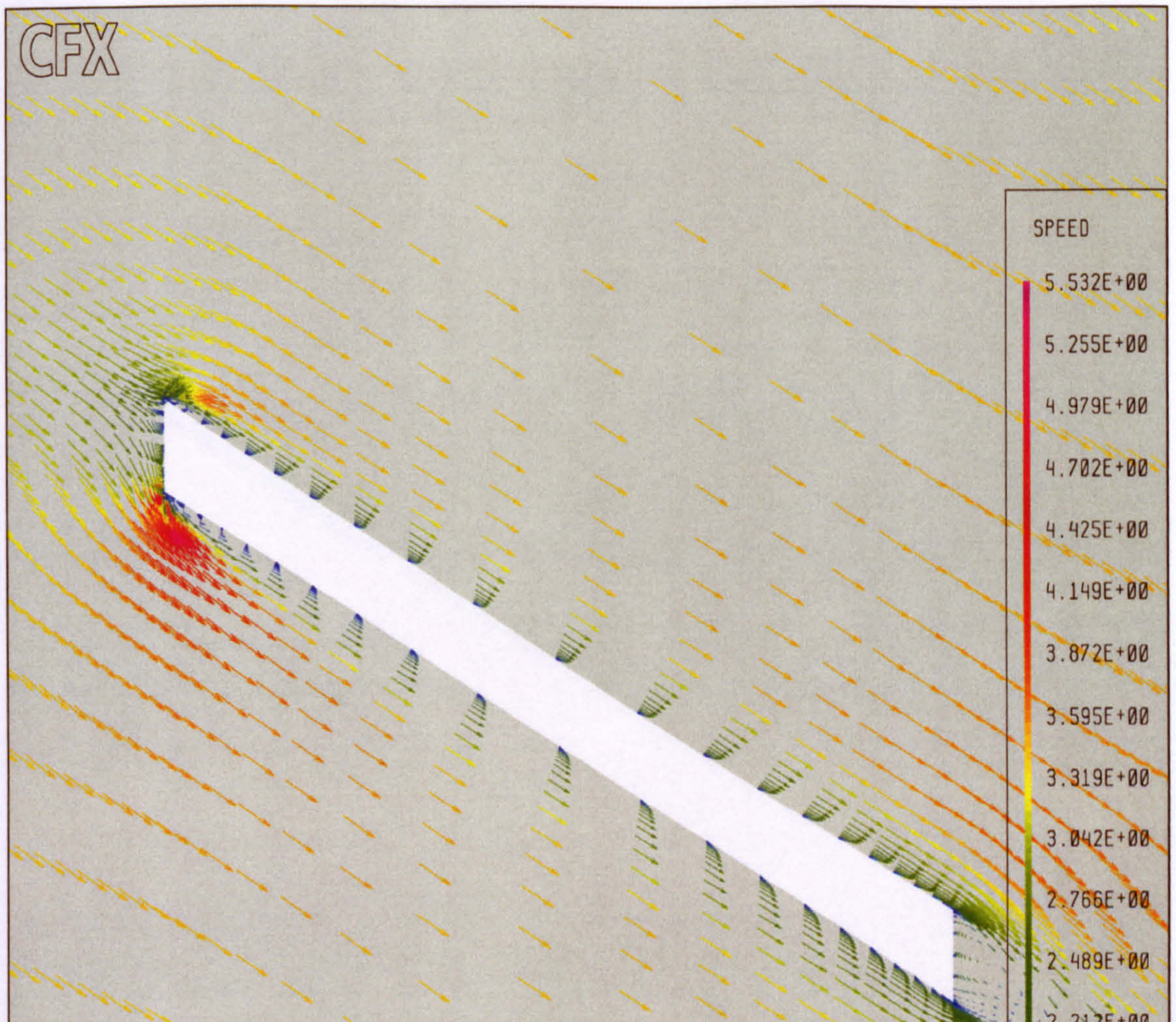

Figure 8. 29(c) P9 (Step 540) — Velocity plotted on rms radius surface;

$\overline{\dot{V}_s}$ = 0.292 × 10^{-3} m^3/s, f_p= 60 Hz, α_p= 36.69 %.

P9 Velocity Plot (Step 620)

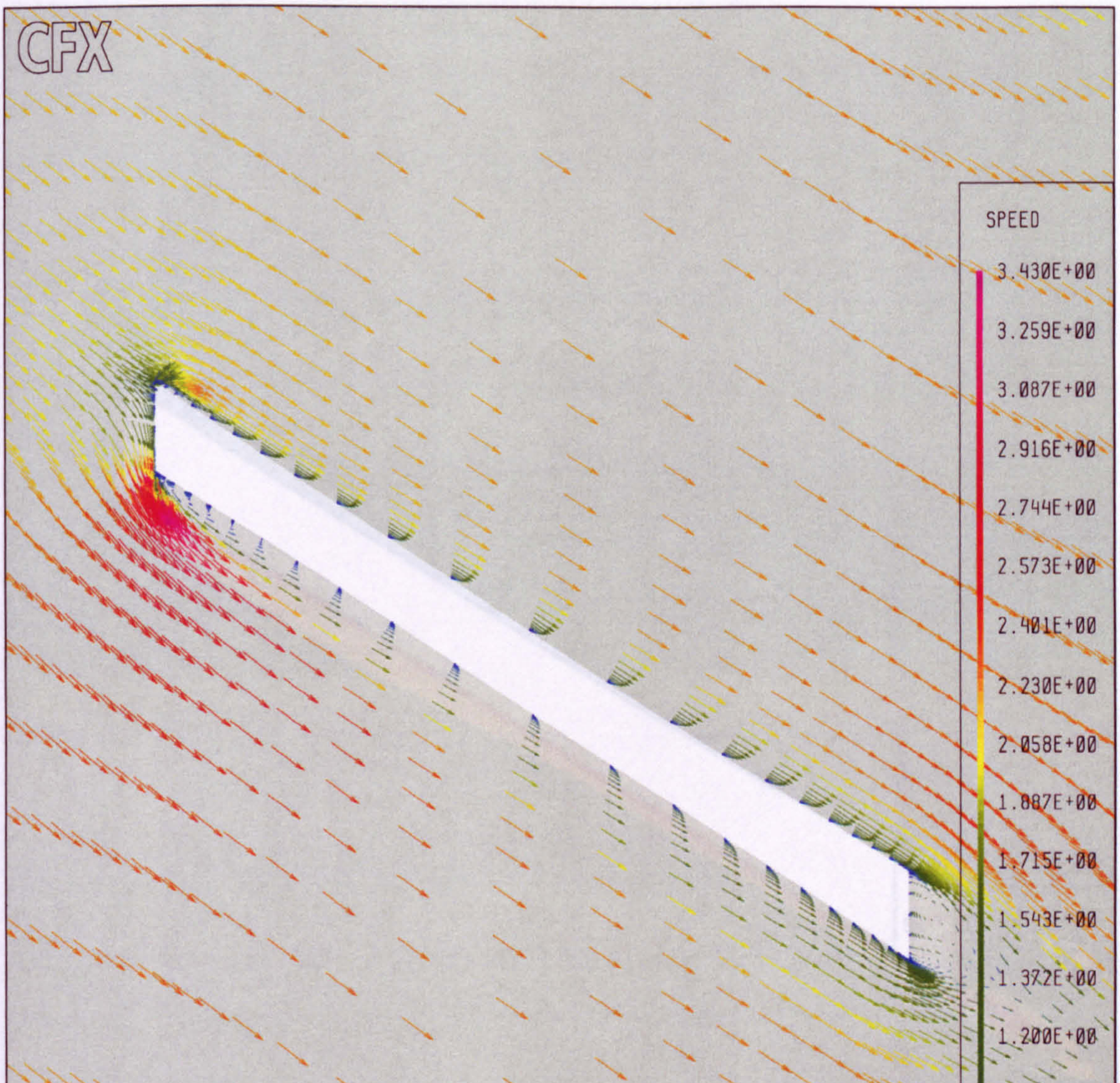

Figure 8. 29(d) P9 (Step 620) — Velocity plotted on rms radius surface;

$\overline{\dot{V}_s}$ = 0.292 × 10^{-3} m^3/s, f_p= 60 Hz, α_p= 36.69 %.

P9 Vorticity Plot (Step 360)

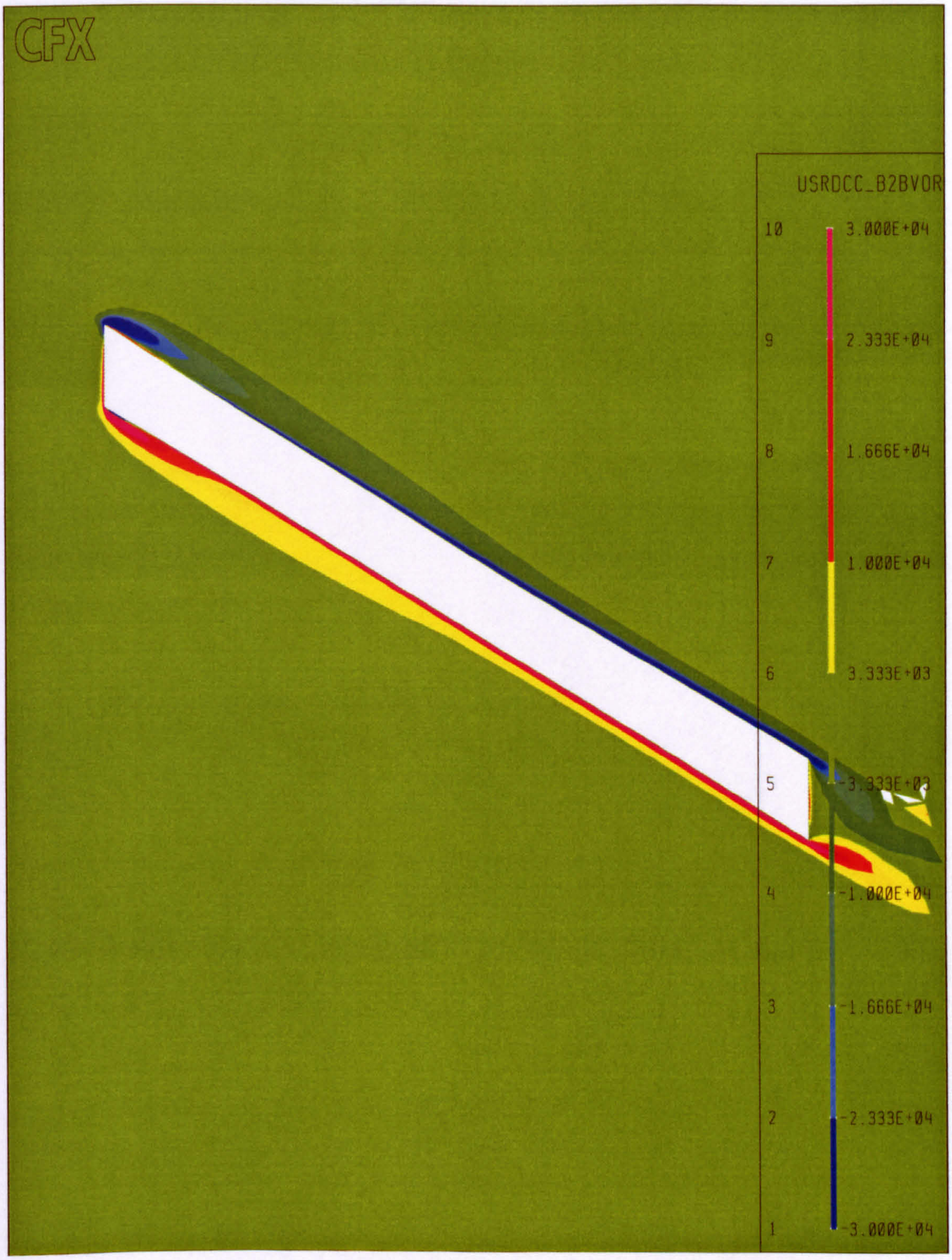

Figure 8. 30(a) P9 (Step 360) — Vorticity plotted on rms radius surface;

$\overline{\dot{V}_s}$ = 0.292 × 10^{-3} m^3/s, f_p= 60 Hz, α_p= 36.69 %.

P9 Vorticity Plot (Step 440)

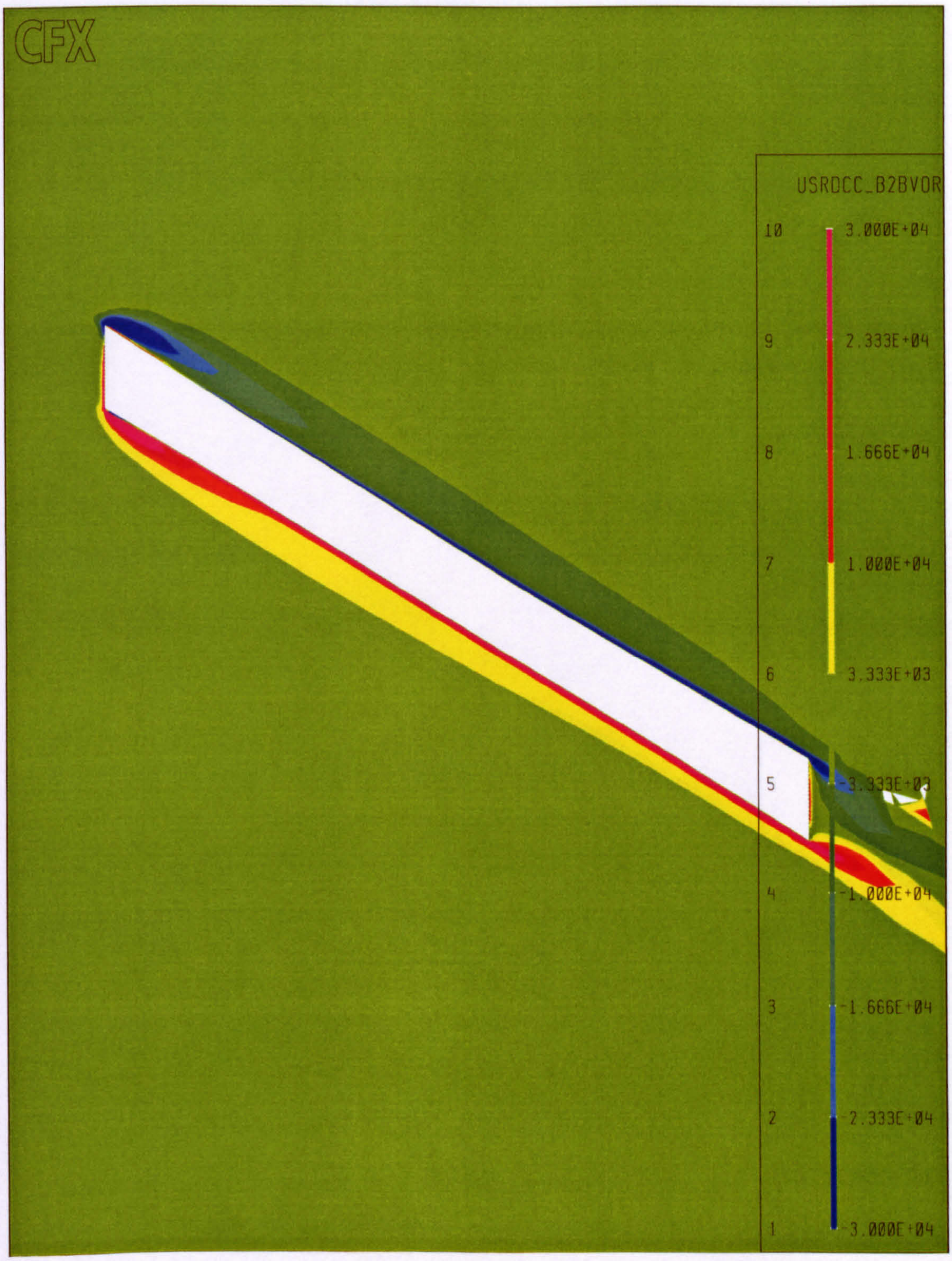

Figure 8. 30(b) P9 (Step 440) — Vorticity plotted on rms radius surface;

$\overline{\dot{V}_s}$ = 0.292 × 10^{-3} m^3/s, f_p=60 Hz, α_p= 36.69 %.

P9 Vorticity Plot(Step 540)

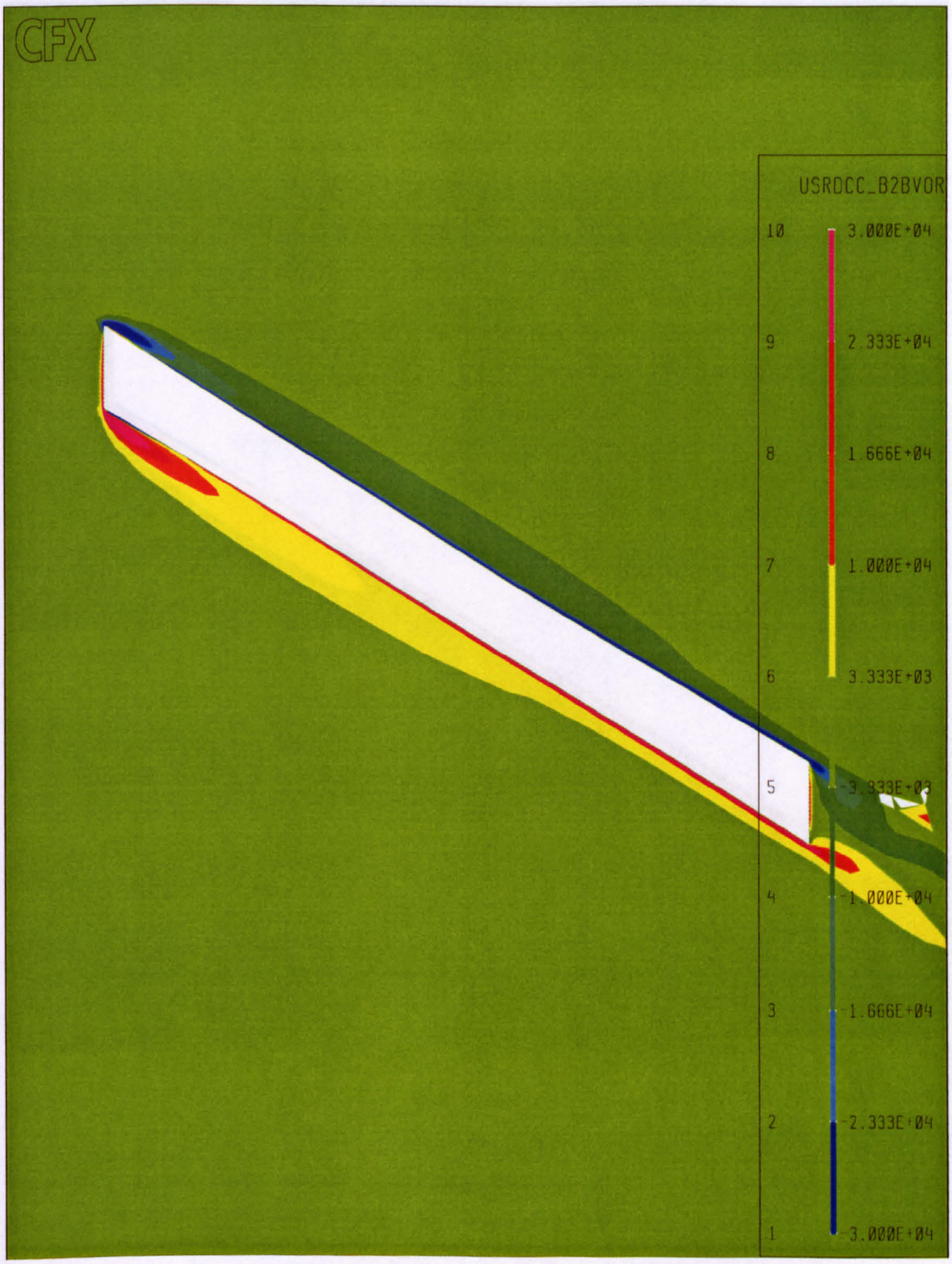

Figure 8. 30(c) P9 (Step 540) — Vorticity plotted on rms radius surface;

$\overline{\dot{V}_s}$ **= 0.292 × 10^{-3} m^3/s, f_p=60 Hz, α_p= 36.69 %.**

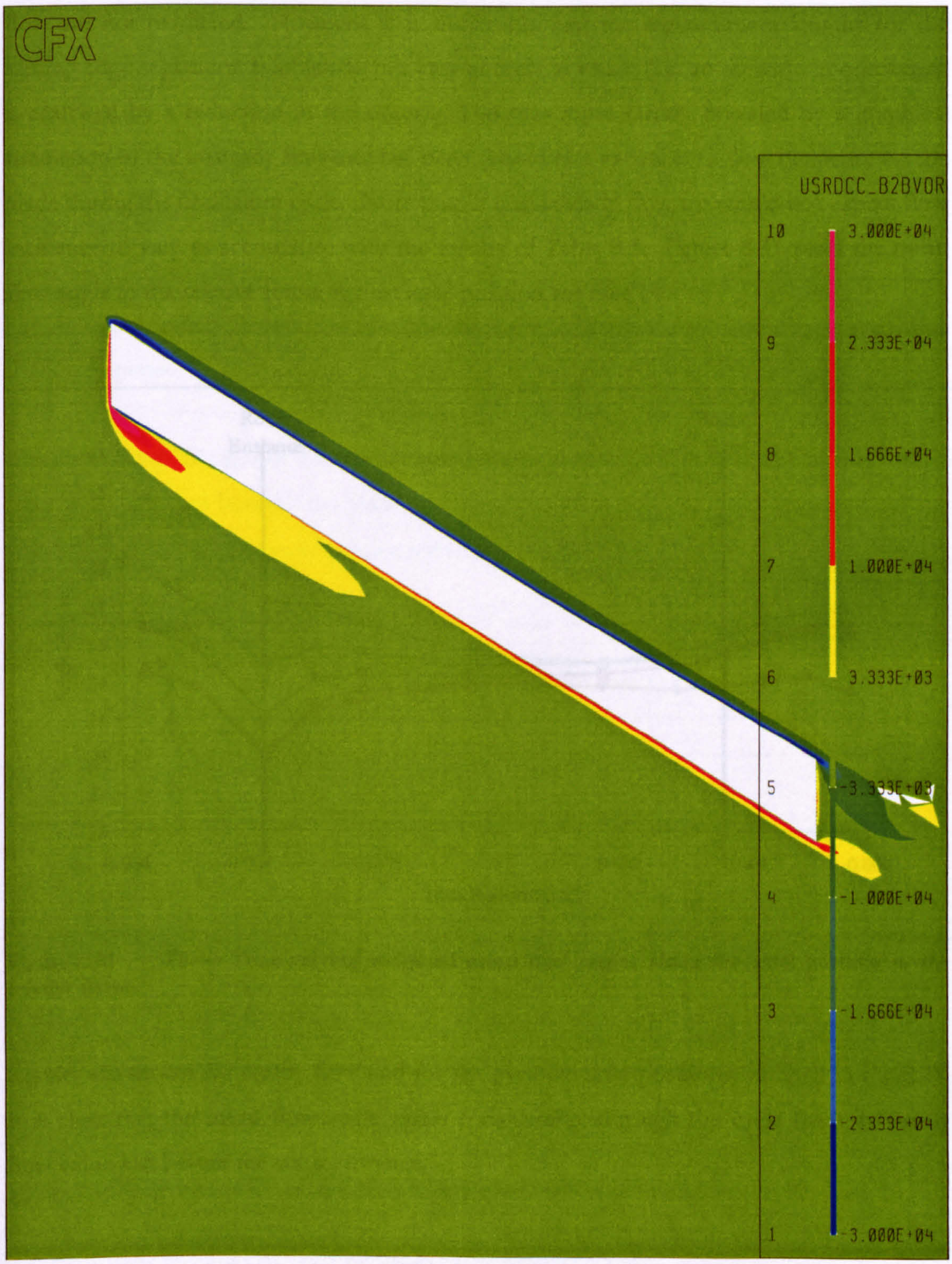

Figure 8. 30(d) P9 (Step 620) — Vorticity plotted on rms radius surface;

$\overline{\dot{V}_s}$ = 0.292 × 10^{-3} m^3/s, f_p=60 Hz, α_p= 36.69 %.

Clearly, the overall structure of the flow is not grossly different from the steady flow structure (Figures 8.11 and 8.12). Particularly in the respect that large areas of separated flow are not predicted. However, it is noticeable that the reattachment lengths for the leading edge separation bubbles do not vary entirely in phase (i.e. an increase in one length is matched by a reduction in the other). This was more clearly revealed by a graphical simulation of the unsteady flow and has been related to a variation in flow incidence on the blade during the oscillation cycle. Note that in quasi-steady flow we would not expect flow incidence to vary in accordance with the results of Table 8.3. Figure 8.31 plots the mean flow angle in the relative frame against axial position for case P9.

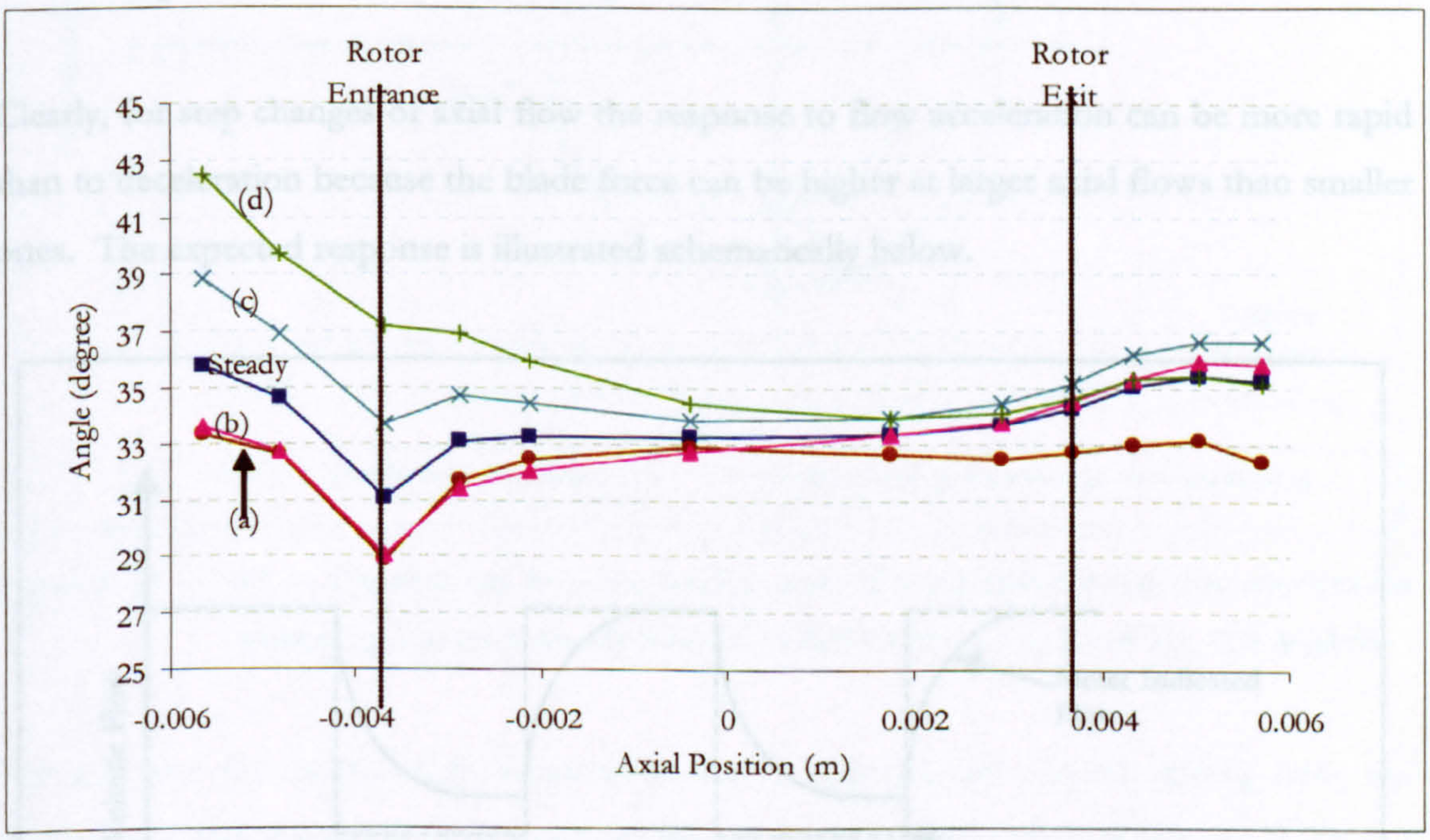

Figure 8. 31 P9 — Time varying weighted mean flow angles along the axial position in the relative frame

Results are shown for steady flow and for the periodic time positions outlined in Fig.8.28. It is clear that the mean flow angle varies considerably through the cycle from its steady flow value just before the rotor entrance.

8.4.5 Analysis and discussion

It is possible to explain the basic trends in flowmeter response with reference to the response to a square wave variation of axial flow. As the acceleration of the blade is ultimately limited by the change in angular momentum through the rotor we can say that:

i. The blade force and acceleration are dependent on the axial flow rate. At high axial flows a faster response is possible than at low axial flows.

ii. At sufficiently high frequencies, the blade response lags the axial flow because the blade force is insufficient to provide the acceleration required for a more rapid response.

Clearly, for step changes of axial flow the response to flow acceleration can be more rapid than to deceleration because the blade force can be higher at larger axial flows than smaller ones. The expected response is illustrated schematically below.

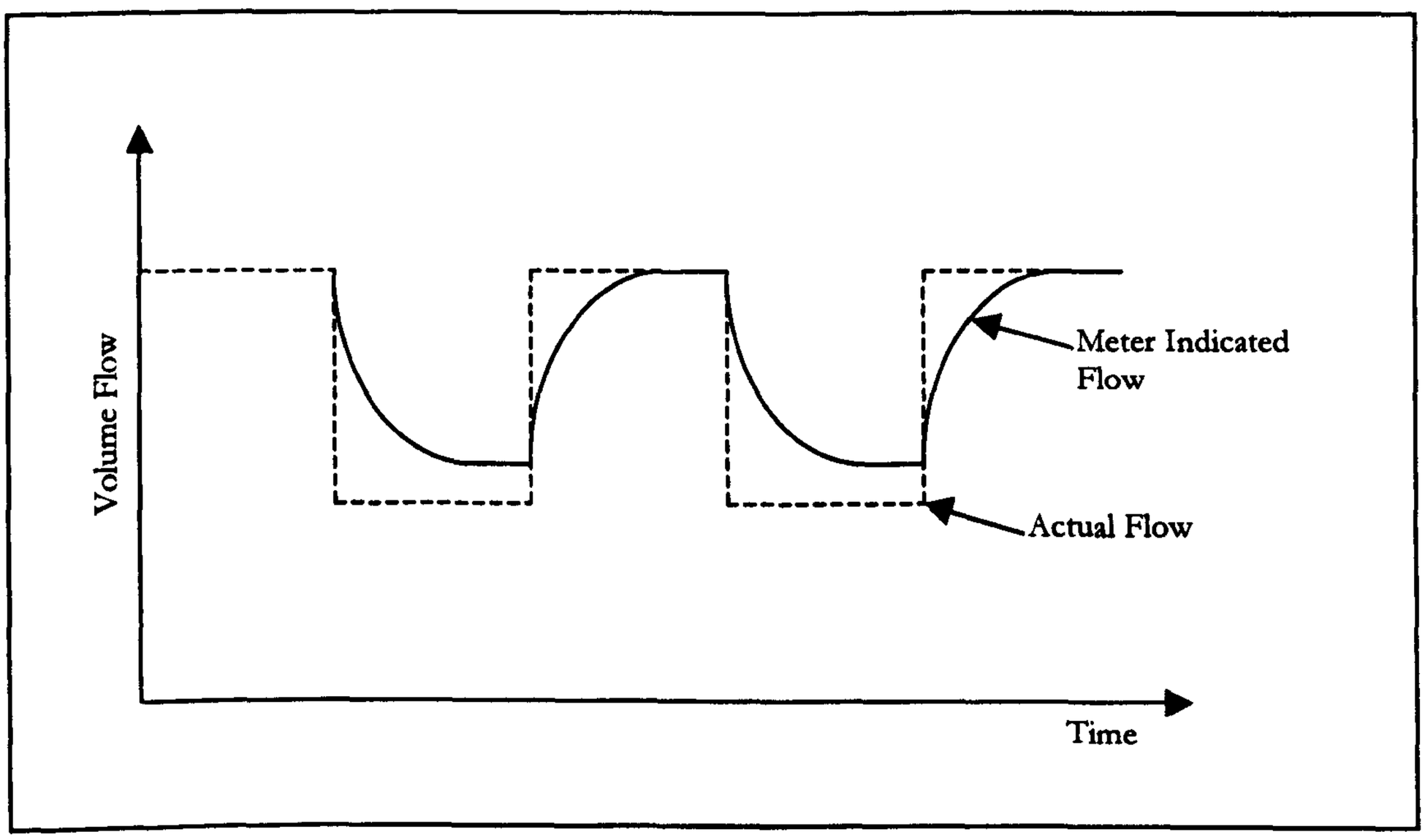

Figure 8. 32 Schematic Diagram of meter response to step flow

It is evident that the first harmonic of the measured flow inferred from the blade pulsation will have a reduced amplitude, a raised mean and a phase lag relative to the actual flow. This is exactly what is observed in sinusoidally oscillated flow. Most notably, it is suggested

that the response to flow acceleration should be different from the response to deceleration. We can examine this point for the conditions of case P9: Figure 8.33 shows the flow acceleration for this case plotted against volume flow. A closed curve is obtained for sinusoidal oscillation. The figure compares the computed result with what would have been obtained if the rotor had responded in a quasi-steady fashion.

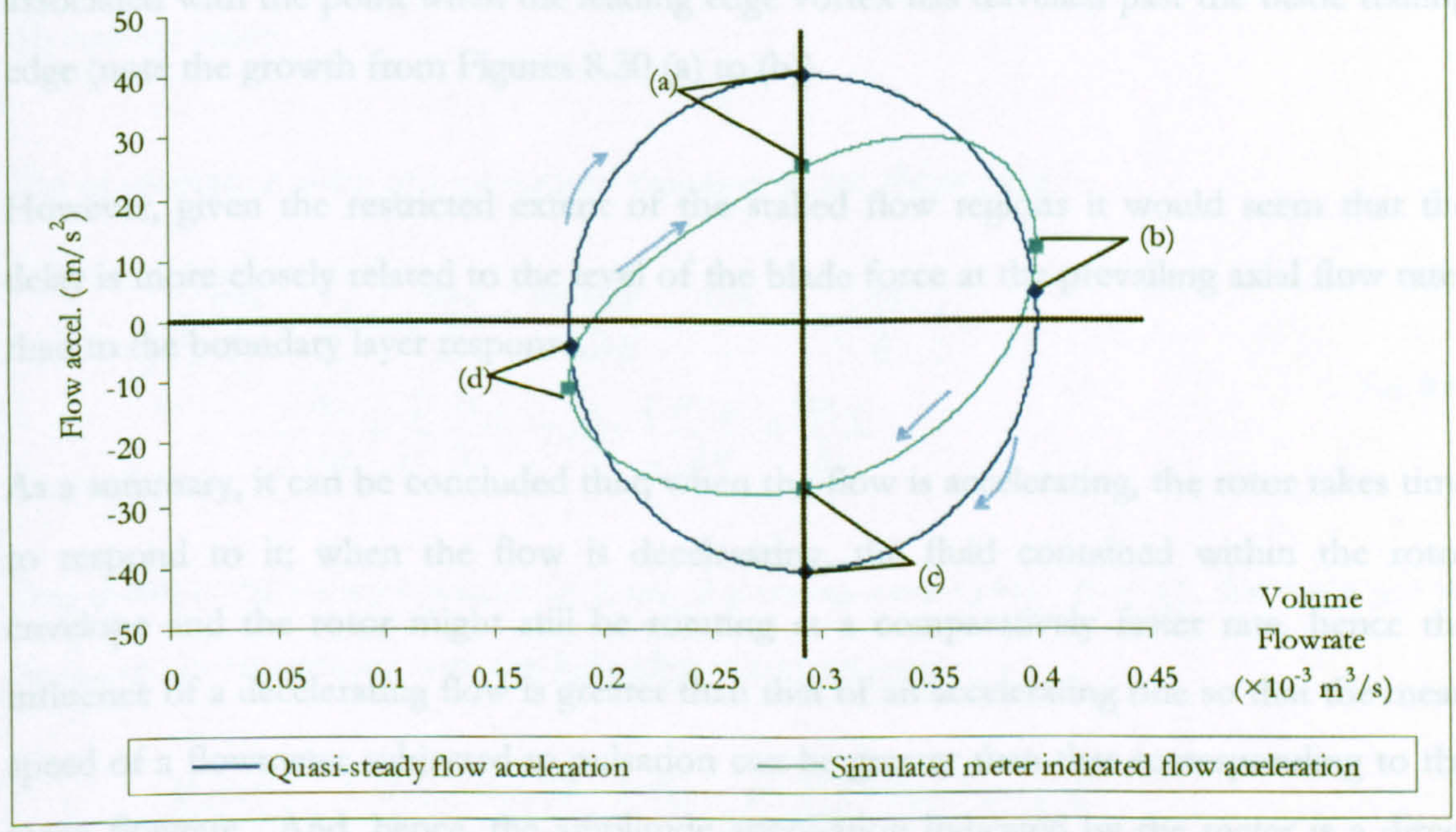

Figure 8. 33 **P9 — Quasi-steady flow acceleration and CFD simulated meter flow acceleration plotted against quasi-steady flow; $\overline{\dot{V}_s} = 0.292 \times 10^{-3}$ m^3/s, f_p= 60 Hz, α_p= 36.69 %.**

We see that the quasi-steady acceleration has a symmetrical pattern during both the acceleration and deceleration of the flow within the pulsating cycle. However, there is a significantly different pattern in the computed blade acceleration. In fact, this asymmetrical pattern in the meter indicated flow bears the same characteristics of a hysteresis loop in the dynamic stall theory (Theodorsen 1935) — "the effect of flow oscillation is to produce a time lag between the actual conditions and the state of the boundary layer. As a result, the lift (and the other forces) would be in delay."

Starting clockwise from the point of zero acceleration, just shortly after point (d), the meter flow acceleration follows the quasi-steady acceleration slowly, until at point (a) the flow acceleration starts to decrease, but the meter acceleration keeps on increasing until a breakdown occurs just before point (b). At the breakdown point there is flow separation

and hence the meter acceleration started to decrease following the quasi-steady flow deceleration. It will take some time to recover the regular behaviour, but the meter deceleration will be less than the quasi-steady deceleration for most of the remaining loop.

The increase of the meter acceleration after point (a) whilst the quasi-steady acceleration is starting to decrease is attributed to the development of a leading edge vortex on the upper surface that grows and travels downstream. The breakdown point just before point (b) is associated with the point when the leading edge vortex has travelled past the blade trailing edge (note the growth from Figures 8.30 (a) to (b)).

However, given the restricted extent of the stalled flow regions it would seem that the delay is more closely related to the level of the blade force at the prevailing axial flow rates than to the boundary layer response.

As a summary, it can be concluded that; when the flow is accelerating, the rotor takes time to respond to it; when the flow is decelerating, the fluid contained within the rotor envelope and the rotor might still be rotating at a comparatively faster rate, hence the influence of a decelerating flow is greater than that of an accelerating one so that the mean speed of a flowmeter subjected to pulsation can be greater than that corresponding to the mean flowrate. And, hence, the amplitude attenuation indicated by the meter is a direct consequence from this lagging response.

8.5 Assessment of the Dijstelbergen Model

8.5.1 Meter B

An analysis of an equation for conservation of angular momentum through the rotor, in the absolute reference frame, is given in this sub-section in order to provide an explanation of the differences between the CFD simulation and Dijstelbergen model as implemented in the current study.

The conservation form of momentum equation in the θ direction is:

$$\rho\left(\frac{\partial u_\theta}{\partial t}+\frac{1}{r}[ru_r]\frac{\partial u_\theta}{\partial r}+\frac{u_\theta}{r}\frac{\partial u_\theta}{\partial \theta}+\frac{u_r u_\theta}{r}+u_x\frac{\partial u_\theta}{\partial x}\right)= -\frac{1}{r}\frac{\partial p}{\partial \theta}+\frac{1}{r^2}\frac{\partial}{\partial r}[r^2\tau_{r\theta}]+\frac{1}{r}\frac{\partial \tau_{\theta\theta}}{\partial \theta}+\frac{\partial \tau_{x\theta}}{\partial x} \qquad \textbf{Eq. 8.17}$$

And multiply the above equation by r, angular momentum ($\rho r u_\theta$) through the rotor will be conserved in accordance with the following transport equation:

$$\frac{\partial(\rho r u_\theta)}{\partial t}+\frac{1}{r}\frac{\partial[ru_r(\rho r u_\theta)]}{\partial r}+\frac{1}{r}\frac{\partial[u_\theta(\rho r u_\theta)]}{\partial \theta}+\frac{\partial[u_x(\rho r u_\theta)]}{\partial x}= -\frac{1}{r}\frac{\partial(rp)}{\partial \theta}+\frac{1}{r}\frac{\partial}{\partial r}[r(r\tau_{r\theta})]+\frac{1}{r}\frac{\partial(r\tau_{\theta\theta})}{\partial \theta}+\frac{\partial(r\tau_{x\theta})}{\partial x} \qquad \textbf{Eq. 8.18}$$

Integrating over the domain of the rotor envelop (by application of Guass' divergence theorem) then gives the equation in vector format as follows:

$$\underbrace{\frac{d}{dt}\iiint \rho r u_\theta \, dvol}_{\text{fluid inertia}}+\underbrace{\oiint \rho r u_\theta \boldsymbol{U}\cdot d\boldsymbol{A}}_{\text{momentum flux}}=\underbrace{\oiint r[\tau_{r\theta}\boldsymbol{i}_r+(\tau_{\theta\theta}-p)\boldsymbol{i}_\theta+\tau_{x\theta}\boldsymbol{i}_x]\cdot d\boldsymbol{A}}_{\text{surface forces}} \qquad \textbf{Eq. 8.19}$$

The Dijstelbergen model, embodied in Eq. 4.14, was derived if it is assumed that:

1. The fluid within the rotor envelop rotates as a solid body.
2. The fluid enters the rotor with uniform velocity at zero angle in the absolute frame, and it emerges from the rotor within uniform velocity at the blade angle.

The correspondence between terms in Eq. 4.14 and Eq. 8.19 is then as follows:

1. Fluid Inertia Term

$$\underbrace{\frac{d}{dt}\iiint \rho r u_\theta \, dvol}_{1S} \equiv \underbrace{I_f \frac{d(U_x \tan\beta_{\bar{r}} / \bar{r} - \omega)}{dt}}_{1P}$$

2. Momentum Flux Term

$$\underbrace{\oiint \rho r u_\theta \boldsymbol{U} \cdot \boldsymbol{dA}}_{2S} \equiv \underbrace{\rho U_x A \bar{r}(U_x \tan\beta_{\bar{r}} - \omega \bar{r})}_{2P}$$

3. Surface Force Term

$$\underbrace{\oiint r[\tau_{r\theta} \boldsymbol{i}_r + (\tau_{\theta\theta} - p)\boldsymbol{i}_\theta + \tau_{x\theta} \boldsymbol{i}_x] \cdot \boldsymbol{dA}}_{3S} \equiv \underbrace{I_R \frac{d\omega}{dt}}_{3P}$$

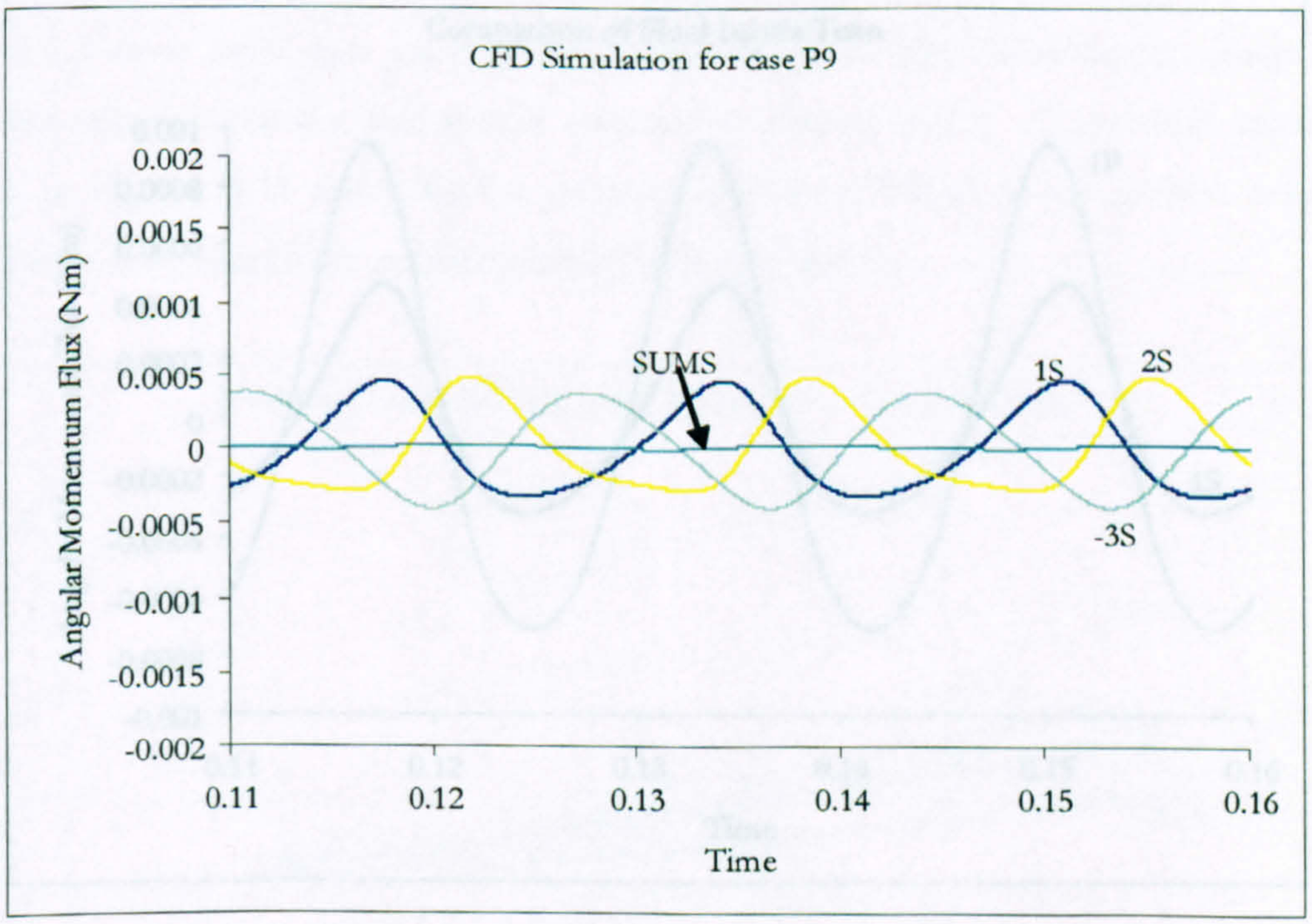

Figure 8. 34 **P9 (f_p=60 Hz, α_p=36.69%) – Comparisons of various angular momentum flux terms resulted from CFD modelling.**

Figure 8.34 plots the variation of terms in Eq. 8.19 (labelled 1S, 2S and 3S) over a flow cycle for case P9. Differences between the CFD based and Dijstelbergen models are expected to depend on the extent to which the modelled forms of fluid inertia and momentum flux terms are good models. This is tested by using the simulated variation of axial flow and blade speed to compute terms according to the Dijstelbergen model and directly comparing with the "exact" terms given by integrating CFD data. The comparisons for the fluid inertia and momentum flux terms are shown in Figures 8.35 and 8.36. We conclude that whilst the term related to the momentum flux into the rotor envelop is fairly well modelled, the inertia term is not. In fact, its amplitude is more than double of that predicted by the simulation (2.5 times). In hindsight, this is not wholly surprising as it seems unrealistic to assume that all fluid within the rotor envelope with the blades is "solid" when it certainly is not. Indeed, it might be more reasonable to expect that the fluid entering the rotor gradually adjusts itself to the prevailing blade speed as it moves axially through the meter. In this circumstance, an over-prediction of fluid inertia would result from the previous assumption.

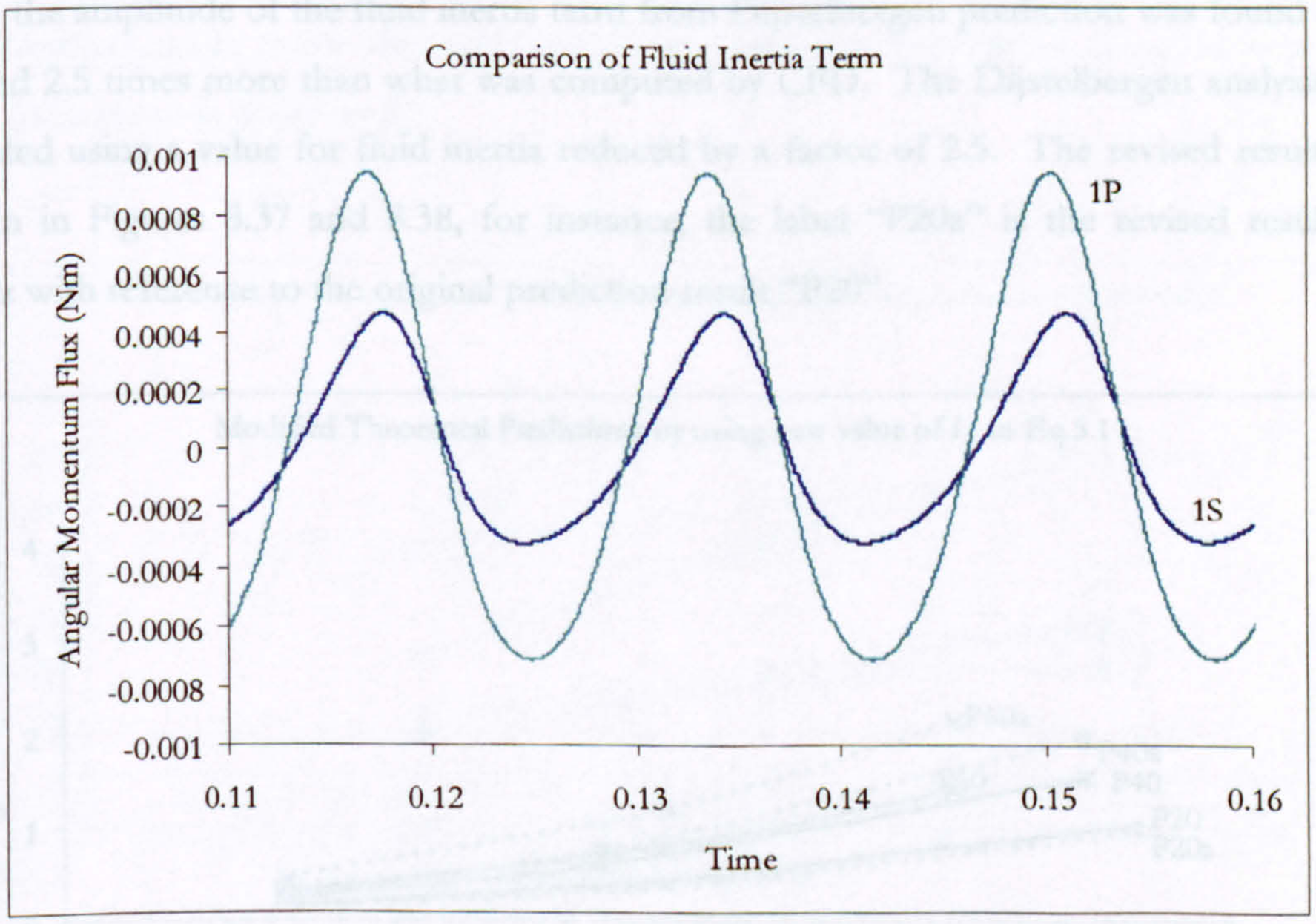

Figure 8. 35 **P9 (f_p=60 Hz, α_p=36.69%) – Comparisons of the fluid inertia terms from CFD Simulation and the Prediction using Dijstelbergen equation.**

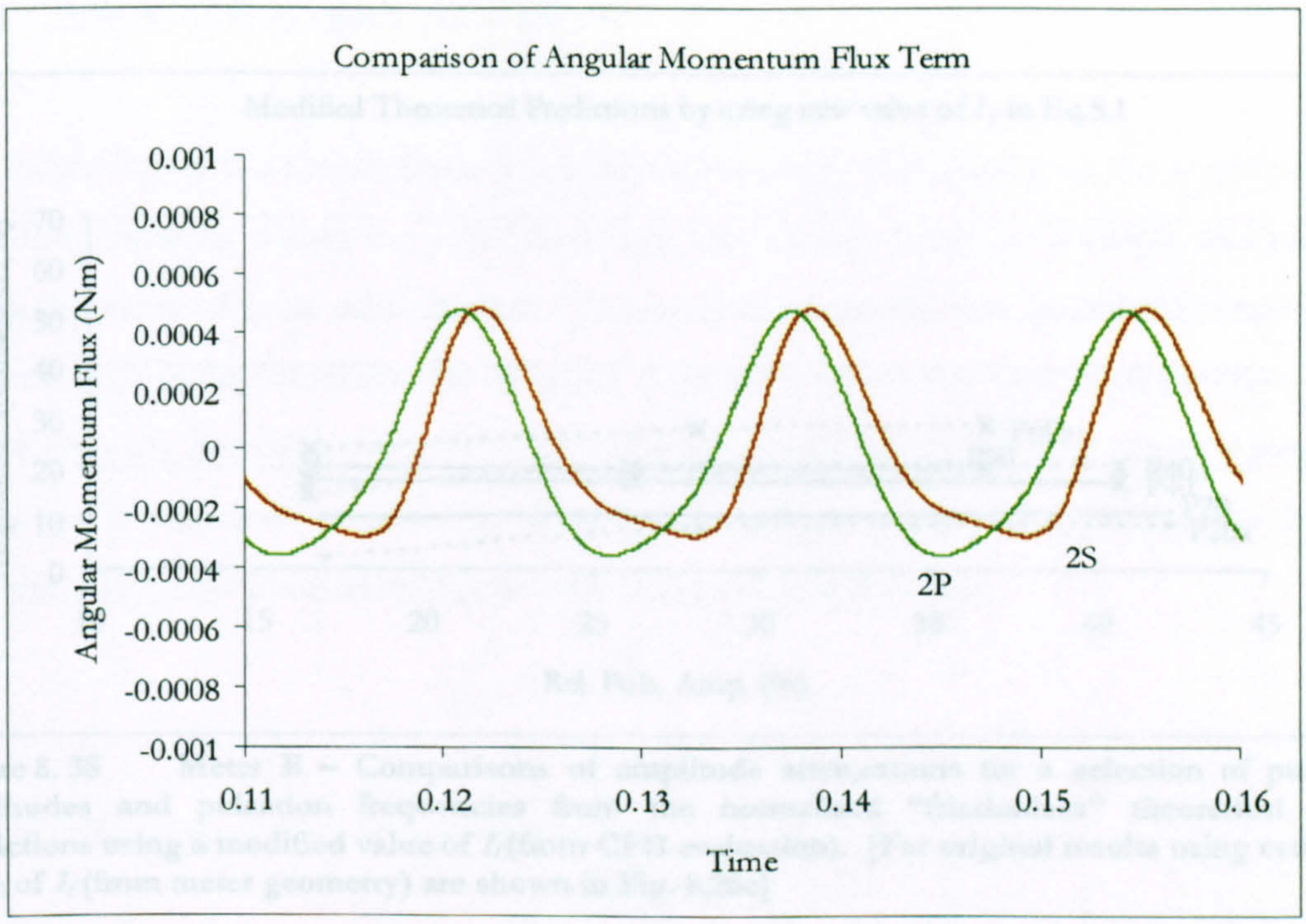

Figure 8. 36 **P9 (f_p=60 Hz, α_p=36.69%) – Comparisons of the momentum flux terms from CFD Simulation and the Prediction using Dijstelbergen equation.**

Since the amplitude of the fluid inertia term from Dijstelbergen prediction was found to be around 2.5 times more than what was computed by CFD. The Dijstelbergen analysis was repeated using a value for fluid inertia reduced by a factor of 2.5. The revised results are shown in Figures 8.37 and 8.38, for instance, the label "P20a" is the revised result for 20 Hz with reference to the original prediction result "P20".

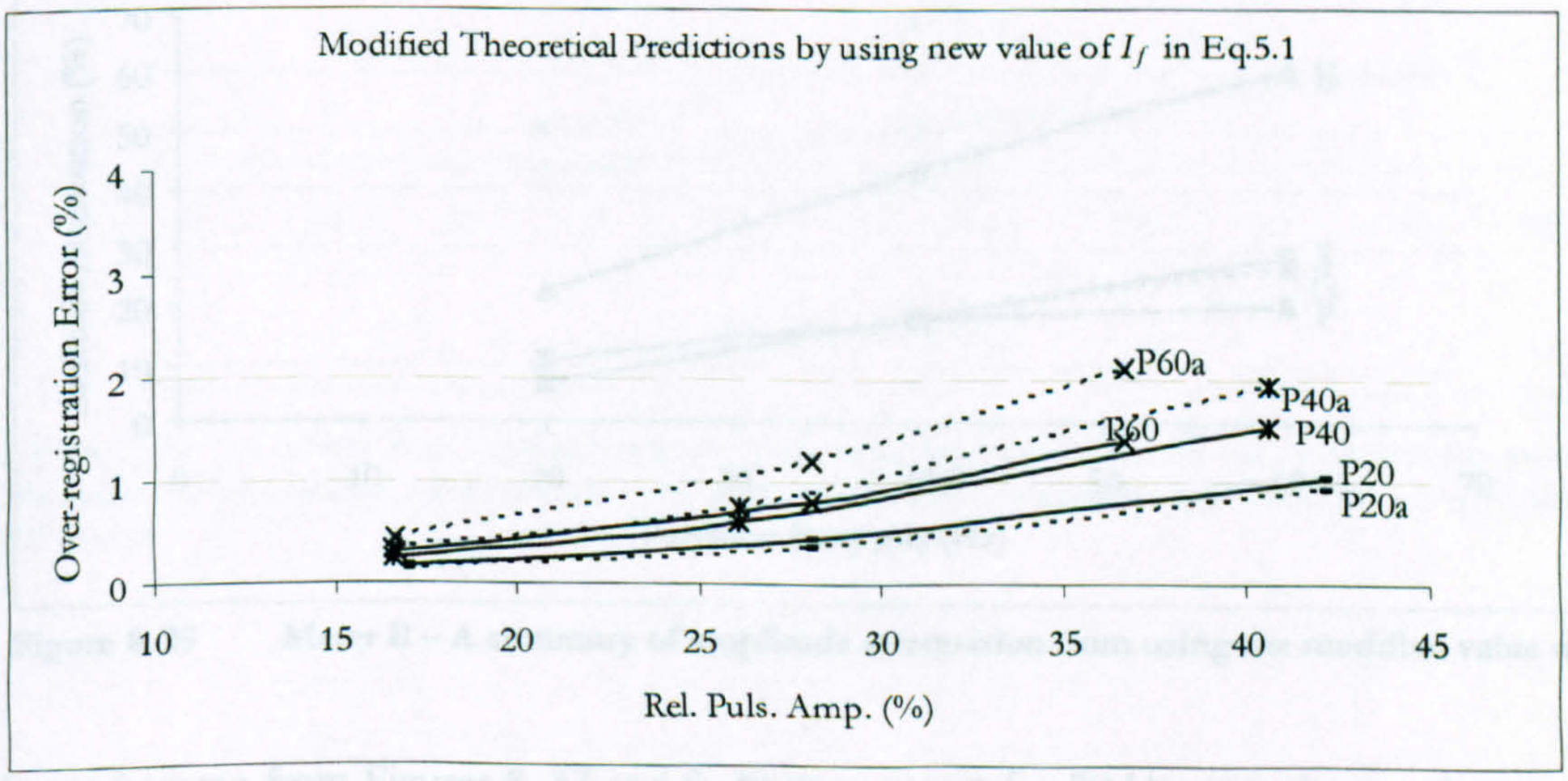

Figure 8. 37 **Meter B – Over-registration errors for a selection of pulsation amplitudes and pulsation frequencies from the normalised "frictionless" theoretical model predictions using a modified value of I_f (from CFD evaluation). [For original results using estimated value of I_f (from meter geometry) shown in Fig. 8.25c]**

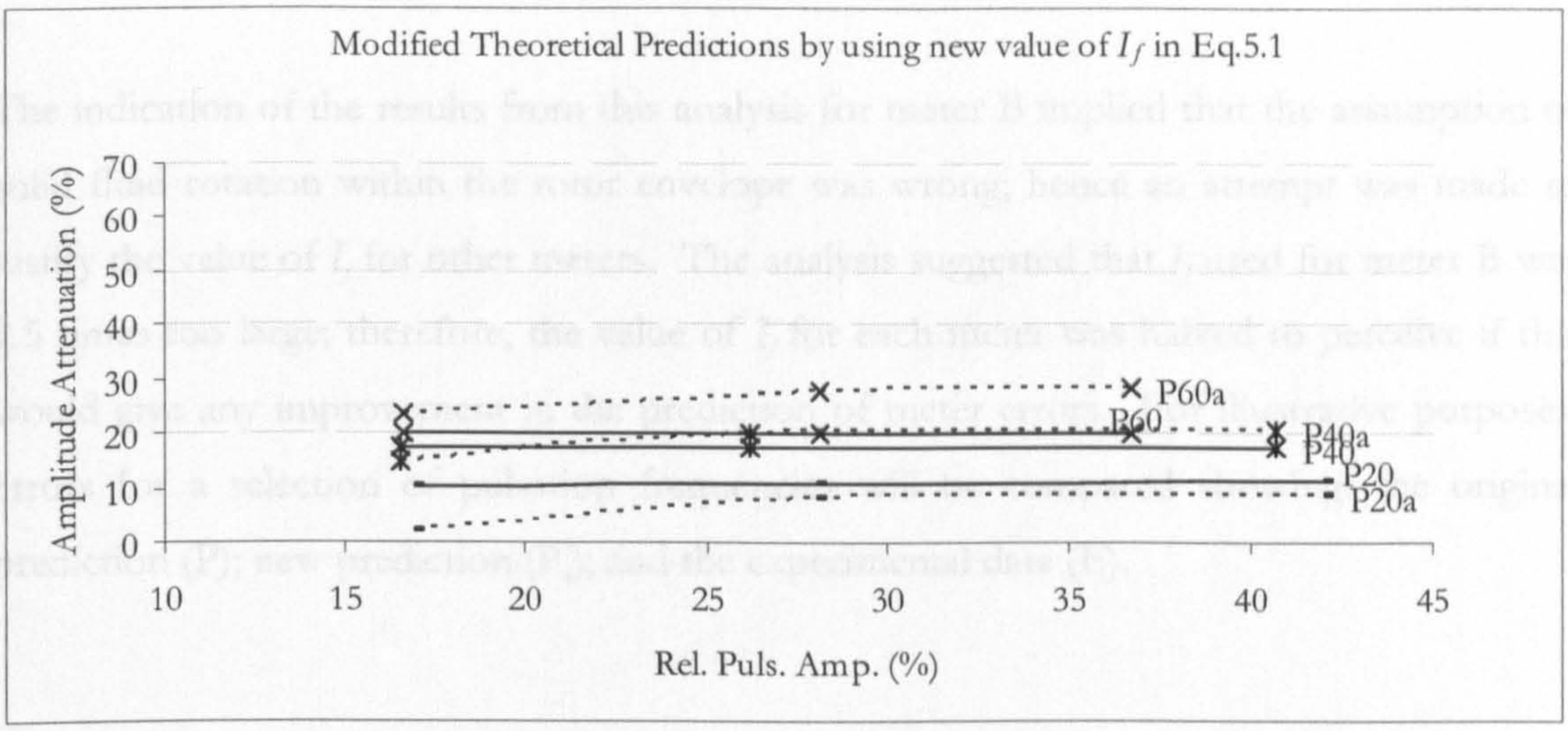

Figure 8. 38 Meter B – Comparisons of amplitude attenuations for a selection of pulsation amplitudes and pulsation frequencies from the normalised "frictionless" theoretical model predictions using a modified value of I_f(from CFD evaluation). [For original results using estimated value of I_f(from meter geometry) are shown in Fig. 8.26c]

Since the amplitude attenuation is mainly dependent on the imposed pulsation frequency, an alternative graph (as previously shown in Fig. 8.27) is now shown below, noting the improvement made to the theoretical predicted amplitude attenuation using the new value of I_f. (new curve is noted as P_a).

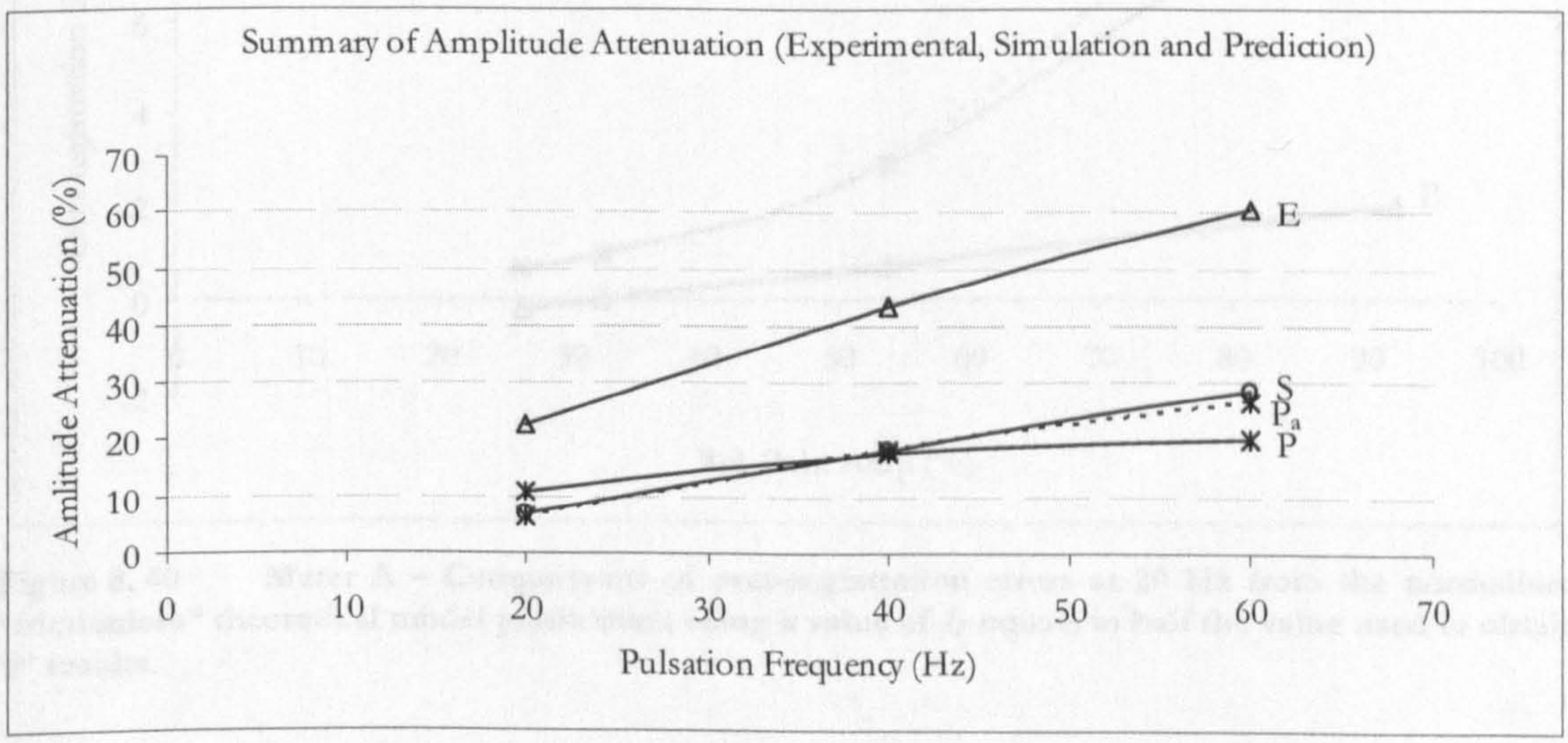

Figure 8. 39 Meter B – A summary of amplitude attenuation from using the modified value of I_f

It can be seen from Figures 8. 37 and 8. 39 that, except for 20 Hz case, the trends are now quite close to the CFD predicted result and are qualitatively improved relative to the experimental data (as compared to Figures 25a and 27).

8.5.2 Effects of fluid inertia on all meters

The indication of the results from this analysis for meter B implied that the assumption of solid fluid rotation within the rotor envelope was wrong; hence an attempt was made to justify the value of I_f for other meters. The analysis suggested that I_f used for meter B was 2.5 times too large; therefore, the value of I_f for each meter was halved to perceive if this would give any improvement in the prediction of meter errors. For illustrative purposes, errors for a selection of pulsation frequencies will be compared showing: the original prediction (P); new prediction (P_a); and the experimental data (E).

8.5.2.1 Predictions of over-registration error

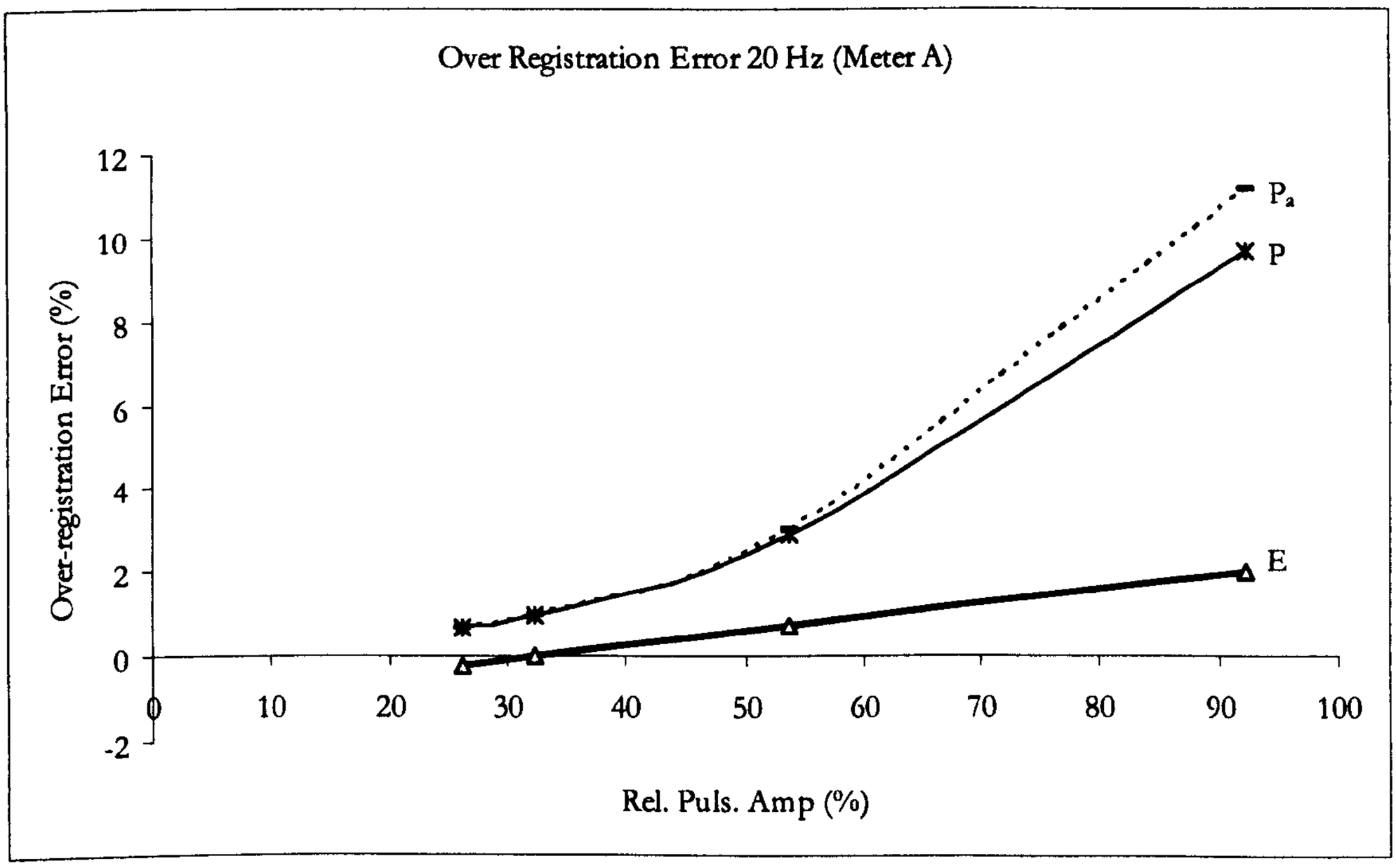

Figure 8. 40 Meter A – Comparisons of over-registration errors at 20 Hz from the normalised "frictionless" theoretical model predictions using a value of I_f equals to half the value used to obtain 'P' results.

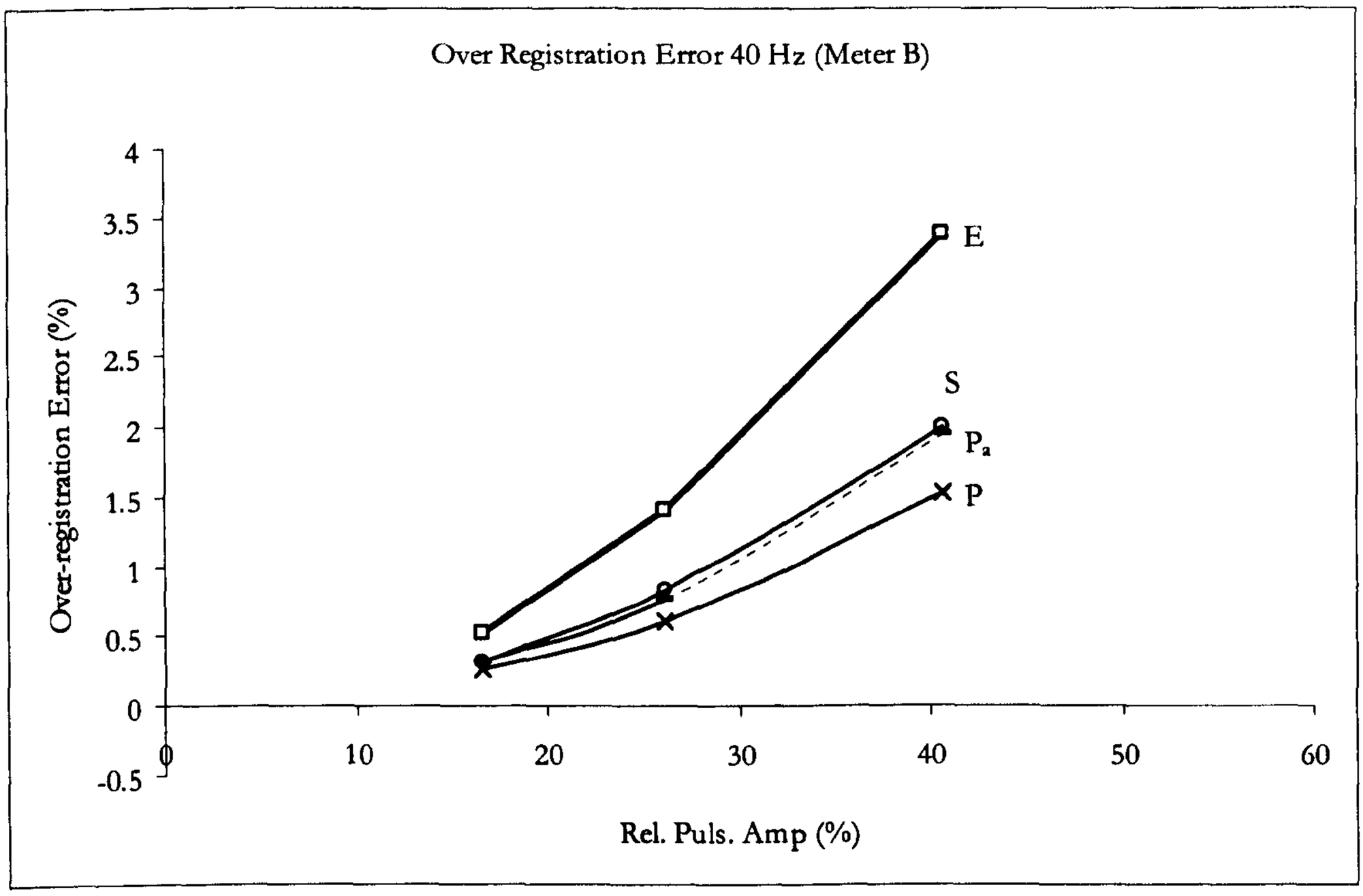

Figure 8. 41 Meter B – Comparisons of over-registration errors at 40 Hz from the normalised "frictionless" theoretical model predictions using a value of I_f equals to half the value used to obtain 'P' results. (Notation 'S' represents simulation data from CFD)

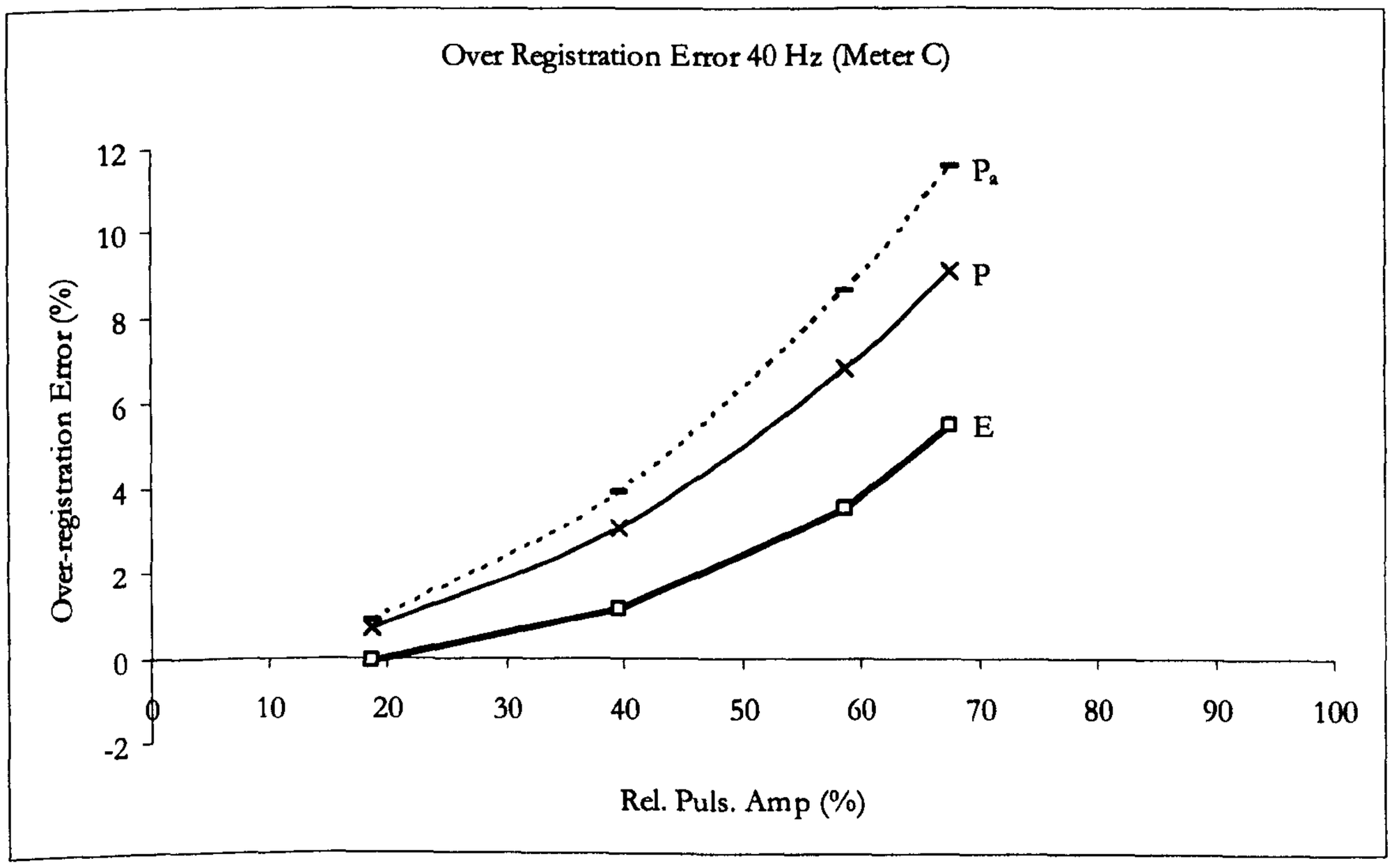

Figure 8. 42 Meter C – Comparisons of over-registration errors at 40 Hz from the normalised "frictionless" theoretical model predictions using a value of I_f equals to half the value used to obtain 'P' results.

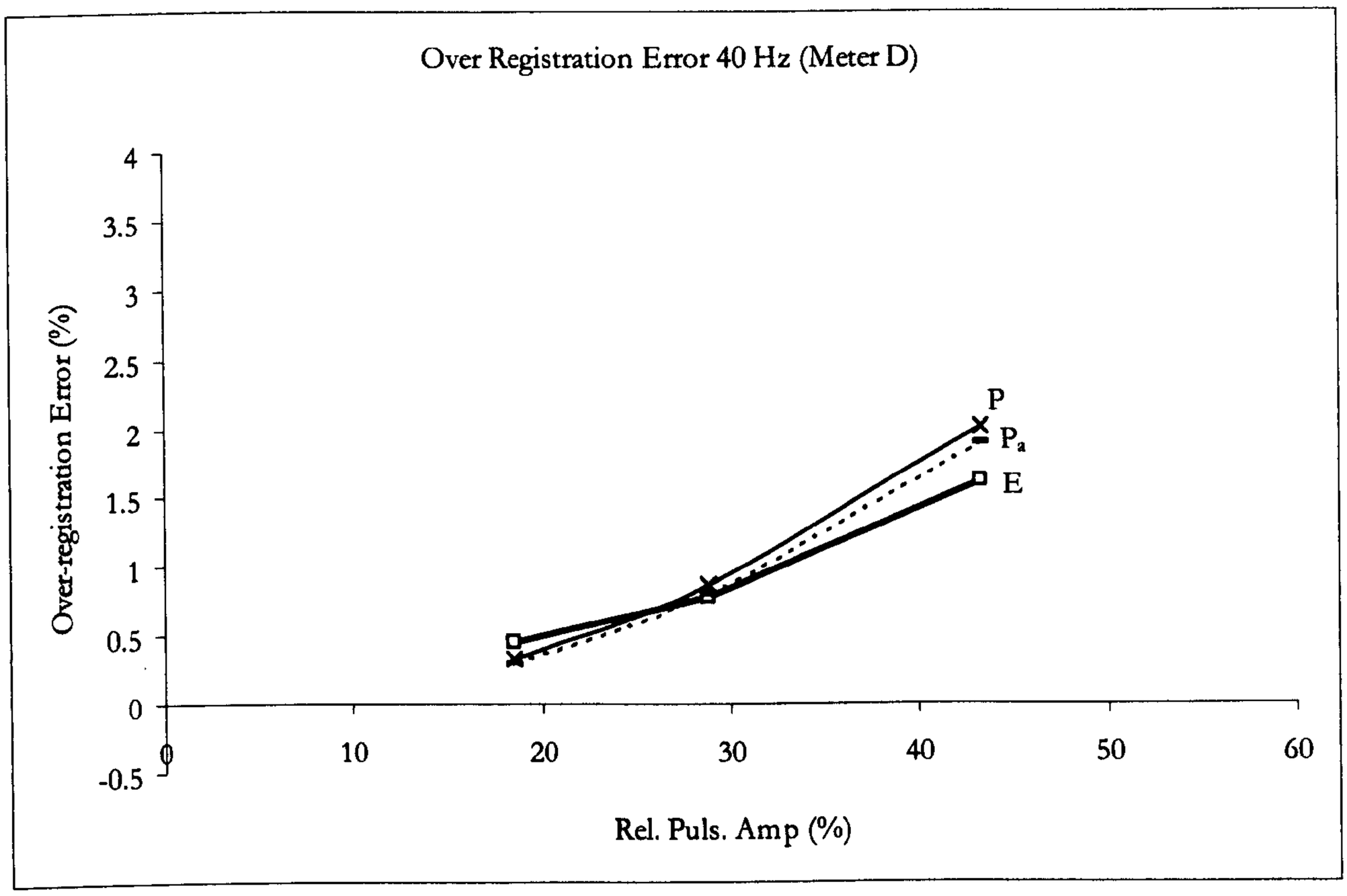

Figure 8. 43 Meter D – Comparisons of over-registration errors at 40 Hz from the normalised "frictionless" theoretical model predictions using a value of I_f equals to half the value used to obtain 'P' results.

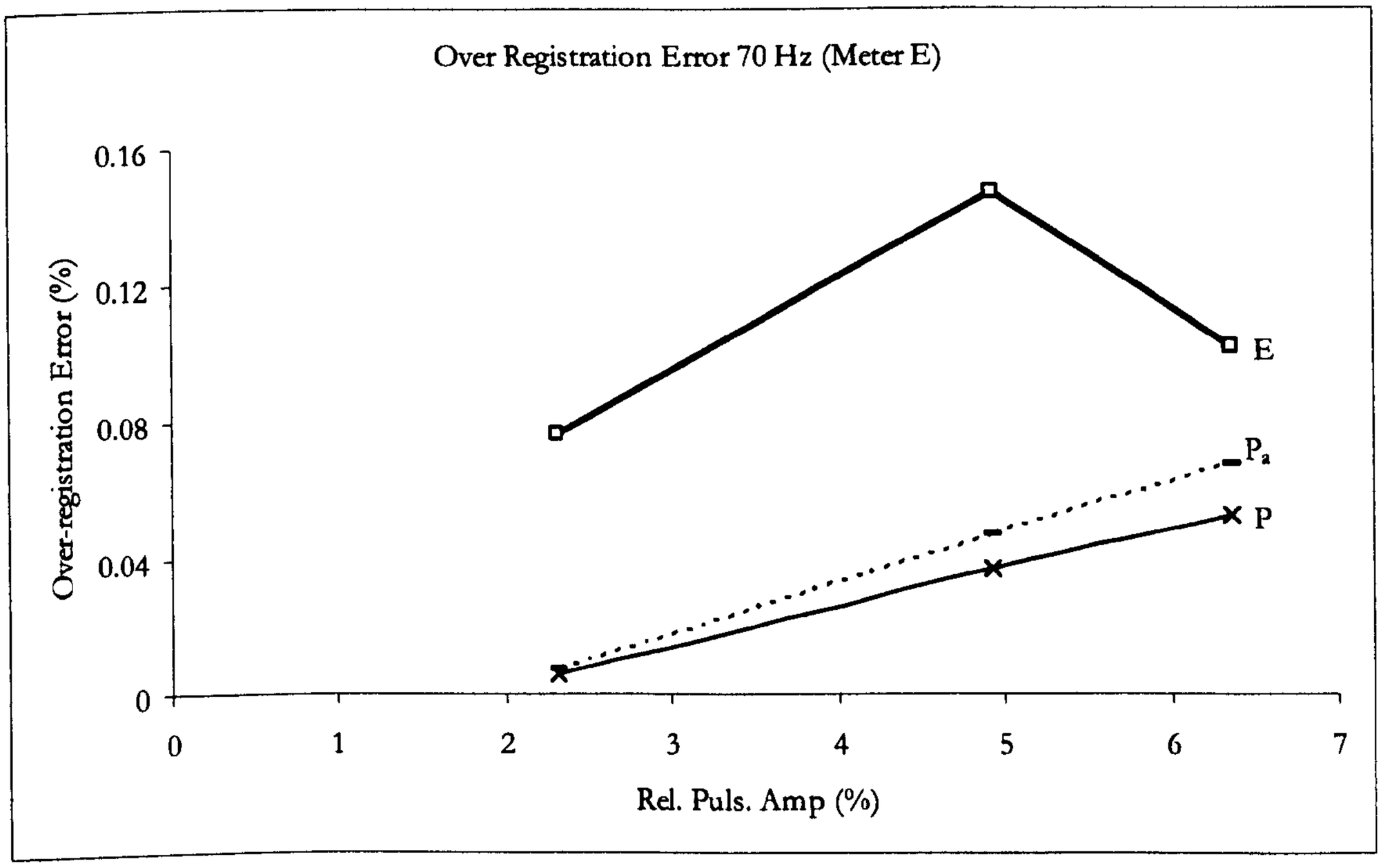

Figure 8. 44 Meter E – Comparisons of over-registration errors at 70 Hz from the normalised "frictionless" theoretical model predictions using a value of I_f equals to half the value used to obtain 'P' results.

8.5.2.2 Predictions of amplitude attenuation

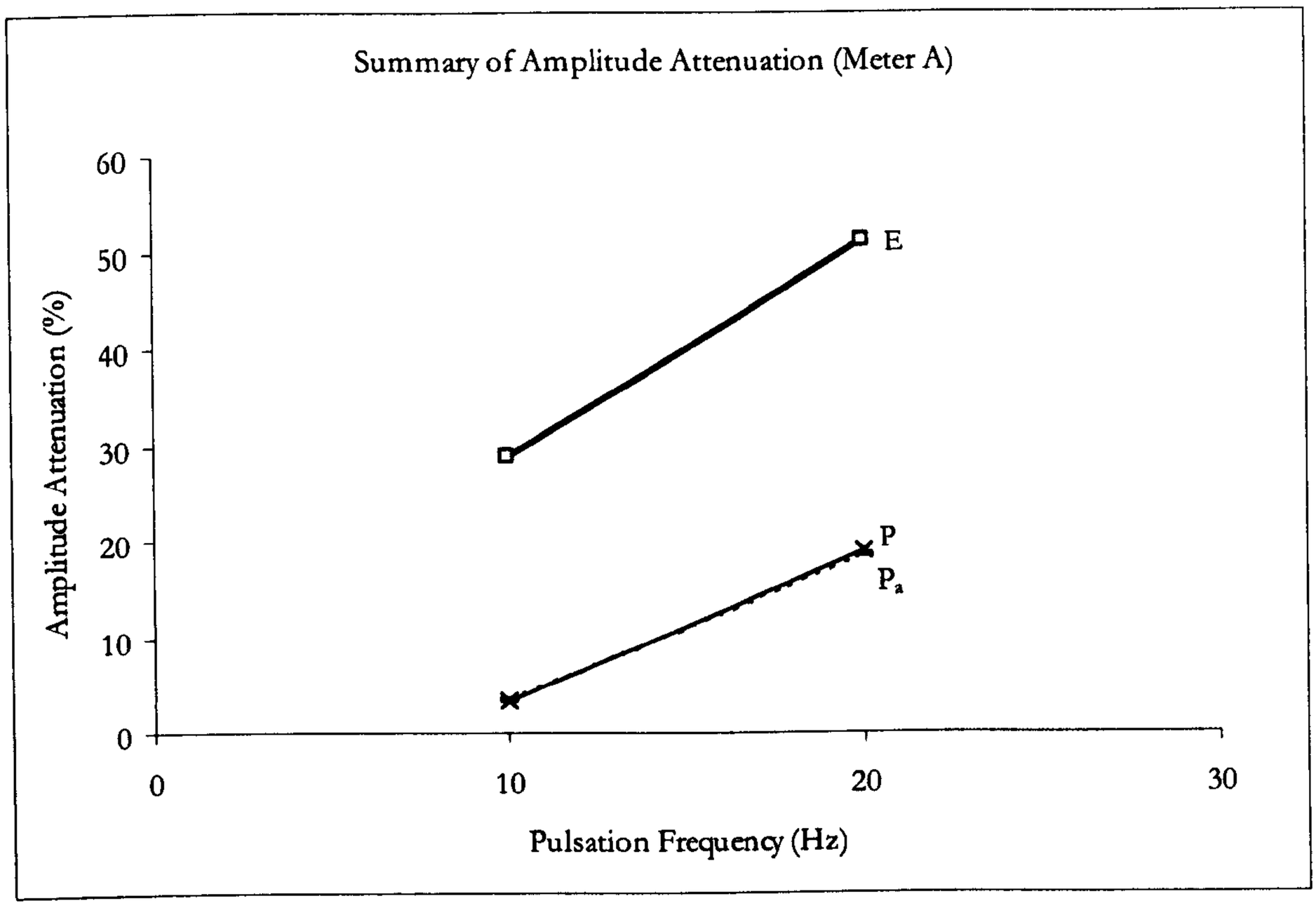

Figure 8. 45 Meter A – Comparisons of amplitude attenuation from the normalised "frictionless" theoretical model predictions using a value of I_f equals to half the value used to obtain 'P' results.

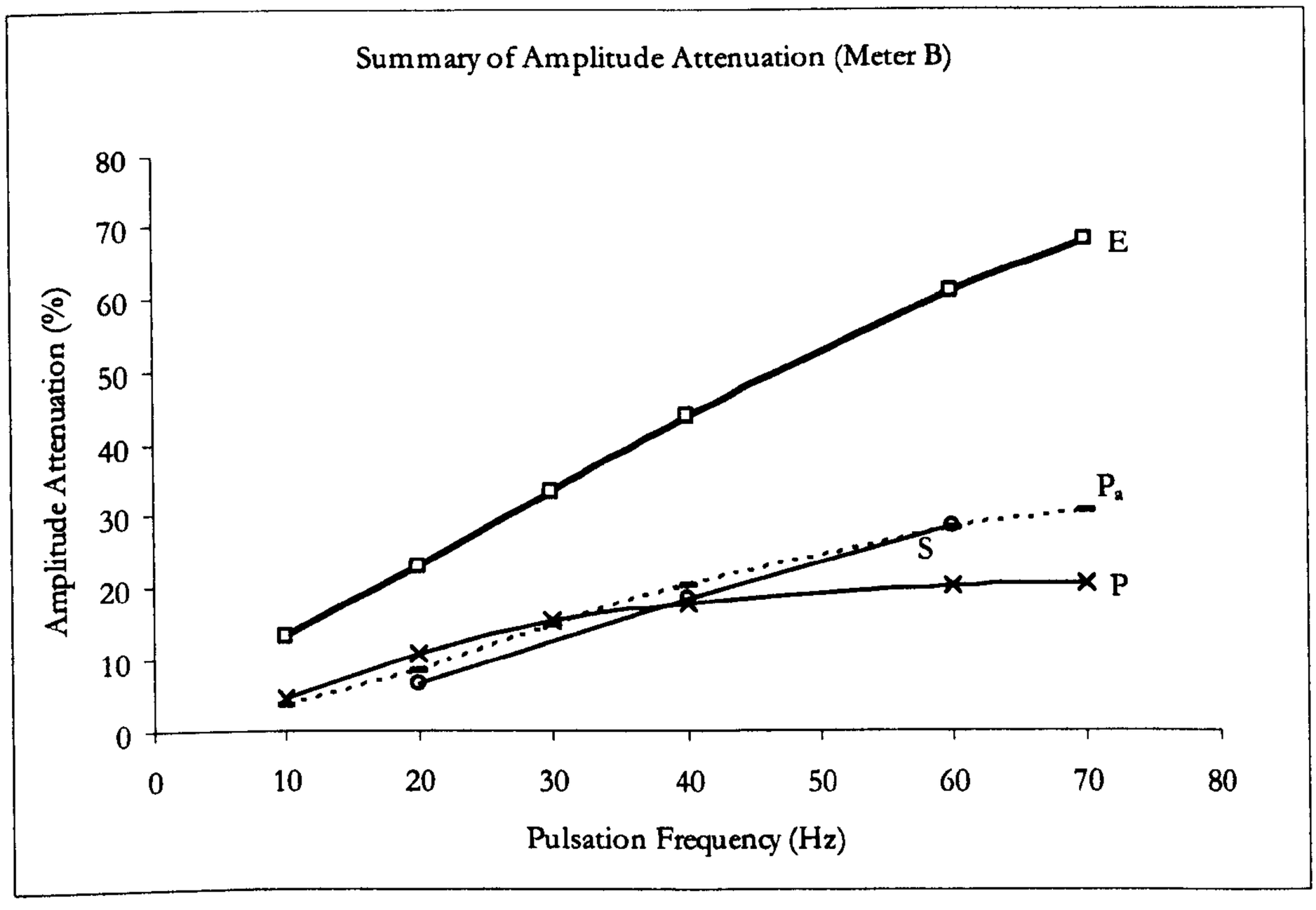

Figure 8. 46 Meter B – Comparisons of amplitude attenuation from the normalised "frictionless" theoretical model predictions using a value of I_f equals to half the value used to obtain 'P' results. (Notation 'S' represents simulation data from CFD)

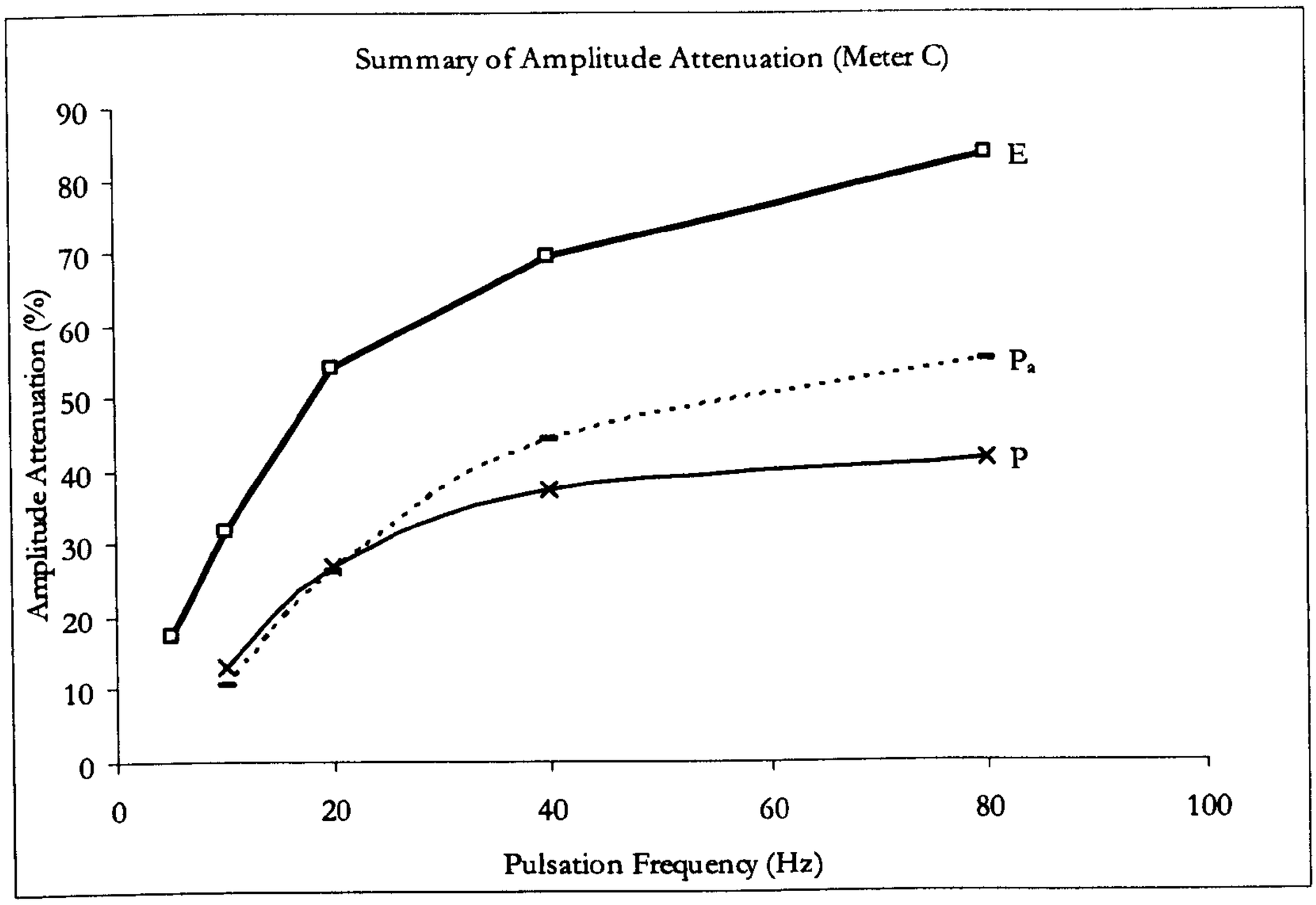

Figure 8. 47 Meter C – Comparisons of amplitude attenuation from the normalised "frictionless" theoretical model predictions using a value of I_f equals to half the value used to obtain 'P' results.

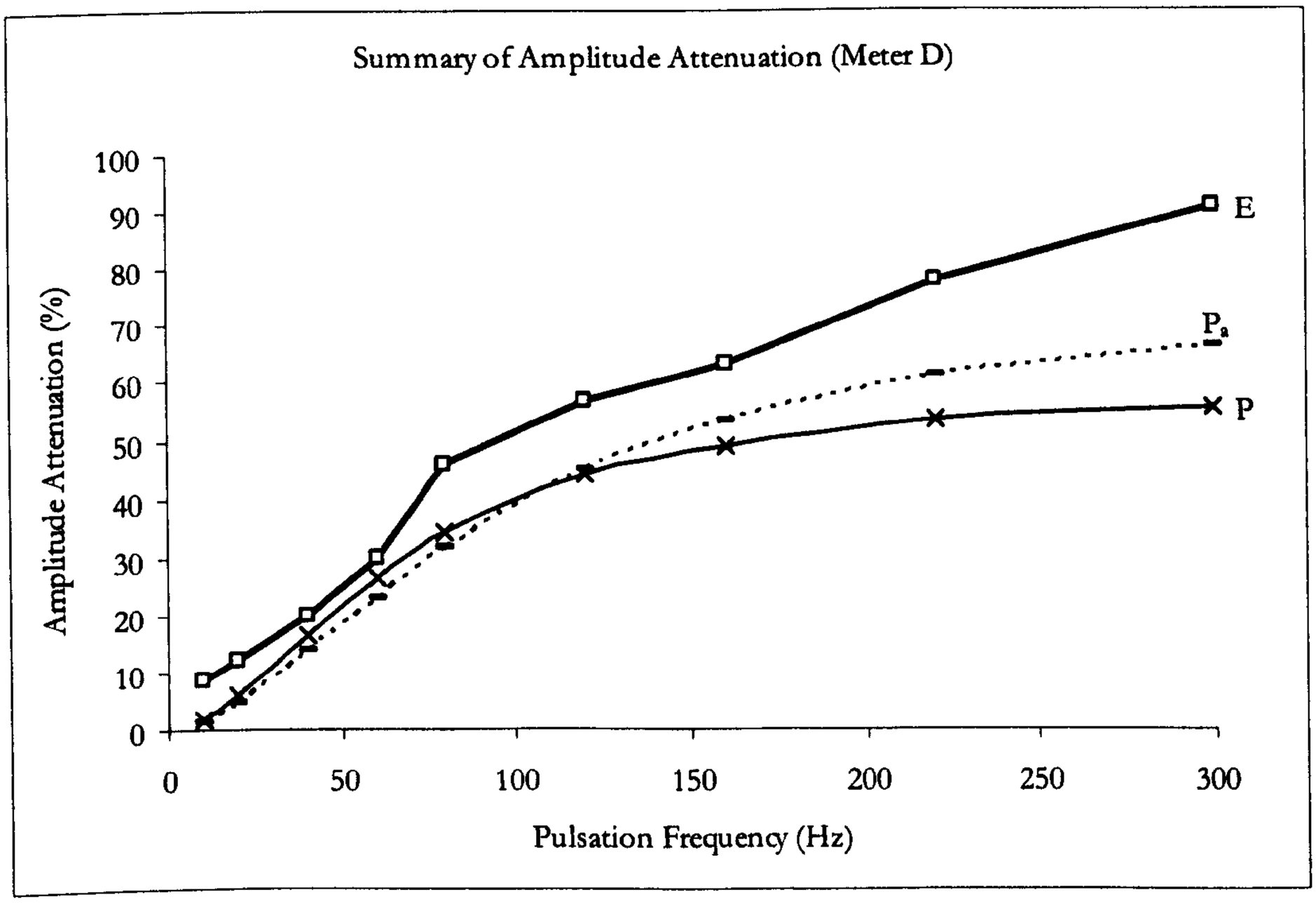

Figure 8. 48 Meter D – Comparisons of amplitude attenuation from the normalised "frictionless" theoretical model predictions using a value of I_f equals to half the value used to obtain 'P' results.

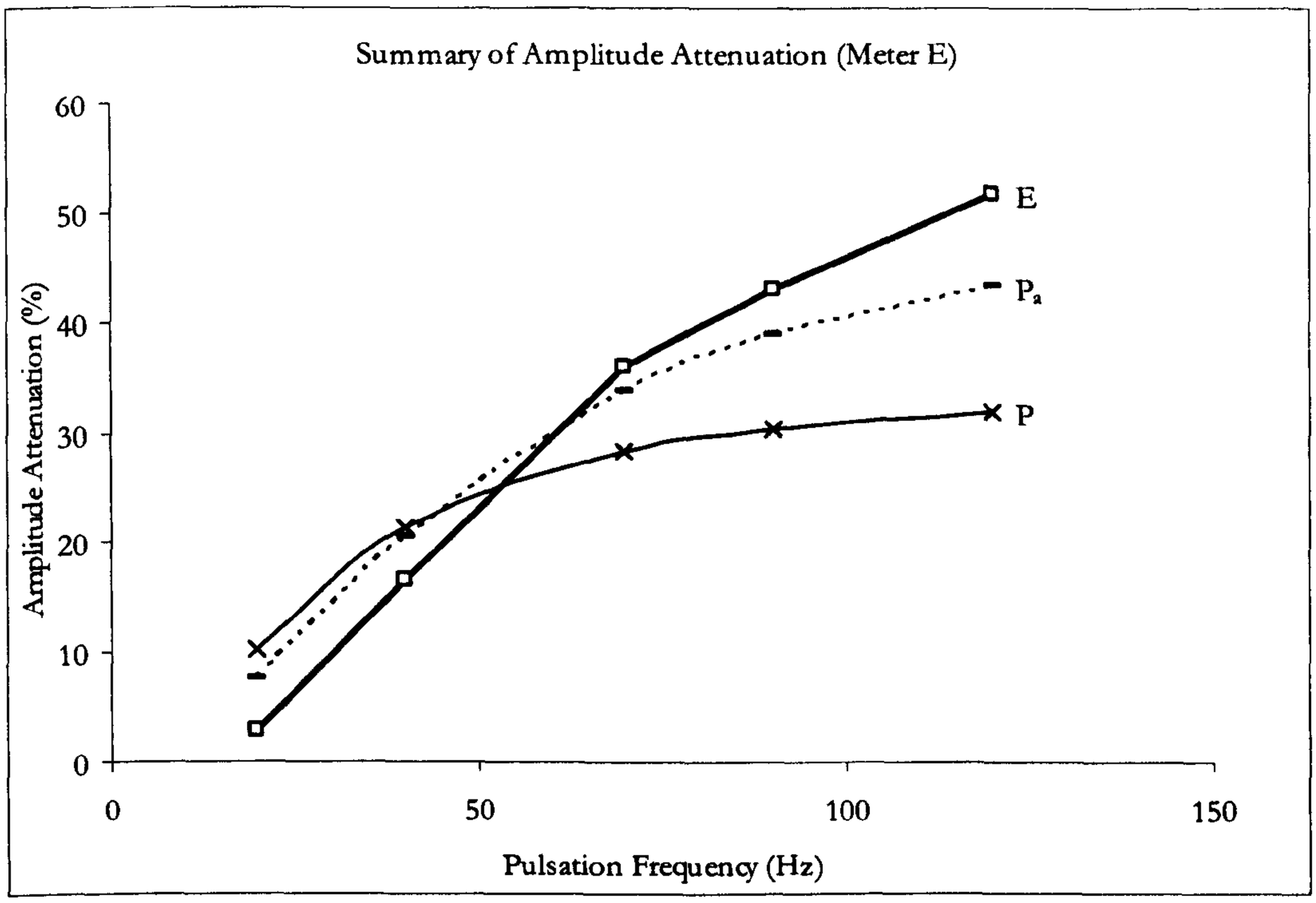

Figure 8. 49 Meter E – Comparisons of amplitude attenuation from the normalised "frictionless" theoretical model predictions using a value of I_f equals to half the value used to obtain 'P' results.

8.5.3 Discussion of revised predictions

Having used the new value of I_f, it can be seen from Figures 8.39 to 8.43, that whilst some predictions of over-registration errors have been improved (meters B, D & E), some predictions have been worse (meters A & C). However, in terms of correction of amplitude, it can be seen from Figures 8.44 to 8.48, that all of the amplitude errors have been improved.

From these observations, it could be deduced that all meters are very sensitive to the value of I_f.

8.6 Summary of CFD Results

Although the CFD data did not give a quantitative close agreement with the experimental data, CFD has facilitated an understanding of the rotor dynamics resulted from the various patterns of flow incidence, boundary layer growth and blade forces at the prevailing axial flow rates within the pulsation cycle. It is now known that the asymmetrical pattern of the blade acceleration within the flow cycle (Fig. 8.33) gives rise to the lagging of meter response and hence over-registration and amplitude attenuation.

The cause of the quantitative difference between CFD results and experimental data is due to a combination of a number of factors:

1. The CFD simulation was based on a very basic modelled geometry in which the various resistant torques, the real inlet flow profile and the wakes from the flow straightener were not accounted.

2. The solution procedure was only first order time accurate.

3. The relatively coarse grid and the length of time step were chosen to optimise for the quickest possible computational time for the solutions.

No attempt was made to determine the individual contribution of each of these factors.

It was also shown that the CFD data could emulate the meter error trends better than the prediction data resulted from using the Dijstelbergen equation. Having evaluated the conservation of angular momentum flux within the rotor envelope from the CFD data for case P9, it was found that the fluid inertia term used in the prediction for meter B was about 2.5 times larger than the value inferred from the CFD results. The CFD suggested value for the fluid inertia was incorporated into the prediction procedure and the trends from the prediction were improved for meter B.

However, the conclusion that the original value of I_f used for meter B was too large could not be directly applied to all meters; it is clear that the degree of sensitivity to the value of I_f used in the prediction procedures is very specific to the individual meter. No attempt was made to find specific I_f values for other individual meters.

Chapter 9 Conclusions and Future Work

In this chapter, the work presented in this thesis is concluded. The major achievements of the work are discussed in Chapter 9.1. A number of improvements to the correction method of the turbine meter signal are suggested in Chapter 9.2.

9.1 Conclusions

- New experimental evidence showed that there were over-registration errors and amplitude attenuations for a range of flowmeters, of sizes 6mm to 25mm. The typical trends are: (1) the higher the imposed pulsation frequency and pulsation amplitude, the higher the over-registration error; (2) the increase of amplitude attenuation mainly depends upon the increase of imposed pulsation frequency (See Chapters 5.2.4 and 6.5.2.3). Also experiments showed that the trends remained unchanged with varying operating flow rates within the linear range of the meter. Although the over-registration errors were within the limits of specified meter accuracy for low frequency pulsations (5 to 10 Hz), they may be significant for higher frequencies and larger pulsation amplitudes, maximum over-registration observed was 5.5 %. The amplitude attenuation error was likely to be significant over a considerable range of amplitudes and frequencies, and can be as large as 90%.

- Although various sizes of meters were studied experimentally, there was no unique correlation across the five meters in this study, therefore it was rather difficult to normalise the results in terms of either the meter size, or the number of blades, or the operating mean flow conditions. (Note that meters A and B both have the same number of blades, but they are of different sizes and different mean flow conditions; similarly meters A and C both can be tested under the same mean flow condition, but they have different number of blades and different size).

- Moreover, another problem that gave rise to the difficulties in normalising the experimental data with various meter sizes was the restriction of the flow rig's

capability in producing relatively large pulsations at higher flow rate. For meter E, at 1.740×10^{-3} m^3/s, the current maximum pulsation amplitude that the flow rig could achieve was less than 10%. For these experimental conditions, though meter E showed that there were significant amplitude attenuations, there were insignificant over-registrations observed. It is uncertain whether meter E would still remain accurate in mean flow indication if the pulsation amplitude is increased beyond 10%.

- On the basis of same operating flow condition, it was found that a meter with smaller value of the response parameter and ratio of inertias, $b(1+\lambda)$, gave better indication of the true flow than one with a larger value. This reflects what is expected from theory, as can be seen from Eq. 4. 18a, $\left[t_c = b(1+\lambda)/(\dot{V}_a - \Delta\dot{V}_a)\right]$, the time constant, t_c, is proportional to $b(1+\lambda)$, for any meter operating under the same flow condition.

- By using Dijstelbergen's frictionless theoretical method, error predictions of meter indicated mean flow and amplitude were made. Generally, under the same pulsating flow conditions, error predictions made for a meter with higher blade number (better flow guidance) were closer to the experimental values than those with lower blade number of the same size.

- Based on Dijstelbergen's frictionless theoretical model, a correction method was developed by Cheesewright to correct experimentally recorded meter signals. The most successful correction of mean flow error was the reduction from 1.99% to 0.08% and the maximum correction of amplitude attenuation was from 56.80% to 21.50%.

- Generally, for the correction of over-registration errors, the correction method was considered to be relatively more effective at higher pulsation amplitudes. The corrections of pulsation amplitude were generally more effective as pulsation frequency increases. It was deduced that as there were larger or quicker fluctuations in the flow, fluid inertia was more likely to be dominant over the various friction effects which were being ignored in the correction procedure.

- The correction method was also considered to be relatively more effective for meters with higher blade number, since more data points could be extracted from the meter, hence better point to point correction of the signal resulted. Therefore, for pulsating flow measurement, providing that the correction tool is applied, the use of a meter with a higher number of blades would yield better results than for a lower blade number.

- Although the CFD results did not give a close quantitative agreement with the experimental data, CFD has facilitated an understanding of the rotor dynamics resulting from the various patterns of flow separation and boundary layer growth within the pulsation cycle. It is now known that the asymmetrical pattern of the blade acceleration gives rise to the lagging meter response and, hence, over-registration and amplitude attenuation.

- For the one meter simulated, it was also shown that the CFD results could emulate the meter error trends better than the data resulting from using Dijstelbergen's equation. Having evaluated the rate of change of angular momentum within the rotor envelope from the CFD data for a particular case, it was found that the fluid inertia term used in the Dijstelbergen prediction was about 2.5 times larger than the value inferred from the CFD analysis. Thus, a corresponding reduced value for the fluid inertia was implemented into the prediction procedure and the trends from the prediction were correspondingly improved by 50% for this meter.

- However, the attempt to improve other meter error predictions by halving the respective individual fluid inertia values in the prediction procedure did not result in significant improvements. This could be due to the fluid inertia parameter used in the prediction procedures is very specific to the individual meter, in which factors such as number of blades, blade profile and blade tip clearance could influence the value of the effective fluid inertia.

9.2 Future Work

In this section, future work on both experimental investigation, CFD modelling, and subsequently the associated correction of meter readings are discussed.

- One of the restrictions experienced during the experimental investigation was the limitation of the maximum imposed pulsation frequency for each meter. The extraction of pulsating flow induced errors depended upon the quality of the signal waveform. This in turn, depended upon the number of data points that could be generated. Hence if it was possible, as proposed, to sample the rotor speed more frequently, this could extend the range of imposed pulsation frequency that could be. Thus, more extensive experimental investigation could then be achieved.

  The use of multiple pick-ups; such as having two pick-ups located around the meter at 90° out of phase to each other, together with the appropriate data processing technique, results in double the amount of data points from the meter. Alternatively, a drum could be fixed at the tip of the rotor with multiple, equally spaced, ferromagnetic studs to allow an increase of number of data points in the meter signal. Hence further tests of meter dynamic response could be possible. However, the above two suggested methods would possibly increase the resistant torque value due to increasing magnetic pick-up effect.

- If some non-dimensional parameters could be used to correlate experimental data, such as the Reynolds number and the Strouhal number, this would provide a more thorough insight into the turbine meter dynamic performance. Therefore further experimental work on different sizes of meter and different number of blades with limits of relevance would clarify this aspect.

- The correction tool could be developed further to allow real time application.

- If the CFD model could be developed and extended to allow parametric modelling, it would then be more readily available to predict the appropriate value of the fluid inertia term (for correction purposes) for individual meters. This, in turn, would facilitate a better prediction of errors for all meters.

- The CFD simulation could also be improved further to facilitate a more accurate solution. Some careful evaluation is needed to determine which solution algorithms are most influential to accuracy: (1) development of a finer grid to resolve the boundary layers throughout the domain; (2) more accurate second order time stepping procedure; (3) other discretisation schemes, such as higher-order upwind scheme with flux limiters, to ensure boundedness of the solution; and (4) the inclusion of friction effects.

References

Abbott and Basco. Computational Fluid Dynamics – An Introduction for Engineers, John Wiley & Sons, Inc. (1994) Chapter 9 – Computational fluid dynamics of turbulence.

Alspach, W. J., Miller, C. E. and Flynn, T. M. Mass flowmeters in cryogenic service. Flow Measurement Symposium, ASME. (1966) pp 34-56.

American Petroleum Institute: Measurement of liquid hydrocarbons by turbine meter systems. API standard 2534. (1970) March.

Anderson, J. D. Jr. The Handbook of Fluid Dynamics (edited by Johnson, R.). CRC Press Ltd. (1998) Chapter 2 — Some Reflections on the History of Fluid Dynamics.

Arnberg, B.T. In the "Discussion" of Shafer, M. R. — Performance characteristics of turbine flowmeters. J. Basic Engineering. (1962) 84, pp 471-485.

Atkinson, K. N. A software tool to calculate the over-registration error of a turbine meter in pulsation flow. Flow Meas. Instrum. (1992) 3(3), pp 167 – 172.

Baker, R. C. and Deacon, J. The behavior of turbine, vortex and electromagnetic flowmeters. The Chemical Engineer. (1984) 401, pp 13 – 15.

Baker, R. C. An introductory guide to flow measurement. MEP Ltd, London. (1989) Chapter 5.2 — Turbine meters, Chapter 5.3 — Oscillatory meters.

Baker, R. C. Turbine flowmeters: II. Theoretical and experimental published information. Flow Meas. Instrum. (1993) 4(3), pp 123-144.

Baker, R. C. Coriolis flowmeters: industrial practice and published information. Flow Meas. Instrum. (1994) 5, pp 229-246.

Baker, R. C. Flow Measurement Handbook. Cambridge University Press 2000. (2000) Chapter 10 — Turbine and Related Flowmeters, Chapter 12 — Electromagnetic Flowmeters.

BBC News Online. "Price of Brent crude for February 2001 delivery closed at $24.35 a barrel on 2nd Jan 2001...." (2001) January. (http://news.bbc.co.uk/hi/english/business/newsid_1096000/1096916.htm)

Bean, H. S. The expanding field of fluid metering. Flow Measurement Symposium ASME. (1966) pp 1 – 4.

Berto, F. J. Technology review of tank measurement errors, reveals techniques for greater accuracy. Oil and Gas Journal Online (http://ogj.pennnet.com/). (1997) 95(9).

Birkhead, W. G. Field Experience with Turbine Meters. Proceedings of the International School of Hydrocarbon Measurement. (1985) pp 406-408.

Blows, L. G. Towards a better turbine flowmeter. International Conference on Advances in Flow Measurement Techniques. (1980) September, pp 307-315.

British Standard, BS 6169: Part 2: 1984 (ISO 2715-1981). British Standard Methods for Volumetric measurement of liquid hydrocarbons. Part 2. Turbine meter systems. British Standards Institution. [ISO title: Liquid hydrocarbons – Volumetric measurement by turbine meter systems] (1984).

British Standard, BS ISO TR 3313:1998. Measurement of fluid flow in closed conduits — Guidelines on the effects of flow pulsations on flow-measurement instruments. British Standards Institution. (1998).

Bronner, J. W. and McKee, R. J. Cogen Pulsation Effects on Turbine Metering. Proceedings of American Gas Association. Operating Section. (1991) April, pp 625-638.

Caffrey, C., McEwen D. and Neal, A. Installation and viscosity effects on turbine flowmeters — A CFD modelling approach supported by practical testing. National Measurement System Policy Unit, D.T.I., London. (1997) March

Cheesewright, R., Edwards, D. and Clark, C. Measurements with a turbine flow meter in the presence of large, non-sinusoidal pulsations. Fluid Control, Measurement and Visualization (FLUCOME) 1994 Symposium, Toulouse. (1994).

Cheesewright, R and Clark, C. The influence of forces due to electromagnetic pick-ups on the performance of small turbine flowmeters. Proc Instn. Mech. Engrs. (1996) 210, pp 243-247.

Cheesewright, R., Atkinson, K. N., Clark, C., Horst, G. J. P. , Mottram, R. C. and Viljeer, J. Field tests of turbine meter correction procedures. Flow Meas. Instrum. (1996) 7(1), pp 7-17.

Cheesewright, R. and Clark, C. Step-response tests on turbine flow meters in liquid flows. Proc Instn. Mech. Engrs. (1997) 211(A), pp 321-329.

Cheesewright, R., Bisset, D. and Clark, C. Factors which influence the variability of turbine flowmeter signal characteristics. Flow Meas. Instrum. (1998) 9, pp 83-89.

Cheesewright, R. and Clark, C. The dynamic response of coriolis massflow meters. Fluid Control, Measurement and Visualization (FLUCOME) 2000 Symposium, Canada. (2000) August.

Clark, C. The measurement of dynamic differential pressure with reference to the determination of pulsating flows using DP devices. Flow Meas. Instrum. (1992) 3, pp 145-150.

Daniel International Ltd. "Turbine Meter Theory" (2001) January. (http://www.daniel.co.uk/tm2.htm)

DeFeo, J. W. Turbine Flowmeters for Measuring Cryogenic Liquids. Advances in Instrumentation, Proceedings. (1992) 47(1), pp 465-472.

Deschere, A. R. Basic difficulties in pulsating-flow metering. Trans. ASME. (1952) 74, pp 919- 923.

Dijstelbergen, H. H. Dynamic response of turbine flowmeters. Instrum. Rev. (1966) 13, pp 241-244.

Dowdell, R. B. and Liddle, A. H. Measurement of pulsating flow with propeller and turbine type flowmeters. Trans. A.S.M.E. (1953) 75, pp 961-968.

Ferreira, V. C. S. Flow patterns inside a turbine type flowmeter. PhD Thesis, Cranfield Institute of Technology. Cranfield, Bedford, April 1988.

Fox, R. W and McDonald, A. T. Introduction to Fluid Mechanics. John Wiley and Sons, Inc. 4th Edition (1994) Chapter 2 Fundamental Concepts, p20.

Gajan, P., Mottram, R. C., Hebrard, P, Andriamihafy, H. and Platet, B. The influence of pulsating flows on orifice plate flowmeters. Flow Meas. Instrum. (1992) 3, pp 118-121.

Gannon, J. Getting the most from turbine flowmeters. Machine Design. (1994) 66, pp 55-58.

Gannon, J. Turbine flowmeters for liquids and gases. Sensors. (1994) 11(10), pp 38-42.

Ginesi, D. A raft of flowmeters on tap - Engineering Practice (Part 2). Chemical Engineering. (1991) 98(5), pp 146-155.

Grey, J. Transient response of the turbine flowmeter. Jet Propulsion. (1956) February, pp 98-100.

Gruskos, R. L. Cryogenic flow measurement utilizing the turbine flowmeter — an overview. Advances in Instrumentation. (1985) 40(2), pp 1017-1025.

Hakansson, E., and Delsing, J. Effects of pulsating flow on an ultrasonic gas flowmeter. Flow Meas. Instrum. (1994) 5(2), pp 93-101.

Hall, N. A. Orifice and flow coefficients in pulsating flow. Trans. ASME. (1952) 74, pp 925-929.

Higson, D. J. The transient performance of turbine flowmeters in water. J. Sci Instrum. (1964) 42(5), pp 337-342.

Hochreiter, H.M. Dimensionless correlation of coefficients of turbine type flowmeters. Trans. ASME. (1958) 80, pp 1363-1368.

Jepson, P. Method of measuring the time constants of current meters and turbine-type flowmeters. J. Sci. Instrum. (1967) 44, pp 17-20.

Jepson, P. Transient response of a helical flowmeter. J. Mech. Engng Sci. (1964) 6(4), pp 317-320.

Jepson, P. and Bean, P.G. Effect of upstream velocity profiles on turbine flowmeter registration. J. Mechanical Engineering Science. (1969) 11(5), pp 503-510.

Kalivoda, R. Fundamentals of liquid turbine meters, Technical paper 103B, Bulletin TP02001, Issue/Rev. 0.1 (8/98), Smith Meter Inc. (1998).

Launder, B. E. and Sharma, B. T. Application of the energy dissipation model of turbulence to the calculation of flow near a spinning disc. Lett. Heat and Mass Transfer. (1974) 1, pp 131-138.

Launder, B. E. and Spalding, D. B. The numerical computation of turbulent flow. Computational Methods Appl. Mech. Eng. (1976) 14, pp 269-289.

Lee, W. F. Z. and Karlby, H. A study of viscosity effect and its compensation on turbine-type flowmeters. J. Basic Engineering. (1960) 82, pp 717-728.

Lee, W. F. Z. and Evans, H. J. A field method of determining gas turbine meter performance. J. Basic Engineering. (1970) 92, pp 724-731.

Lee, W. F. Z., Kirik, M. J. and Bonner, J. A. Gas turbine flowmeter measurement of pulsating flow. J. Engineering for Power. (1975) 97, pp 531-539.

Liu, F.F. In the "Discussion" of Shafer, M. R. — Performance characteristics of turbine flowmeters. J. Basic Engineering. (1962) 84, pp 471-485.

Madison, R. Modern Electronics Meet Turbine Flowmeters. Measurements and Control. (1995) 170, pp 128-132.

Massey, B. S. Mechanics of fluids. ELBS/Van Nostrand Reinhold (International) Co. Ltd. (1988) p 329.

McCoy, M. Smart turbine flowmeters for aerospace applications. Sensors. (1994) 11(3), pp 11-13.

McKee, R. J. Pulsation effects on single- and two-rotor turbine meters. Flow Meas. Instrum. (1992) 3(3), pp 151-166.

McShane, J. L. Ultrasonic flowmeters. Flow - Its Measurement and Control In Science and Industry. (1974) 1, pp 897-913.

Minemura, K., Egashira, K., Ihara, K., Furuta, H., and Yamamoto, K. Simultaneous measuring method for both volumetric flow rates of air-water mixture using a turbine flowmeter. J. of Energy Resources Technology. (1996) 118, pp 29-35.

Mottram, R. C. An overview of pulsating flow measurement. Flow Meas. Instrum. (1992) 3, pp 114-117.

Mullen, T. E. Turbine meters benefit from field-tested O&M procedures. Pipeline Industry. (1994) 77(12), pp 42-47.

Nakayama, Y. and Boucher R. F. Introduction to fluid mechanics. London: Arnold. (1999) pp 67-70.

National Space Development Agency of Japan (NASDA). "Results of Cryogenic Propellant Loading Test of H-II Launch Vehicle No. 8." (1999) October. (http://www.tksc.nasda.go.jp/Home/Press/e/199910/h28_991006_e.html)

Nicholl, A.J. Factors affecting the performance of turbine meters. Brown Boveri Review. (1977) 11, pp 684-692.

Oppenheim, A. K. and Chilton, E. G. Pulsating flow measurement — a literature survey. Trans. ASME (1955) 77, pp 231-248

Osha Federal Register. "Electric power generation, transmission, and distribution; electrical protective equipment - 59:4320-4476" (1994) January. (http://www.osha-sic.gov/FedReg_osha_data/FED19940131.html)

Ovodov, G. I., Raskovalkina, E. A. and Seifer A. L. Dynamic characteristics of turbine-type flowmeters for cryogenic fluids. Meas. Techniques. (1989) 31(10), pp 975-980.

Ower, E. On the response of a vane anemometer to an air-stream of pulsating speed. Phil. Mag. Ser.7. (1937) 23(157), pp 992-1005.

Patankar, S. V. and Spalding, D. B. A calculation procedure for heat, mass and momentum transfer in three dimensional parabolic flows. Int. J. Heat Mass Transfer. (1972) 15(10), pp 1787-1806.

Peronneau, P. A., Pellet, M. M., Xhaard, M. C., Hinglais, J. R. The electromagnetic flowmeter as applied to the measurement of blood flow in living systems. Invited paper — Flow — Its Measurement and Control in Science and Industry. Pittsburgh. Instrument Society of America. (1971) 1(3), pp 1337-1345.

Ross, G. The electromagnetic flowmeter as applied to the measurement of blood flow in living systems. Invited paper — Flow — Its Measurement and Control in Science and Industry. Pittsburgh. Instrument Society of America. (1971) 1(3), pp 1337-1345.

Rouse, H. and Ince, S. History of Hydraulics. Dover Publications, Inc. (1963) Chapter 1 — Practical hydraulics in early antiquity.

Rowell, P. Turbine Flowmeters, Monitor of Choice for Custody Transfer. Control Engineering. (1996) 43, pp 85-86.

Salami, L. A. Effect of upstream velocity profile and integral flow straighteners on turbine flowmeters. J. Heat and Fluid Flow. (1984) 5, pp 155-164.

Salami, L. A. Analysis of swirl, viscosity and temperature effects on turbine flowmeters. Trans. Inst. Meas. Control. (1985) 7(4), pp 183-202.

Shafer, M. R. Performance characteristics of turbine flowmeters. J. Basic Engineering. (1962) 84, pp 471 – 485.

Shaw, C. T. Using computational fluid dynamics. London: Prentice Hall. (1992) pp 23-27.

Sparks, C. R. A study of pulsation effects on orifice metering of compressible flow. Flow Measurement Symposium, Trans. ASME. (1966) pp 124-138.

Speziale, C. F. and So, R. M. C. The Handbook of Fluid Dynamics (edited by Johnson,

R.). CRC Press Ltd. (1998) Chapter 14 – Turbulence Modeling and Simulation.

Stanley Middleman. An introduction to fluid dynamics — principles of analysis and design. John Wiley and Sons, Inc. (1998) Chapter 4 – Conservation of Mass and Momentum in a Continuous fluid. p144.

Tan P.A.K. and Hutton, S. P. Experimental, analytical and tip clearance loss studies in turbine-type flowmeters. Proc. Harwell Conference on Modern Development in Flow Measurement. (1971) September, pp 321-346.

The Animated Software Company. "Piston Pump" (2001) January.
(http://www.animatedsoftware.com/pumpglos/pistpump.htm)

The Foot Rule Unit Conversion. "One barrel of oil (42 US gallons) contains 0.158987m^3 of oil" (2001) January.
(http://www.omnis.demon.co.uk/conversn/convjvsc.htm)

The National Space Society. "Background Information — DoD & The X-33 SSTO Program" (1997).
(http://www.hvcn.org/info/a2s2/backgrnd.html.)

Theodorsen, T. General theory of aerodynamic instability and the mechanism of flutter. NACA TR 496, 1935.

Thompson, R. E. and Grey, J. Turbine flowmeter performance model. J. Basic Engineering. (1970) 92, pp 712-723.

Tiemstra, G., Rans, R. and Backus, H. Comparison of orifice and turbine meter accuracy. Proceedings of Amer. Gas Assoc., Operating Sect. (1991) April, pp 593-603.

Tsukamoto, H. and Hutton, S. P. Theoretical prediction of meter factor for a helical turbine flowmeter, Conf. FLUCOME '85. (1985) pp 973-978.

Universal Currency Converter. "Exchange rate as of 4th January 2001, 1USD = 0.67 GBP" (2001) January.
(http://www.xe.net/ucc/convert.cgi)

Vetter, G., Notzon, S. Effect of pulsating flow on Coriolis mass flowmeters. Flow Meas. Instrum. (1994) 5, pp 263-273.

Watson, G. A. and Furness, R. A. Development and application of the turbine meter. Proc. Transducer 77 Conf. Flow Measurement Session, Wembley, London. (1977) June, pp 1-16.

White, F. M. Fluid mechanics. Mc Graw-Hill. (1979) pp 10-13.

Wilson, M. P. Jr. Flow Measurement — Practical Guides for Measurement and Control. Instrument Society of America. (1991) Chapter 2 — Historical Perspective.

Xu, Y. Calculation of the flow around turbine flowmeter blades. Flow Meas. Instrum. (1992) 3(1), pp 25-35.

Xu, Y. A model for the prediction of turbine flowmeter performance. Flow Meas. Instrum. (1992) 3(1), pp 37-43.

Zarek, J. M. The neglected parameters in pulsating flow measurement. Flow Measurement Symposium, ASME. (1966) pp 14-33.